KOMUNIKÁCIE
COMMUNICATIONS

5
Peter Bury – Igor Jamnický – Peter Hockicko
ACOUSTOELECTRIC INVESTIGATION OF DEEP CENTERS IN BULK AND MULTILAYERED SEMICONDUCTORS

14
Ivan Turek – Daniel Káčik – Ivan Martinček
TO THE INFLUENCE OF MATERIAL DISPERSION ON THE INTERMODAL INTERFERENCE IN OPTICAL FIBRES

18
Drahoslav Barančok – Július Cirák – Pavol Tomčík – Marek Vančo
MOLECULAR ULTRATHIN LAYERS AND ORDERED SYSTEMS

22
Julius Štelina – Ctibor Musil
THE STUDY OF KINETIC COLLOIDAL PARTICLES IN MAGNETIC FLUIDS USING DIFFRACTION EFFECT ON AN OPTICAL GRATING CREATED BY INTERSECTING LASER BEAMS

26
Sofia Berezina – Oleg Kolosov – Juraj Slabeycius
INVESTIGATION OF LOCAL MECHANICAL PROPERTIES OF Al-Cu-Li ALLOYS BY ACOUSTIC MICROSCOPE

29
D. Pudiš – J. Kováč jr. – J. Kováč – J. Jakabovič
SEMICONDUCTOR LASERS BASED ON QUANTUM WELL STRUCTURES

33
Ivo Čáp – Klára Čápová – Dagmar Faktorová
INTERACTION OF ELECTROMAGNETIC AND ACOUSTIC WAVES IN CONDUCTORS AND ITS UTILIZATION

37
P. Šutta – Q. Jackuliak
X- RAY DIFFRACTION LINE PROFILE ANALYSIS OF STRONGLY TEXTURED THIN FILMS OF ZnO

41
P. Bury – Š. Barta – V. Magula – V. Slugen – T. Šmida
ULTRASONIC INVESTIGATION OF PLASTICALLY DEFORMED STEEL-CONTRIBUTION TO ANALYSIS OF DEGRADATION INFLUENCE

44
Dalibor Blažek – Jozef Kúdelčík – Jozef Blažek
A DESIGN OF AN INDUCTION METHOD DEVICE WITH RESPECT TO THE SIGNAL AND NOISE SENSITIVITY

48
Tadeusz Kasprowicz – Leopold Kruszka – Ryszard Rekucki
DYNAMIC RESPONSE OF A TRUNK STRUCTURE BUILDING TO MULTIPLE TRANSIENT LOADINGS

54
Andrzej Surowiecki – Edward Hutnik
INTERNAL FORCES TESTS IN RETAINING WALLS OF ROAD EMBANKMENTS

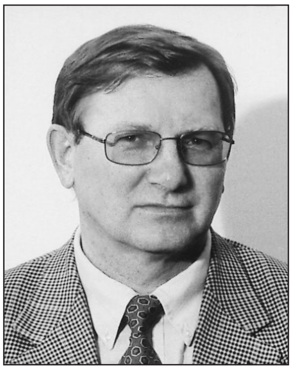

Dear reader,

While, on the one hand, almost all the teachers working in technical departments of our university are convinced that natural sciences and especially physics are necessary for development of new technologies and realization of new technical applications, on the other hand, more and more frequently we come across opinions that diminish the role played by physics in contemporary development of science and technology and, consequently, in educating new technicians.

Discussions whether physics conditions the development of technology or vice versa are useless and never ending. The debates of this kind have no value as there is some truths in both of them. The path from physics to new technical applications is not straightforward, it is more or less spiral. Physics enables development of new technologies and new technologies enable to gather newer knowledge in physics thus creating conditions for new technologies - and the cycle is repeated over and over.

Let us take the following example: a hundred years ago there were no electronic components. Today we can hardly find any electrical device without them. With the birth of quantum mechanics and its applications in a periodic structure the development of electronic materials began. This opened the way to discovery of the transistor, which was followed by a modern era of electronics, computers and communications. This era is today called the „age of informatics". The investigation in stimulated and spontaneous excitation led to the construction of laser, which in turn, serves for transfer of information by means of glass fibers, after the study of interaction of light with condensed matters had been accomplished. Physical studies of nuclear magnetic momentum finally led to magnetic resonance imagining. Many other similar examples showing mutual interconnection of physical and technical research could be mentioned.

It can be concluded that there is a close interrelationship between physics and technology. Although each of them has its own specific principles and procedures, their mutual communication is necessary. They must be bridged with knowledge, objectives and also with personal contacts.

We are grateful for the opportunity given by the editorial board of the Communications to present on the pages of the journal at least a part of results achieved by physicists, mostly from the Department of Physics at the Faculty of Electrical Engineering of the University of Žilina. The papers are evidence of mutual interrelation between physical research and possible technical applications, thus fostering mutual communication between physics and technology, communication among physicists and technicians.

Peter Bury

https://doi.org/10.26552/com.C.2003.2.5-13

Peter Bury – Igor Jamnický – Peter Hockicko *

ACOUSTOELECTRIC INVESTIGATION OF DEEP CENTERS IN BULK AND MULTILAYERED SEMICONDUCTORS

Two basic versions of the acoustic deep-level transient spectroscopy (A-DLTS) technique based on the acoustoelectric effect resulting from the interaction between an acoustic wave and interfaces have been used to study deep centers in semiconductor structures. The former uses the high frequency transverse acoustoelectric signal (TAS) arising from the interaction of surface acoustic wave electric field and free carriers at the structure interfaces. The latter uses an acoustoelectric response signal (ARS) produced by the structure interface when a longitudinal acoustic wave propagates through the structure. An additional version of A-DLTS uses the acoustoelectric effect on light beam generated interface in high resistivity and along with photosensitive semiconductors. Planar Si MIS structure and GaAs/AlGaAs heterostructure capacitors and high resistivity GaAs were investigated by these versions of the A-DLTS technique. Several deep centers were found and their activation energies and corresponding cross-sections determined. Both the appearance of some A-DLTS peaks and the shift of practically all peaks of the A-DLTS spectra with increasing bias voltage in investigated structures can be considered to be the characteristic features of interface states. The polarization and the propagation direction of acoustic waves generated on the light beam produced interface appears as important condition of detected deep centers.

1. Introduction

Semiconductors are the fundamental materials of the electronic industry because their properties can be manipulated over wide ranges through the control of impurities and other imperfections. While shallow impurities generally contribute extra charge carriers, electrons or holes and introduce minor perturbations in the crystal other impurities and a variety of lattice defects (vacancies, antisite defects, self-interstitials, etc.) constitute a more severe local perturbation, give rise to bound states that are considerably more localized, and often have energies deep in the band gap. We know all such impurities, lattice defects, and impurity-defect complexes as deep centers. Unlike shallow impurities the role of which is primarily to control the type and magnitude of conductivity, deep centers act primarily as carrier traps or recombination centers. The deep centers can control the lifetime of charge carriers and as such, deep centers are undesirable in devices where carriers must have long lifetimes, e.g., solar cells. On the other hand, they are useful when the carrier concentration needs to be reduced sharply on a short time scale, as in a fast switch. In addition, when the recombination or carrier-capture energy is released as light, deep centers are used in making light-emitting diodes (LEDs). Finally, many deep centers (vacancies, interstitials, vacancy-impurity complexes, etc.) play a major role in diffusion processes and in reactions that underlie materials modification (e.g., oxidation, recrystallization, etc.).

During the recent past, the semiconductor interfaces in metal-semiconductor contacts, semiconductor-insulator interfaces and semiconductor heterostructures are most important concepts in semiconductor devices and circuits that play a revolutionary role in microelectronics. New technologies, however require smaller devices, sharper transitions and higher number of preparation steps. Narrower transitions require sharper dopping profiles and subsequently lower temperatures during the preparation processes. Lower temperatures introduce defects that hardly can be removed by thermal treatment. These defects represent another new group of fabrication-induced defects.

The microscopic properties and the role of shallow impurities were already quite well understood through combination of theory and experiments in silicon and germanium. Deep centers on the other hand, proved far more difficult to investigate. Over the last thirty years, great progress has been achieved. Many experimental and theoretical techniques were developed and applied to particular systems. The choice of systems was dictated sometimes by technological concerns and sometimes by sheer academic curiosity. In many cases, as new techniques were developed, they were applied to systems that had been extensively studied with earlier techniques. The new information would either confirm, complement and expand existing knowledge about the center, or contradict it and thus lead to new understanding.

The interface deep states of semiconductor structures have been extensively studied and many useful experimental methods have been developed to characterize them [1 – 6]. Following the work of Lang [7], deep-level transient spectroscopy (DLTS) has become most powerful technique commonly used for the characterization of semiconductors and semiconductor structures because it reveals information about several characteristics of electrically or optically active defects present in such materials. Several useful variants of DLTS have been developed [8 – 11] and many attempts

---

* **Peter Bury, Igor Jamnický, Peter Hockicko**
Department of Physics, Faculty of Electrical Engineering, Žilina University, 010 26 Žilina, Slovakia

to improve the defect resolution capabilities of DLTS introducing different types of transient analysis procedure have been reported [12 – 17].

Recently, the acoustoelectric effect in semiconductor structures has been shown to be a useful tool for the experimental study of deep centers and two basic modifications of acoustic deep-level transient spectroscopy (A-DLTS) were introduced. The former surface acoustic wave (SAW) technique uses a nonlinear acoustoelectric interaction between the SAW electric field and the free carriers in an interface region which generates a transverse acoustoelectric signal (TAS) across the structure. Transient measurements of the rise or fall times of the resulting dc and hf part of the TAS have been used to study charged traps [18 – 21]. The latter longitudinal acoustic wave (LAW) technique uses an acoustoelectric response signal (ARS) observed at the interface of the semiconductor structure when a longitudinal acoustic wave propagates through the structure [21 – 23].

Both ARS and TAS are extremely sensitive to any changes in the space charge distribution in the interface region especially due to the trapped charge after an injection pulse has been applied. Their time development represents acoustoelectric transients, which reflect relaxation processes associated with the thermal recombination of excited carriers moving towards their equilibrium state. Using a method of computer evaluation of isothermal acoustoelectric transients by applying a data compression algorithm [24] the activation energies and corresponding capture cross-sections can be determined from transient measurements of acoustoelectric response amplitudes as a technique of A-DLTS.

The technique of acoustic transient spectroscopy based on the utilization of space charge inhomogenity in high resistivity semiconductors produced by non-uniform illumination can be used to bulk deep centers investigation, too. The space charge inhomogenity can generate in proper conditions both the longitudinal and transversal or surface acoustic wave by applying a high frequency electric field [25]. The acoustoelectric transient technique consists then in the analysis of the amplitude time development of such generated acoustic wave after the light is turned off and that is detected by the receiving transducer. The trap states inside the semiconductor band gap are either filed or emptied by an optical illumination. After the external stimulus is removed, the traps either emit or capture charges to move forwards their equilibrium state.

In this contribution we present the principle of the A-DLTS technique as the acoustic spectroscopy technique using both SAW and LAW and describe the experimental procedures based on the computer- evaluation of isothermal acoustoelectric transients by applying a data compression algorithm and method of digital filtering by convolution. The A-DLTS technique has been applied for several kinds of semiconductor structures including Si and GaAs MIS structures, GaAs/AlGaAs heterostructures and high resistivity semiconductors to determine deep center parameters and proved to be an effective method to study deep centers that can play an important role in substrate materials used for electronic devices.

2. Experimental principles and details

The principle of A-DLTS techniques is based on the fact that the time development of the amplitude of the measured acoustoelectric signal (both TAS and ARS) after an injection pulse (electrical or optical) has been applied to the semiconductor structure (p-n junctions, MIS structures, heterostructures, ...) is proportion to the nonequilibrium carrier density, so that the decay time constant associated with the relaxation of the acoustoelectric signal amplitude is a direct measure of the time constant associated with the relaxation processes of injected carriers. The release of carriers from deep center levels that leads to the thermal equilibrium on a new steady state has the time dependence [19]

$$\Delta n(t) = \Delta n_{t0} e^{-\frac{t}{\tau}}, \qquad (1)$$

where Δn_{t0} represents the variation in trap occupancy due to the acoustoelectric field and τ is the time constant associated with the release of the carrier from deep centers when injection pulse is turned off.

The ARS produced by semiconductor structure when a high frequency LAW propagates through the structure is proportional, as in the case of electromechanical capacitance transducer, to the voltage and relative change of capacitance induced by the acoustic wave. For the case of thin planar structure ($d << \lambda$) [22] is given by

$$U_{ac} = \frac{Q}{C_i}\frac{p}{K_i} + \frac{Q}{C_\omega}\frac{p}{K_\omega} = \frac{Q}{C}\frac{p}{K}, \qquad (2)$$

where in the case of MIS structure C_i, C_ω are the capacitances of insulator and space charge region and in the case of GaAs/AlGaAs heterostructure they are the capacitances of the insulating layer between two dimensional electron system (2-DES) and the electrode and the channel capacitance, respectively, C is the total capacitance of the structure, Q is the accumulated charge, p is the acoustic pressure and K is the elastic modulus assuming that elastic modules of the structure layers K_i and K_ω are approximately equal. When a quiescent reverse bias voltage U_G is applied to the MIS structure so that the structure is in deep depletion then for a short time a forward biased injection pulse is superimposed that results in filling of the interface states with majority carriers. After the filling pulse a new non-equilibrium depletion condition is established and due to the thermal emptying of the interface states the accumulated charge and simultaneously the capacitance of the structure is changed. As the ARS is able to reflect changes in the charge distribution in the interface region very sensitively the time development of the ARS after an injection bias pulse reflects relaxation processes associated with the thermally activated emission of excited carriers. From the acoustoelectric investigation of both MIS structures [22] and heterostructures [26] we can conclude that the ARS follows the accumulated charge behavior over the capacitance one.

By presenting the semiconductor structure capacitance as the equivalent capacitance of the series-connected capacitance of the dielectric and depletion layer in the case of MIS structure or the capacitance of insulating and channel layer in the case of

GaAs/AlGaAs heterostructure, the measured acoustoelectric response signal amplitude can be expressed then as follows

$$U^0_{ac}(t) = U^0 \exp(-t/\tau), \tag{3}$$

Since this relation was obtained assuming only one deep center, the result can be readily generalized.

Non-destructive A-DLTS technique represented as SAW technique is based on the fact that the transversal acoustoelectric signal (TAS) arisen from the interaction of SAW electric field and free carriers in semiconductor structures reflect also any changes in the space charge distribution in the interface regions. The resulting electric field that develops across the structure can be expressed by the relation

$$E = E_0 + E_1\, e^{-i(\omega t - kx)}, \tag{4}$$

where E_0 is dc part and E_1 is hf part of TAS, respectively. Using hf part of TAS the acoustoelectric response signal is given by

$$U_{ac} = \int_0^d E_1 \sin(\omega t - kx)dx, \tag{5}$$

where d is the window width.

The special case occurs under the illumination of some part of high resistivity semiconductor by the weekly absorbed light of proper energy when free carriers are generated and the population of trapping centers in the illuminated part alters by the filling or emptying the deep center levels for electrons and holes. The non-equilibrium carriers then can immigrate from the illuminated to dark part of semiconductor and the space charge region arises producing the interface and internal electric field

$$E_{st} = -\frac{kT}{e(n_0 + \Delta n)}\frac{d\Delta n}{dx}, \tag{6}$$

where n_0 is the equilibrium concentration of free carriers and Δn is the concentration of excited electrons or holes. In piezoelectric semiconductor such as high resistivity GaAs, the sample being in the form of bar with its piezoactive direction orientated along the bar, the application of a hf electric field on the region with non-uniform distributed space charge can then lead to the periodic accumulation of electric charge that provides an additional hf electric field [25, 27, 28] and generates an additional acoustic wave. After the illumination is turned off the photo-excited carriers recombine thereby establishing thermal equilibrium by the same way as in the previous cases so that the effect can be used to study deep centers in bulk semiconductors.

The present measurement technique compared with the original A-DLTS that uses the analysis of the acoustoelectric transient signal after an injection pulse similarly as in the Lang's DLTS developed for the capacitance transient by means of a set of emission rate windows [7], the present measurement technique is based on the computer-evaluated transients measured at fixed temperatures. The technique allows a single transient to be sampled at up to 8 different sample rates permitting 3 to 4 decades of time constants to be observed in one thermal scan. The differential ARS or TAS ΔU_{ac} can be then monitored as a function of temperature and peaks with maxim of the temperature for which the emission rate is the same as the adjusted sample rate. Because it is necessary to analyze only enough data to obtain the required information, specifically, the time constants of the transient at each temperature, a data compression algorithm was applied. For example, if 32 767 data points are taken at a base sample rate 4 kHz, one could store the first 256 points, the extract another 256 points from the same transient by 128 averages of 2 points each, followed by extracting 512 points by 128 averages of 4 points each, etc. This storage scheme allows the transient to be observed at 4 kHz for 64 ms, 2 kHz for 128 ms, 1 kHz for 256 ms etc. up to 31.25 Hz for 8.192 s. Thus many decades of time can be sampled from the same transient without permanently storing or processing redundant data. Sixteen transients were averaged per temperature. The temperature is then decreased to next temperature and the process is repeated. Additionally, the hard disk memory required to store such data does not need to exceed 2.3 kbytes per temperature comparing with 64 kbytes without data compression.

The software for the calculation has been thoroughly checked by performing a series of evaluations on computer-generated simulated transients. The purpose of this was to test the capability of the program to properly reveal the emission rates of the transients and the resolution of the method. The computer-evaluation of the observed isothermal ARS transients could be provided by both using Lang's original scheme [23] and correlation procedure with higher order on-line filters and rectangular weighing function [13].

Using the well known relation expressing the temperature dependence of the relaxation time characterizing the acoustoelectric transient [22]

$$\frac{1}{\tau} = \sigma \langle v_{th} \rangle N_c\, e^{-\frac{E_T}{k_T}}, \tag{7}$$

the activation energy, E_T, and corresponding capture cross-section, σ, can be determined. Here $\langle v_{th} \rangle$ is the mean thermal velocity and N_c the effective density of states at the bottom of the conduction band.

A block diagram of the experimental arrangement of the A-DLTS techniques is shown in Fig. 1. The computer system was used to trigger the apparatus, to generate excitation pulses as well as to record and evaluate the isothermal transients of the acoustoelectric signals. A SAW of frequency 10 MHz was generated using an interdigital transducer (IDT) evaporated on the $LiNbO_3$ delay line and the structure to be investigated was placed on the top of the $LiNbO_3$ and pressed against the window (detail-A). A LAW of frequency 4.6 or 13.2 MHz was generated using a $LiNbO_3$ transducer in the arrangement illustrated in detail-B. A fast and slow mode of shear acoustic wave or longitudinal acoustic wave of frequency 13 MHz were generated on high resistivity GaAs through both the piezoactivity and additional acoustoelectric effect on space charge inhomogenity by applying hf electric field pulses along its $\langle 110 \rangle$ direction and detected by shear and/or longitudinal quartz transducer (detail-C). The schematic illustration of the time arrangement of some experimental parameters corresponding to the isothermal transients scanning process is given in Fig. 2.

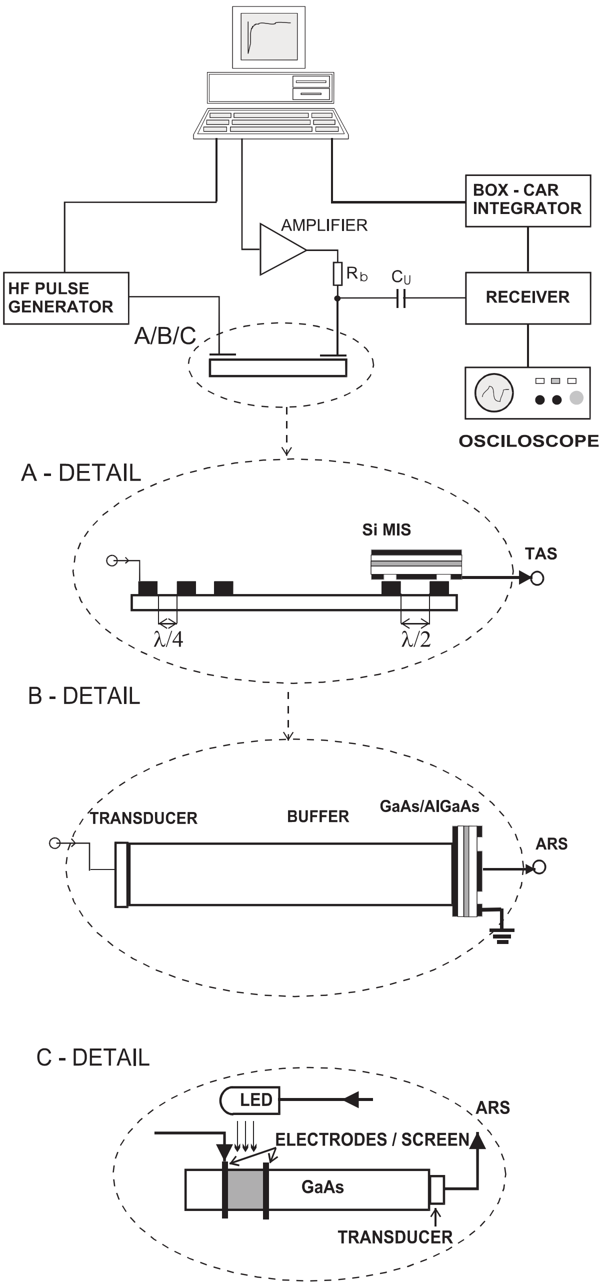

Fig. 1. Block diagram of the experimental arrangement for A-DLTS measurements. The detailed sample configurations are illustrated in A-detail (TAS measurement), B-detail (ARS measurement) and C-detail (illumination generated interface).

The both quiescent bias voltage pulse and illumination pulse with pulse width of 100 – 200 ms filling traps completely were applied to the structures and semiconductors, respectively using the computer with analogous – digital converter. The IR-LED with the maximum in spectral characteristic of 900 nm was used for the illumination The acoustoelectric signal produced by the structure after detection in the receiver was selected by the box-car integrator and then recorded and stored by computer.

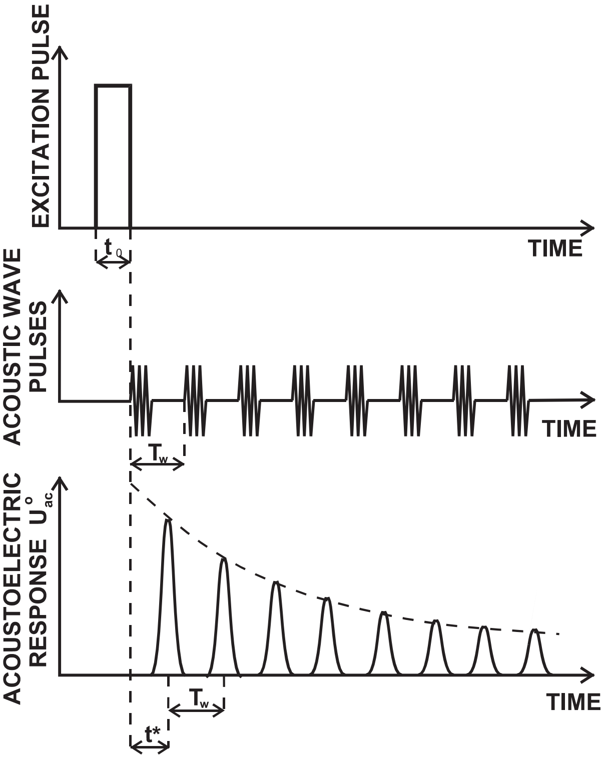

Fig. 2. Schematic illustration of the time arrangement of some experimental parameters, t_o is the injection pulse width, $f_w = 1/T_w$ the rate frequency and t^+ the transverse time through the buffer rod.

The well known Si MOS structures were firstly investigated to verify the principles of the above described method – Acoustic DLTS. The Al-SiO$_2$-Si capacitors were fabricated both on n-type Si substrates with (100) surface orientation and 2.6 to 2.8 Ωcm resistivity and on p-type Si substrates with the same orientation and 8.0 to 8.7 Ωcm resistivity. The oxide layers were grown by CVD technique to thickness 80 nm. Aluminum was deposited onto the insulator layer using a vacuum evaporation. Oxide from the backside of the wafer was removed and Al or Ag was deposited to provide the back contacts.

We have also investigated three different GaAs/AlGaAs heterostructures, which have been grown by MBE on semi-insulating (SI) GaAs substrates and prepared in the form of planar structure with two dimensional electron system – 2 DES (NU 169 and NU 1787) and two dimensional hole system – 2 DHS (NU 1323) at heterojunction. The first relatively simple investigated heterostructure (NU 169) consisted of the following layers: SI buffer layer, 2 μm; undoped AlGaAs spacer layer, 20 nm; n-type doped AlGaAs layer with 1×10^{18} cm^{-3} Si, 40 nm; SI GaAs capping layer, 20 nm. The 2 DES was located at the interface between the SI GaAs layer and the AlGaAs spacer layer. Two ohmic contacts were made to reach the 2 DES layer. The schematic illustration of the heterostructure arrangement is in Fig. 3.

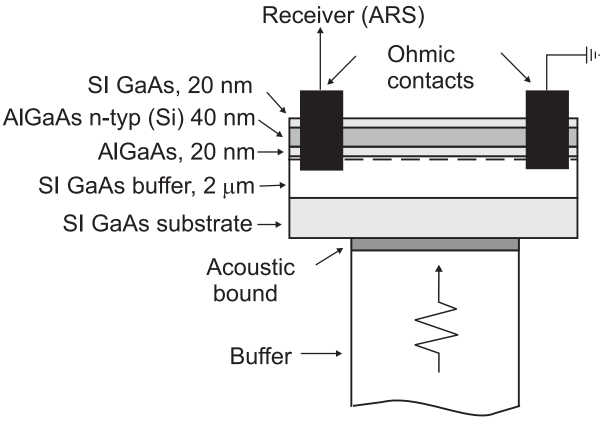

Fig. 3. Schematic illustration of experimental and layers arrangement of investigated GaAs/AlGaAs heterostructure (NU-169).

Another two heterostructures, NU 1787 and NU 41323 had similar layer structures consisting of superlattice. The layer structure of the sample NU 1787 consisted of the following layers: undoped GaAs, 1 μm; superlattice GaAs (2.5 nm)/AlGa (2.5 nm), 50×; undoped GaAs, 0.5 μm; undoped AlGa, 50 nm; n-type doped AlGa with $n = 5.1017$ cm^{-3}, 80 nm; undoped GaAs, 17 nm. The third heterostructure (NU 1323) with 2 DHS contained: undoped GaAs, 1 μm; superlattice GaAs/AlGa, 5 nm (50×); undoped GaAs, 0.5 μm, AlGa layer, 80 nm; p-type doped AlGa layer with $n = 5 \times 1017$ cm^{-3}, 80 nm; undoped GaAs, 17 nm. The 2 DES and 2 DHS were located between undoped GaAs and AlGa layers.

The fast and slow mode of transversal acoustic wave (T_1 and T_2) and longitudinal acoustic wave (L) of frequency 13 MHz were generated through the acoustoelectric effect on space charge inhomogenity produced by illumination through the metal screen on high resistivity Cr-doped GaAs applying hf electric field pulses in $\langle 110 \rangle$ direction and detected by transverse and longitudinal quartz transducers, respectively. The surface acoustic wave (SAW) of frequency 10 MHz was generated in $\langle 001 \rangle$ direction and detected by IDT evaporated directly on the sample rod.

3. Results and Discussion

Using the above-described techniques the development of the ARS as a function of temperature was for the first time investigated for Si MIS structures mentioned in the previous part. Fig. 4 shows typical ARS transients measured at various temperatures and the same bias voltage conditions for p-type Si MIS structure. These transients contain only one exponential component corresponding to 0.3 eV trap. Fig. 5 represents a series of A-DLTS signals calculated from the isothermal ARS transients for various time constants (sampling times) using the correlation analysis with first order filter. Fig. 6 shows the series of A-DLTS spectra for different bias voltages applied to the Si MIS structure and the same time constant. As indicated by both the $C - UG$ and $U_{ac} - U_G$ measurements, by increasing U_G towards negative values the SiO$_2$ − Si interface region passes from deep depletion to nearly accumulation state. As it is shown in Fig. 6, peaks of the A-DLTS spectra are shifted to lower temperature with the increasing bias pulse voltage, that is characteristic features of the interface states [8].

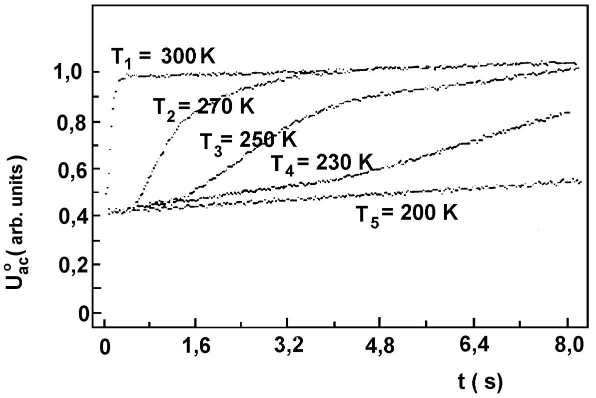

Fig. 4. Typical ARS transients recorded at various temperature.

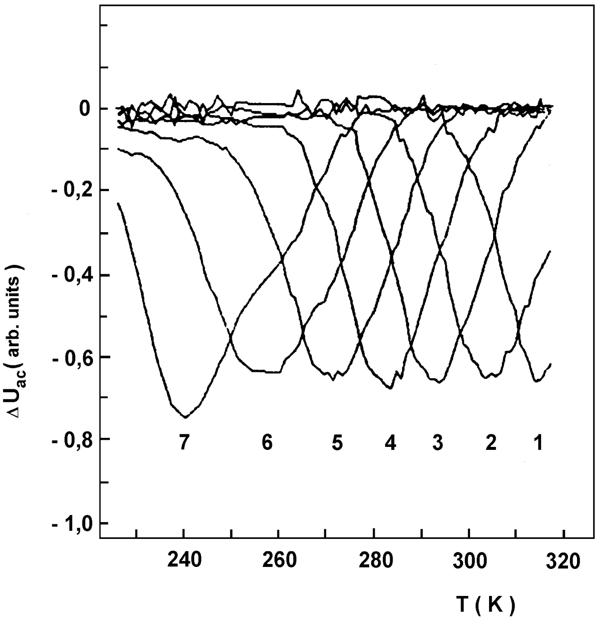

Fig. 5 A set of A-DLTS spectra calculated from isothermal transients for various relaxation times τ, from 18,4 ms (1) to 1,178 s (7) measured at $U_G = 4$ V.

The activation energies and corresponding capture cross-sections were determined from the Arrhenius plots (Fig. 7) constructed for the individual peaks from the A-DLTS spectra at different biases using the relation expressing the temperature dependence of the relaxation time characterizing the acoustoelectric transient. The obtained energy levels 0.47, 0.30 and 0.25 eV above the valence band edge with the cross sections 4.8×10^{-17}, 1.0×10^{-19} and 1.5×10^{-20} cm^2 corresponding to the bias voltages 2, 4 and 6 V, respectively confirm the energy distribution of the interface states that is in a reasonable agreement with the many results found by DLTS and other techniques and are attributed to various defects [5, 6, 29 - 31]. The measurement in the inversion state ($U_G = 9$ V) showed the energy level 0.60 eV with corresponding capture cross-section 4.8×10^{-13} cm^2. As the A-DLTS signal originates from the capture of electrons from the valence band into the trap level (hole emission process) and this appears as the negative signal in A-DLTS spectra [22], we believe that observed levels are deep acceptor levels.

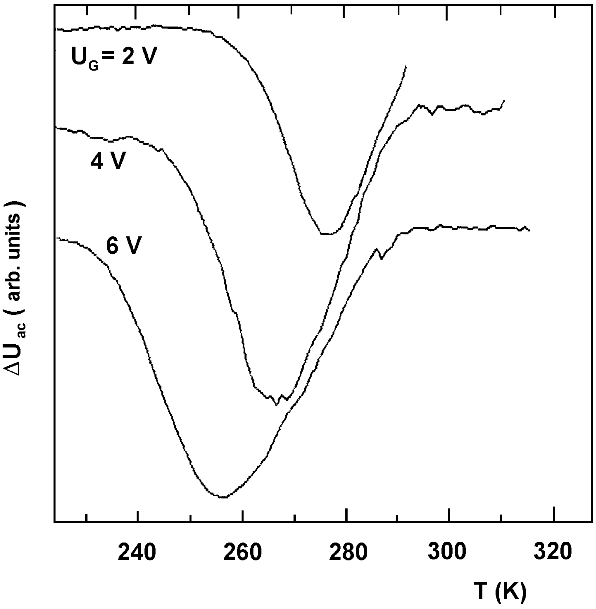

Fig. 6 A-DLTS spectra obtained from ARS transients as a function of bias voltage applied to the p-type Si MIS structure, $\tau = 0.2945$ s.

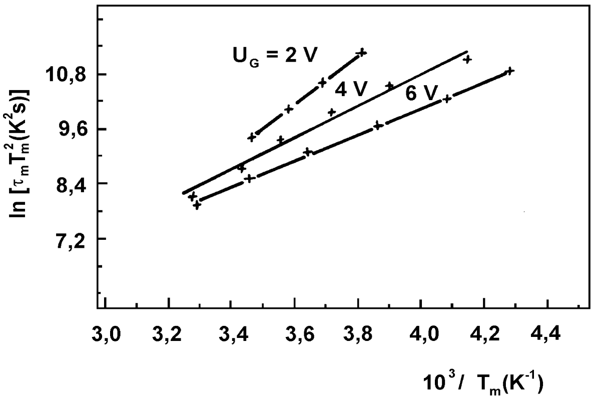

Fig. 7 Arrhenius plots constructed and calculated from the positions of the peak maxim using the A-DLTS spectra at different biases $U_G = 2,4$ and 6V.

Fig. 8 represents a series of A-DLTS signals calculated from the isothermal acoustoelectric transients for various bias voltages applied to the n-type Si MIS structure. Both the $C - U_G$ and $U_{ac} - U_G$ measurements indicate that by increasing U_G towards positive values the SiO$_2$-Si interface region passes from the depletion state to the a state close to accumulation. The decreasing of UG under -6V indicated that an inversion state is created. The peaks of the A-DLTS spectra were shifted to lower temperature with the decreasing bias pulse voltage that again represents the characteristic features of the interface states. The obtained energy levels 0.52, 0.59 and 0.67 eV and the cross sections 2.1×10^{-15}, 8.0×10^{-14} and 4.6×10^{-12} cm^2 corresponding to bias voltages -3, -5 and -6V, respectively, confirm the energy distribution of the interface states that is in a reasonable agreement with the results found by DLTS and other techniques [6, 32]. In spite of the fact that the energy level position 0.54 eV below the conduction band edge agrees with values mostly found for the bulk impurities and some structural defects it seems to be characteristic also for interface states. The measurements for the inversion state ($U_G = -9$V) showed the energy levels at 0.35 eV and 0.32 eV with corresponding capture cross sections 1.8×10^{-17} cm^2 and 5.9×10^{-19} cm^2, respectively. While the former energy level represents interface traps of donor character, the latter represents hole trap observed in the inversion layer [22].

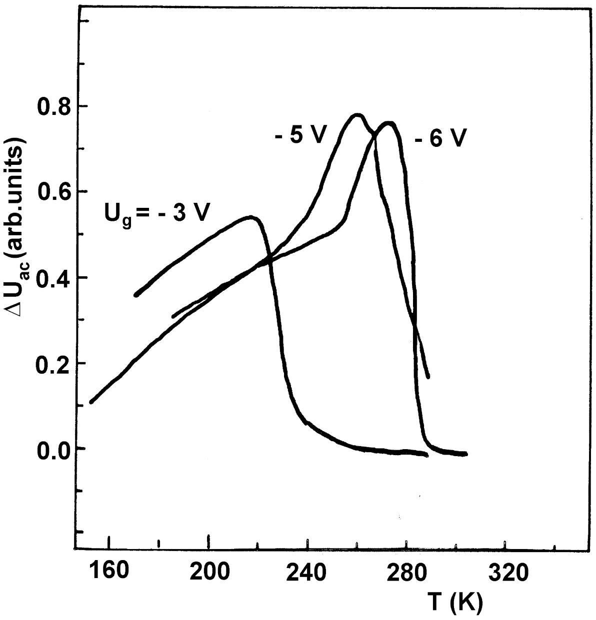

Fig. 8 A-DLTS spectra obtained from ARS transients as a function of bias voltage applied to the n-type Si MIS structure, $\tau = 0{,}1472$ s.

Representative optically induced A-DLTS spectra of all investigated samples GaAs/AlGaAs with both 2 DES and 2 DHS obtained from acoustoelectric transients are illustrated in Fig. 9. The A-DLTS spectrum of NU-169 sample contains three evident peaks representing three deep centers. The activation energies and corresponding capture cross-sections determined from the Arrhenius plots constructed for the individual peaks of A-DLTS spectra have the values: 0.29 eV (1), 0.26 eV (2), 0.21 eV (3) and 2.9×10^{-16} cm^2 (1), 5.2×10^{-16} cm^2 (2), 1.8×10^{-15} cm^2 (3), respectively. While two of them, (1) and (2), have a donor character, the last center is of an acceptor type.

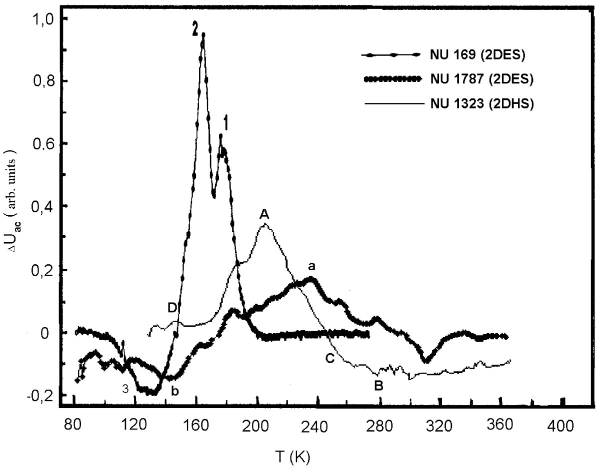

Fig. 9. A-DLTS spectra of investigated GaAs/AlGaAs heterostructures obtained for a relaxation time $\tau = 0.0368$ s.

All obtained deep centers are well known from the measurements obtained by DLTS or other techniques, however never in the same composition. The deep centers with the energy level 0.29 eV were detected in GaAs/AlGaAs heterostructures [33], but also in GaAs layers prepared by MBE technique [34]. The deep center with energy 0.26 eV is known also as DX center [35], sometimes with energies of 0.25 – 0.28 eV. Deep center of acceptor character with energy 0.21 eV was detected in both GaAs/AlGaAs or GaAs layers prepared by MBE technique [35, 36]. Some measurements [35] indicated even internal structure of obtained peaks like superposition of two different peaks similar as in our optically induced A-DLTS measurements [38].

The appearance of two broader peaks corresponding to deep centers of different type with some structure of smaller peaks is the characteristic feature of A-DLTS spectra obtained on NU 1787 sample containing also 2 DES. The activation energies of 0.29 eV (a) and 0.10 eV (b) with corresponding cross-sections of 2.2×10^{-18} cm^2 (a) and 5.5×10^{-21} cm^2 (b), respectively were determined as parameters characterizing these deep centers. It should be noted that the A-DLTS signal at this case was much smaller (presented A-DLTS spectrum is even ~ 2× amplified) comparing to previous spectrum and smaller peaks could not be easily used to deep centers characterization. The deep centers of acceptor type characterized by activation energy close to the value 0.1 eV and not detected in previous sample were obtained in GaAs/AlGaAs heterostructures by SAW technique using dc TAS [18] and also by ordinary DLTS measurements [33].

The A-DLTS spectrum of NU-1323 sample with 2 DHS recorded by applying an optical injection pulse contains one dominant peak (A) and three weaker ones (B-D). Using Arrhenius plots, the following activation energies and corresponding capture cross-sections were determined: 1.29 eV (A); 0.33 eV (B); 0.73 eV (C); 0.61 eV (D) and 1.8×10^{-19} cm^2 (B); 9.2×10^{-12} cm^2 (C); 1.5×10^{-12} cm^2 (D), respectively. In spite the fact that some of the obtained deep centers (B-D) were registered also by other transient techniques using both electrical and optical pulse excitation [33, 36, 37], they are typical for acoustical transient measurements [2, 10] and deep center (A) characterized with relatively high activation energy, 1.29 eV and large cross-section ($\sim 10^{-4} - 10^{-6}$ cm^2) is known, except acoustic transient measurements [20, 28], only from TSC measurements [39].

As it can be seen the obtained values of activation energies are mostly in good agreement with the values found by both optically induced and other transient spectroscopy techniques and attributed to deep centers or other defects. The experimental arrangement indicates that detected deep centers should be localized close to the 2 DES or 2 DHS. However, some features found only by acoustic transient spectroscopy still remain unclear.

Fig. 10 and Fig. 11 show a typical A-DLTS spectra obtained for Si MIS structures and GaAs/AlGaAs heterostructures by non-destructive SAW A-DLTS technique, respectively. Using the above mentioned procedure, the activation energies and capture cross-sections, summarized in Table 1, were calculated from the Arrhenius plots constructed for individual peaks of A-DLTS spectra.

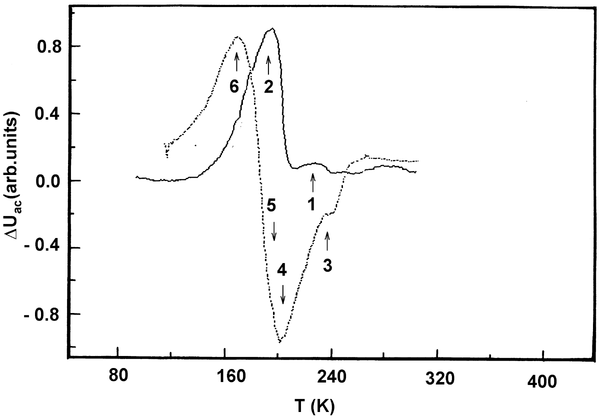

Fig. 10. A-DLTS spectra of Si(n) and Si (p) MIS structures obtained by SAW technique.

The obtained values are mostly in good agreement with the values found by DLTS or others techniques [18, 24, 29, 30, 32, 40]. Comparing the presented results with those obtained by A-DLTS technique using longitudinal acoustic wave (Fig. 6 and Fig. 8) the energy levels are shifted because of the acoustoelectric transverse dc voltage is added to the excitation bias voltage.

Fig. 12. represents A-DLTS spectra of Cr-doped GaAs obtained for various generated acoustic waves (fast transversal T_1, slow transversal T_2, longitudinal L and SAW) and calculated from the isother-

mal acoustoelectric transients. The activation energies and corresponding capture cross-sections determined from the Arrhenius plots are summarized in Table 2.

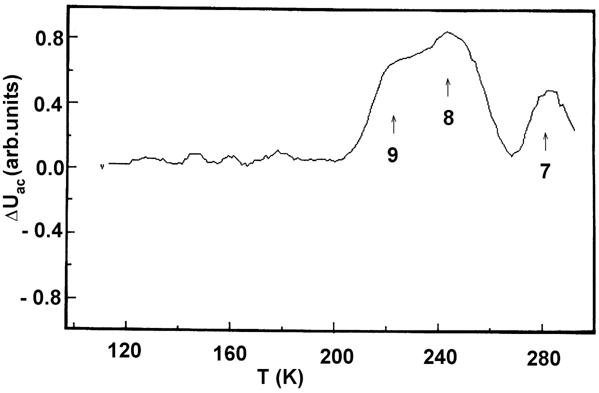

Fig. 11. A-DLTS spectra of GaAs/AlGaAs heterostructure obtained by SAW technique.

Summary of the deep centers parameters detected by SAW A-DLTS in Si MIS and GaAs/AlGaAs heterostructures Table 1

Label	Structure	E[eV]	σ[cm^2]	$-U_G$ [V]
1	Si(n) MIS	0.37	7.8×10^{-17}	3.0
2	Si(n) MIS	0.21	4.7×10^{-19}	3.0
3	Si(p) MIS	0.49	3.3×10^{-13}	4.0
4	Si(p) MIS	0.67	5.2×10^{-11}	4.0
5	Si(p) MIS	0.47	6.5×10^{-13}	4.0
6	Si(p) MIS	0.61	3.4×10^{-6}	4.0
7	GaAs/AlGaAs	0.47	1.3×10^{-14}	5.0
8	GaAs/AlGaAs	0.39	6.6×10^{-16}	5.0
9	GaAs/AlGaAs	0.67	2.7×10^{-12}	7.0

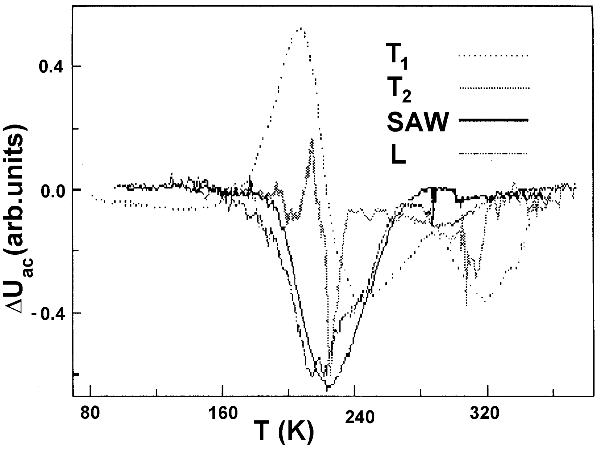

Fig. 12. Optically induced A-DLTS spectra of Cr-doped GaAs obtained for various acoustic waves (fast transversal T_1, slow transversal T_2, longitudinal L and SAW)

Summary of the centers parameter detected in high resistivity GaAs for various acoustic waves Table 2

Propagation Direction	Polarization	Deep Centers	
		E [eV]	σ[cm^2]
[110]	[001] (T1)	1.28	3.1×10^{-4}
		0.72	2.4×10^{-13}
		0.47	3.0×10^{-15}
		0.31	4.8×10^{-18}
		0.27	2.1×10^{-18}
		0.35	1.7×10^{-16}
		0.22	4.1×10^{-18}
[110]	$[1\bar{1}0]$ (T_2)	1.10	1.6×10^{-6}
		0.79	1.1×10^{-11}
[110]	[110] (L)	0.74	5.1×10^{-12}
		0.32	2.0×10^{-7}
[001]	(SAW)	0.77	2.5×10^{-17}

Most of the obtained energy levels of deep centers are in good agreement with the values found by the other techniques [36, 37, 42] that have been already compared and discussed [41].

The comparison of the results obtained for different acoustic waves (T_1, T_2, L, SAW) generated on the same sample and mostly for the same screen indicates that the interaction of acoustic wave and deep centers depends both on the propagation direction and on the polarization of generated acoustic wave.

4 Conclusion

In conclusion, the acoustoelectric investigation using the acoustic transient spectroscopy technique represented by several various versions we presented can be successfully used to study the deep centers in semiconductors and semiconductors structures. Several deep centers attributed to the interface states in Si MIS structures, GaAs/AlGaAs heterostructures with both 2 DES and 2 DHS and high resistivity GaAs were discovered and their parameters were determined.

The presented and for deep centers investigation used acoustoelectric transient technique induced also some advantages comparing with the other transient techniques: the acoustoelectric signal is produced directly by a heterojunction containing space charge so that any changes in its distribution are immediately reflected by the ARS and/or TAS; the number and thickness of individual insulating layers at the heterostructure does not influence obtained acoustoelectric response; the quality of the ohmic contacts does not play so important role as in electric techniques.

Acknowledgements The authors would like to thank Dr. O. Mikuš (MIS structure) and Dr. M. Henini (GaAs/AlGaAs heterostructures) for the growing of the layers and Mr. F. Černobila for technical assistance. This work was partly supported by Grant No.1/8308/01 of the Slovak Ministry of Education.

References

[1] TERMAN, L.: *Solid State Electronics 5*, (1962) 285.
[2] NICOLLIAN, E. H., GOETZBERGER, A., BERGLUND, C. N.: *Appl. Phys. Letters 15* (1969) 174.
[3] YOUNG, D. R., IRENE DI MARIA, E. A., De KEERSMAECKER, R. F.: J. *Appl. Phys. 50* (1979) 6366.
[4] TSENG, W. L.: *J. Appl. Phys. 62* (1987) 591.
[5] PATER, K.: *Appl. Phys. A 44* (1987) 191.
[6] HUNG, K. K., CHENG, Y. C.: *J. Appl. Phys. 62* (1987) 4204.
[7] LANG, D. V.: *J. Appl. Phys. 45*, (1974) 3023.
[8] YAMASAKI, K., YOSHIDA, M., SUGANO, T.: *J. Appl. Phys. 18* (1979), Japan, 113.
[9] KIROV, K. I., RADEV, K. B.: *Phys. Stat. Sol.* (a) 63 (1981) 711.
[10] TURCHANIKOV, V. I., LYSENKO, V. S., GUSEV, V. A.: *Phys. Stat. Sol.* (a) 95 (1986) 283.
[11] SCHULZ, M., JOHNSON, N. M.: *Appl. Phys. Letters 31* (1977) 622.
[12] DOOLITTLE, W. A., ROHATGI, A.: *Rev. Sci. Instrum 63* (1992) 5733.
[13] CROWELL, C. R., ALIPANAHI, S.: *Solid St. Electron. 24* (1981) 25.
[14] WANG, C. W., WU, C. H., BOONE, B. L.: *J. Appl. Phys. 73* (1993) 760.
[15] DOBACZEWSKI, L., KACZOR, P., HAWKINS, I. D., PEAKER, A. R.: *Appl. Phys. 76* (1994) 194.
[16] DMOWSKI, K.: *Solid State Electronics 38* (1995) 1051.
[17] THURZO, I., GMUCOVÁ, K.: *Rev. Sci. Instrum 65* (1994) 2244.
[18] TABIB-AZAR, M., HAJJAR, F.: *IEEE Transactions on Electron Devices 36* (1989) 1189-1195.
[19] ABBATE, A., MAN, K. J., OSTROVSKIJ, I. V., DAS, P.: *Solid State Electronics 36* (1993) 697.
[20] BURY, P., JAMNICKÝ, I.: *Proc. 16th Int. Congr. on Acoustics*, Vol. I, Seattle, (1998) 429.
[21] BURY, P., JAMNICKÝ, I., RAMPTON, V. W.: *Physica B 263-264* (1999) 94.
[22] BURY, P., JAMNICKÝ, I., ĎURČEK, J.: *Phys. Stat. Sol.* (a) 126 (1991) 151.
[23] JAMNICKÝ, I., BURY, P.: *Phys. Stat. Sol.* (a) 139 (1993) K35.
[24] BURY, P., JAMNICKÝ, I.: *Acta Phys. Slovaca 46* (1996) 693.
[25] BURY, P., HOCKICKO, P., JAMNICKÝ, I.: *Proc. 17th Int. Congress on Acoustics*, Rome, Vol. I, 2001.
[26] BURY, P., RAMPTON, V. W., CARTER, P. J. A., McENANEY, K. B.: *Phys. Stat. Sol.* (a) 133 (1992) 363.
[27] ŠTELINA, J., BRACINÍK, J.: *Appl. Acoustic 44*, (1995) 369.
[28] BURY, P.: *Proc. 16th Int. Congr. on Acoustics*, Vol. I, Seattle, (1998) 431.
[29] KAR, S., NARASIMHAN, R. L.: *J. Appl. Phys. 61*, (1987) 5353.
[30] DAI, Z.: *Solid State Electronics 32*, (1989) 439.
[31] McLARTY, P. K., COLE, J. W., GALLOWAY, K. F., IOUNNOU, D. E., BERNACKI, S. E.: *Appl. Phys. or 13.2 MHz was Letters 51*, (1989) 1087.
[32] HOFMAN, F., KRAUTSCHNEIDER, W. H.: *J. Appl. Phys. 63*, (1989) 1358-1360.
[33] AS, D. J., EPERLEIN, P. W., MOONEY, P. M.: *J. Appl. Phys. 64* (1988) 2408.
[34] WANG, C. W., WU, C. H.: *J. Appl. Phys. 74* (1993) 3921.
[35] ENRIQUEZ, L., DUENAS, S., BARBOLA, J., IZPURA, I., MUÑOZ, E.: *J. Appl. Phys. 72* (1992) 525.
[36] DARMO, J., DUBECKÝ, F., KORDOŠ, P., FORSSTER, A.: *J. 393 Luth, Mat. Science B 28* (1994) 4393.
[37] MARTIN, G. M., MITONNEAU, A., MICREA, A.: *Electr. Lett. 13* (1977) 193.
[38] BURY, P., HOCKICKO, P., RAMPTON, V. W.: *Acta Phys. Slovaca* (will be published).
[39] LIN, A. L., BUBE, R. H.: *J. Appl. Phys. 47* (1976) 1859.
[40] OKUMURA, M., MISAWA, S., YOSHIDA, S.: *Surface Science 174* (1986) 324-330.
[41] BURY, P., JAMNICKÝ, I.: *World Congress on Ultrasonics*, Berlin (1995) 535.
[42] BURY, P.: *Proc. 16th Int. Congress on Acoustics*, Vol. I, Seattle (1998) 431.
[43] DUBECKÝ, F., SAFRÁNKOVÁ, J., OLEJNÍKOVÁ, B.: *Crystal Properties & Preparation 12* (1987) 147-152.

https://doi.org/10.26552/com.C.2003.2.14-17

komunikácie
COMMUNICATIONS

Ivan Turek – Daniel Káčik – Ivan Martinček *

TO THE INFLUENCE OF MATERIAL DISPERSION ON THE INTERMODAL INTERFERENCE IN OPTICAL FIBRES

The comparison of computed and measured spectral dependence of intermodal interference in step-index optical fibre presented in this paper shows the influence of material dispersion on the intermodal interference in optical fibres. It is shown that the influence of material dispersion on intermodal interference is high enough to allow determination of the material dispersion difference of core and cladding of optical fibres.

1. Introduction

The meaning of the term *"dispersion"* is not determined unambiguously. In the papers devoted to physics problems it is used for expression of the fact that some quantity depends on the wavelength (frequency) of the light [1] or on the wavelength of the wave used at a quantity determination. This term is often used for expression of derivation of particular quantity on the wavelength. Most often the term dispersion is used for expression of derivation of material refractive index or derivation of phase velocity of the light on the wavelength – i.e. dispersion d (taken as quantity) is determined by relation

$$d = \partial n / \partial \lambda .$$

For telecommunications purposes, the wavelength dependence of pulse transition time is important, so the critical parameter is not the phase velocity, but the group velocity of transmitted signal. Since the group velocity v_g is equal to

$$v_g = v + k \frac{\partial v}{\partial k} = v - \lambda \frac{\partial v}{\partial \lambda}$$

where v is the phase velocity and k is the absolute value of the wave vector. So the spectral dependence of the pulse delay, determined with the group velocity dispersion, is characterised by the dispersion constant [2, 3]

$$D = \frac{\lambda}{c_0} \partial^2 n / \partial \lambda^2$$

where c_0 is the velocity of light in vacuum.

The phase velocity dispersion as well as the group velocity dispersion can be determined from the known wavelength dependence of the refractive index. There are a lot of sufficiently accurate methods for determination of the refractive index wavelength dependence in bulk materials. However, if it is to determine the dispersion of optical fibres, the problem arises. For determination of the core or cladding refractive index it is necessary to localise the lighting to an area smaller than the core diameter, that is, to the area with diameter of a few μm. The sufficient illumination of so small area is possible, practically, only with lasers. But lasers are usually not wavelength-tuneable and tuneable only in a small region of wavelengths, respectively. To avoid the problems at determination of the material dispersion of optical fibres the investigation of intermodal interference of optical fibre can be used.

2. Influence of dispersion on interference of modes

As it is known, a study of the intermodal interference in optical fibres can be performed if the signal dependence given by interfering modes is detected with non-uniform sensitivity. The detection sensitivity in places where the phase of detecting modes is the same should differ from the places where their phases are opposite [4 – 7]. At such detection the influence of orthogonality of interfering modes is eliminated.

Taking into account the different phase constants of the modes, we can express the output of the quadratic detector located at the end of the fibre of length z as follows:

$$s(z) = \int_S c(x, y) \cdot \sum_i \psi_i(x, y, z) \cdot \sum_i \psi_i^*(x, y, z) \cdot dxdy \qquad (1)$$

where $c(x, y)$ is the detector sensitivity, $\psi_i(x, y, z)$ are the functions describing the propagating modes and are equal to $\psi_{i,0}(x, y) \cdot \cdot \exp(j\beta_i z)$, where $\psi_{i,0}$ are the modal functions, β_i are the phase constants of particular modes, x and y are the coordinates perpendicular to the direction of the propagation, S is area on which the modal function is nonzero and "*" denotes complex conjugation. The expression (1) gives after some manipulation for the signal:

$$\begin{aligned} s(z) = & \int_S c(x, y) \sum_k \psi_{k,0}(x, y) \cdot \psi_{k,0}^*(x, y) \cdot dxdy + \\ & + \int_S c(x, y) \sum_{l \neq k}^{0} \psi_{l,0}(x, y) \cdot \psi_{k,0}^*(x, y) \cdot \\ & \cdot \exp(j \cdot (\beta_l - \beta_k) z) \cdot dxdy . \end{aligned} \qquad (2)$$

---

* [1]Ivan Turek, [2]Daniel Káčik, [1]Ivan Martinček
[1]Department of Physics, University of Žilina
[2]Department of Telecommunications, University of Žilina

The first term on the right side of Eq.(2) represents the sum of particular mode intensities and does not depend on the length of waveguide and only weakly depends on the wavelength (the dependence is only because of the dependence of the modal functions on wavelength).

The second term on the right side of Eq.(2) is the interference term. It is clear that while the sensitivity c does not depend on coordinates its value is zero, because

$$\int_S \psi_{l,0}(x,y) \cdot \psi^*_{k,0}(x,y) \cdot dxdy = 0 \quad \text{for} \quad l \neq k. \tag{3}$$

At a suitable dependence of detector sensitivity on coordinates, the interference term can be nonzero. The interference term of two modes of a monochromatic light with wavelength λ, according the relation (2), is

$$\mathrm{s}(\mathrm{y}, \lambda) = \int_S c(x,y) \cdot \psi_{l,0}(x,y) \cdot \psi^*_{k,0}(x,y) \cdot$$

$$\cdot \exp(j \cdot (\beta_l - \beta_k)z) \cdot dxdy \tag{4,a}$$

or

$$s_{int}(z, \lambda) = s_0 \cdot \cos(\Delta\beta_{l,k}(\lambda)z) \tag{4,b}$$

where $\Delta\beta_{l,k}(\lambda) = \Delta\beta_l(\lambda) - \Delta\beta_k(\lambda)$, indexes l,k correspond to interfering modes and

$$s_0 = \int_S c(x,y) \cdot \psi_{l,0}(x,y) \cdot \psi^*_{k,0}(x,y) \cdot dxdy. \tag{4,c}$$

If we investigate intermodal interference of modes in the light of finite spectral width $\Delta\lambda$, the interference term (4) should be modified. As waves with different frequencies participate in the interference of mode, the term has to be rewritten in the form

$$s_{int}(l, \lambda) = s_0 \cdot \int_{\Delta\lambda} \cos(\Delta\beta_{l,k}(\lambda) \cdot z) \cdot \zeta(\lambda) \cdot d\lambda \tag{5,a}$$

where z is the length of the fibre and $\zeta(\lambda)$ is the spectral density of the light. As ζ depends on λ only slightly, the Eq. (5,a) can be rewritten into

$$s_{int}(l, \lambda) = s_0 \, \bar{\zeta} \cdot \int_{\Delta\lambda} \cos(\Delta\beta_{l,k}(\lambda) \cdot z) \cdot d\lambda \tag{5,b}$$

where $\bar{\zeta}$ is the average value of ζ in the region $\Delta\lambda$.

In Fig.1. the typical curve of transmission function of fibre with nonzero interfering term is shown. As it can be seen from the dependence shown in this figure, the spectral dependencies of experimental observing curves have a character corresponding to the expression (5).

The harmonic character of interference term given by equation (4) (or its modified form (5)) allows to separate the interference term from the measured transmission function. The spectral dependence of interference term obtained from the measured transmission function drawn in Fig. 1. is presented in Fig. 2. In this figure there is also calculated spectral dependence of interference term of the first two modes. It was calculated for such parameters of fibre (values of refractive index of core and cladding, radius of core and length of the fibre) for which the interference centre λ_0 [8] corresponds to the measured interference centre and the periodicity of the dependence is in the maximal agreement with the measured one.

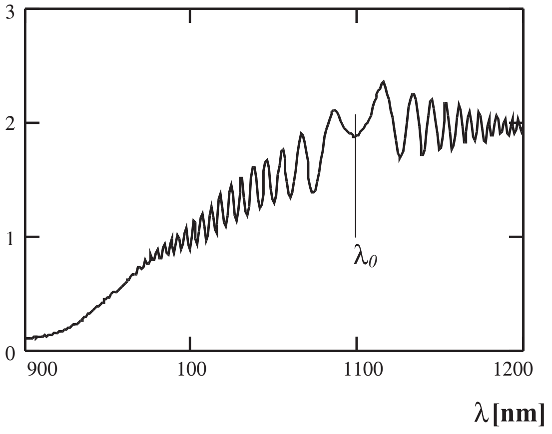

Fig. 1. Spectral dependence of transmission function (in arbitrary units) with significant interference term measured on Siemens fibre.

It can be seen from comparison of these dependencies that their character is the same but the periodicity of the calculated dependence does not correspond to the measured one.

The difference of measured and calculated curves drawn in Fig. 2 is caused by the fact that the phase constants β_l and β_k (which determinate the phase difference of interfering modes) depend on the wavelength not only explicitly, but also through the wavelength dependence of refractive index of core and cladding. This means that $\Delta\beta$ (and the periodicity of signal too) is a function of material dispersion of the core and the cladding. So the interference of modes can be used as an information source of fibre material dispersion.

It follows from the previous that the interference of modes depends on *difference* of material dispersion of fibre's core and cladding, but not on the dispersion itself. The core or the cladding of the fibre is often made from pure silica (for which the dispersion is very well known), so the material dispersion difference, which can be evaluated by studying the intermodal interference, allows to determine the material dispersion of the non-silica material built in the optical fibre.

The following "model example" illustrates the influence of material dispersion on the intermodal interference and possible use of intermodal interference for its determination.

When it is assumed that the wavelength dependence of refractive index of core is the same as it is in pure silica, i.e.

$$n_{co} = 1.4471 + 0.014396\ (\lambda - 1.1 \cdot 10^{-6}\,\mathrm{m})/1.1 \cdot 10^{-6}\,\mathrm{m}$$

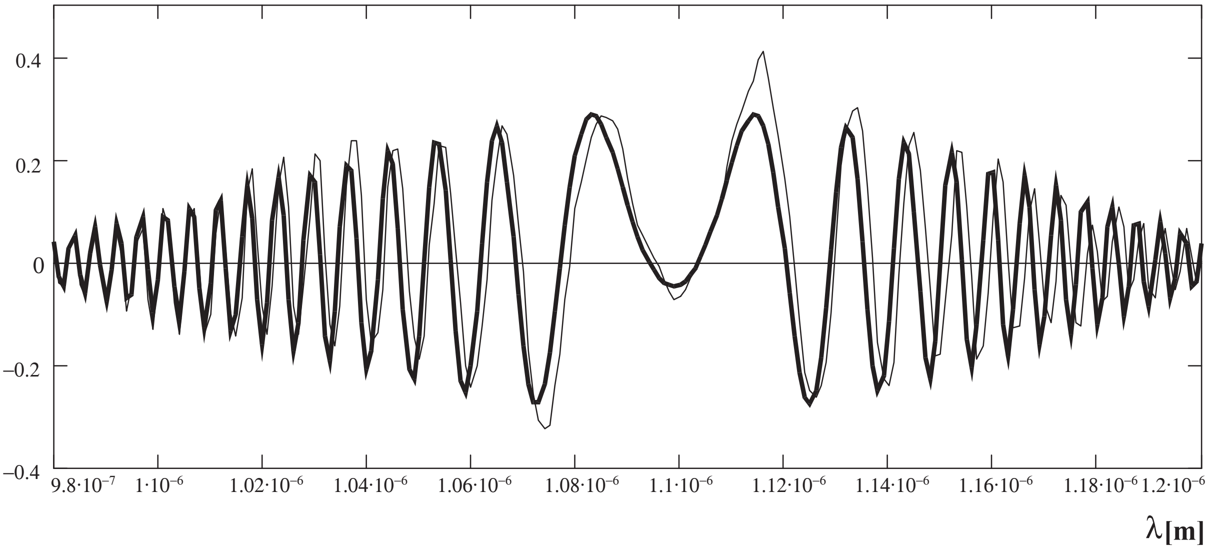

Fig. 2. The comparison between measured —— and computed interference term with constant refractive indexes ▬▬ . Values are plotted in arbitrary units.

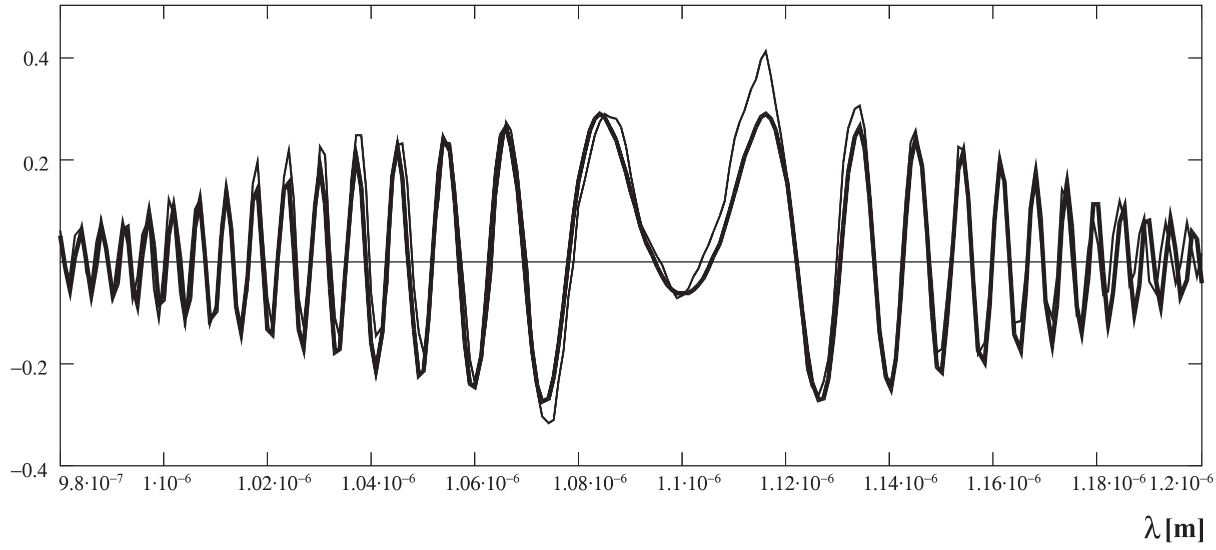

Fig. 3. The comparison between measured —— and computed interference term with linear dependence of dispersion ▬▬. Values are plotted in arbitrary units.

and that the refractive index of cladding is

$$n_{cl} = 1.443299 - 0.01445\ (\lambda - 1.1\cdot 10^{-6}\ \mathrm{m})/1.1\cdot 10^{-6}\ \mathrm{m}$$

the dependence of phase constants difference of the first and second modes calculated for weakly-guiding step-index optical fibre of length 0.72 m, gives spectral dependence of interference term which is drawn in Fig.3.

The difference of the interference term calculated at that assumption and the measured dependence is smaller than error of measurement in the area of the wavelengths 0.8 to 1.16 μm. In the area close to 1.2 μm a difference between computed and measured dependencies is seen. This difference can be eliminated introducing a quadratic dependence of cladding refractive index. When the refractive index of cladding in area from 1.13 to 1.2 μm is assumed to be greater than that one which was taken into account for the curve given in Fig. 3. by the value equal to $3.05\ 10^{8}\ (\lambda - 1.13\cdot 10^{-6})^{2}$, then practically full correspondence of the measured and calculated dependencies is obtained in all investigated region (Fig. 4.).

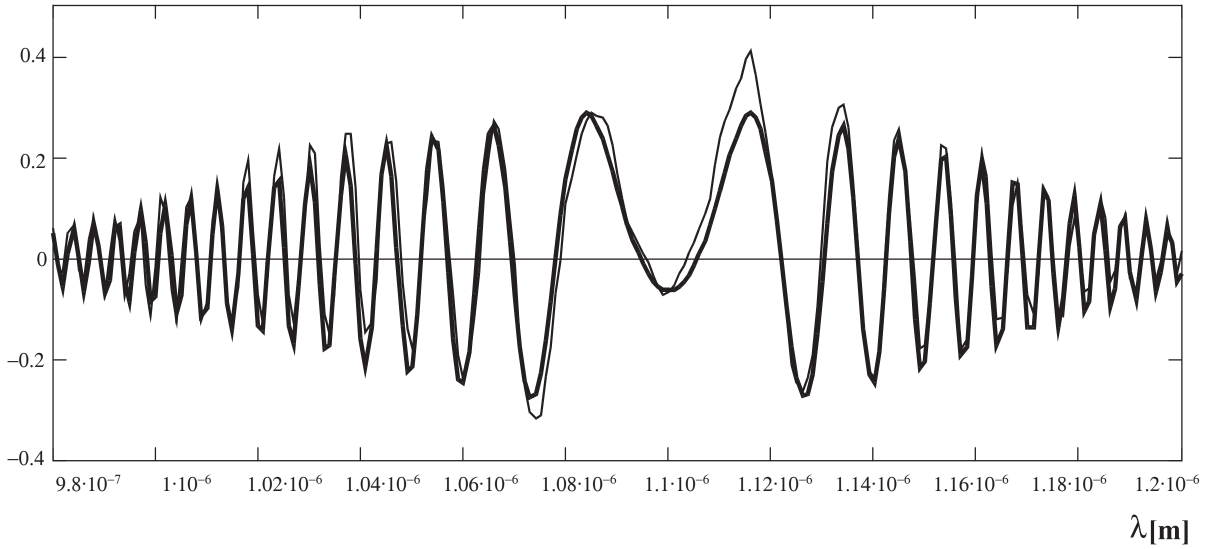

Fig. 4. The comparison between measured —— *and computed interference term with linear and quadratic dependence of refractive index being a function of wavelength (group velocity dispersion)* ━━ *. Values are plotted in arbitrary units.*

3. Conclusion

The presented example shows that spectral dependence of interference term reflects the wavelength dependence of refractive index in a very sensitive way. This sensitivity is so high that the study of intermodal interference can be used not only for examination of geometrical parameters of fibres [7, 8] (radius of core, refractive index profile) but also for determination of material dispersion of investigated fibres.

Technical equipment used in our laboratory allows to measure spectral dependencies with precision of 1 nm of the wavelengths. In the previous paragraph it was showed that such precision allows to observe influence of spectral dependence of interference of modes and to determine its derivation on the wavelength. If the wavelength region in which the interference term is registered is wide enough, it allows also to estimate the second derivation of the difference of indices of the core and the cladding.

Nowadays, in good laboratories there is no problem to determine spectral dependencies with accuracy higher than 0.1 nm. Such precision allows to determine the first and the second derivation of refractive indices also if intermodal interference is observed in an area of wavelengths smaller than the area, which was necessary in our measurement in the presented model example.

References

[1] BORN, M., WOLF, E.: *Principles of Optics*, Cambridge University Press, 2002, p. 95.
[2] KEISER, G.: *Optical fiber communications*, McGraw-Hill, 2000, p. 107.
[3] DADO, M., TUREK, I., ŠTELINA, J., BITTERER, L., TUREK, S., GROLMUS, E., STIBOR, P.: *Kapitoly z optiky pre technikov*, Žilinská univerzita, 1998, p. 316.
[4] TUREK, I., MARTINČEK, I., STRÁNSKY, R.: *"Interference of modes in optical fibers,"* Opt.Eng., vol. 39, 1304-1309, 2000
[5] POSEY, R., PHILLIPS, L., DIGGS, D., SHARMA, A.: *"LP01-LP02 interference using a spectrally extended light source: measurement of the non-step-refractive-index profile of optical fibers,"* Opt. Lett., vol. 21, 1357-1359, 1996
[6] HLUBINA, P.: *"Spectral detection schemes for the low-coherence based two-mode fibre waveguide sensors"*, Poceedings SPIE, vol. 2510 (Fiber Optic and Laser Sensors XIII, Munich 1995), pp. 213-223.
[7] ARCHAMBAULT, J. L., BLACK, R. J., BURES, J., GONTHIER, F., LACROIX, S., SARAVANOS C.: *"Fiber core profile characterization by measuring group velocity equalization wavelengths,"* IEEE Photon. Technol. Lett., vol. 3, 351-353, 1991
[8] MARTINČEK, I., TUREK, I., DADO, M., GRONDŽÁK, K., ČERNICKÝ, S.: *"Interferencia módov v optických vláknach"*, Komunikácie/Communications 2/2000.

https://doi.org/10.26552/com.C.2003.2.18-21

Drahoslav Barančok – Július Cirák – Pavol Tomčík – Marek Vančo *

MOLECULAR ULTRATHIN LAYERS AND ORDERED SYSTEMS

Monomolecular assemblies on substrates, now termed Langmuir-Blodgett (LB) films, exhibit many interesting properties and can perform functions which give them perspectives to impact advanced technologies and molecular electronics in an important way. In this article we briefly present our recent efforts aimed at the study of nanoelectric phenomena in the Langmuir monolayer formed on a water surface as well as electrochemical properties of Langmuir-Blodgett films deposited on the surface of an ultramicroelectrode involved in microsensors.

1. Introduction

Information processing technology currently uses inorganic semiconductor structures. Such structures are fabricated in an essentially planar array on the surface of silicon or gallium arsenide, and have been progressively smaller, primarily by advances in lithography. However, the cost of each successive reduction now increases so much that a practical limit may be approaching. In addition, there are severe physical limits which hinder further progress in miniaturisation. An alternative approach is to start with molecules as basic building blocks, and to assemble the molecules together in a controlled manner so as to create a structure with designed electronic function.

This paper describes a design of systems assembled by the Langmuir-Blodgett (LB) technique. The origin of the present interest in LB films can be traced back from the early 60s, to the works of H. Kuhn [1] who recognized the utility of LB technique as a tool to assemble molecules in a systematic and well-defined manner. The LB technology is based on two successive steps: formation of an organic monomolecular layer of amphiphilic molecules on the surface of water, and transfer of the monolayer onto the solid substrate by its traversal through the air/water interface (Fig. 1). The monolayer is literally a two-dimensional system built of ordered molecules. The preferential orientation of the molecules with a permanent electric dipole results in spontaneous polarization in the monolayer. The conformational and/or orientational changes of the monolayer constituting molecules induced by external stimuli (illumination, chemical reactions, surface pressure) can be monitored by measuring Maxwell's displacement current [2]. The capability of LB technique can be demonstrated by the production of high sensitive electrochemical devices. Their improvement has been introduced by modification of electrodes, e.g. coating the surface with an organic film. Several deposition techniques have been exploited. We tested a new approach in electrode modification: the LB method was applied for this purpose. Significantly enhanced sensitivity of the determination of metal ions in the water solution is demonstrated by the calibration curves obtained for both the bare and the coated ultramicroelectrodes.

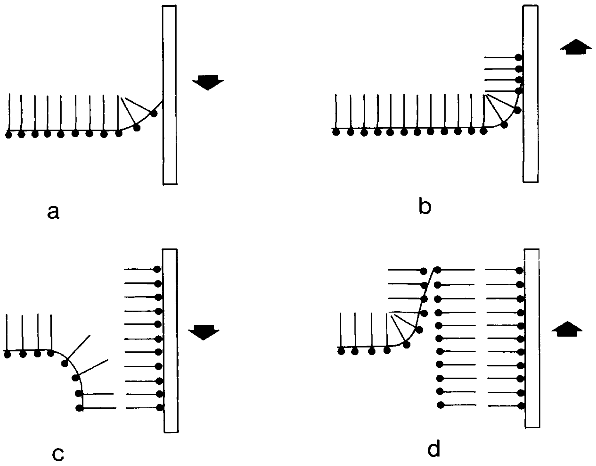

Fig. 1

2. Nanoelectric phenomena in Langmuir monolayer

We introduced a modified version in which the top electrical contact is detached from the upper surface and the Maxwell displacement current (MDC) is detected in the metal/air gap/Langmuir monolayer/metal structure. MDC flows when the vertical component of the polar molecule changes with time. For this reason, the MDC measuring system is suitable for detecting dielectric relaxation phenomena in a monolayer at the air/water interface. We discuss the evaluation procedure of the molecular dipole moment and some remarks are devoted to the dielectric ralaxation phenomena accompanying the orientational ordering and disordering of monolayers by applying lateral monolayer compression.

Fig. 2 shows the experimental setup in this investigation [3]. The top electrode – *TE* – (the area is $S = 20$ cm^2) was suspended in air, parallel to the water surface. The air gap between *TE* and the surface was adjusted to $d = 0.5$ mm with the aid of a micrometer by monitoring the capacitance of the system. The displacement current was detected by a Keithey 517 electrometer (A). The sensitivity of measuring a current was 0.1 fA. The measuring system

---

* **Drahoslav Barančok, Július Cirák, Pavol Tomčík, Marek Vančo**
Department of Physics, Faculty of Electrical Engineering and Information Technology, Slovak University of Technology, Ilkovičova 3, 812 19 Bratislava,
E-mail: barancok@elf.stuba.sk, cirak@elf.stuba.sk, tomcik@elf.stuba.sk, vanco@elf.stuba.sk

was attached to the computer-controlled Langmuir trough (NIMA Technology, UK) and placed in a dust-free compartment on an antivibrating block.

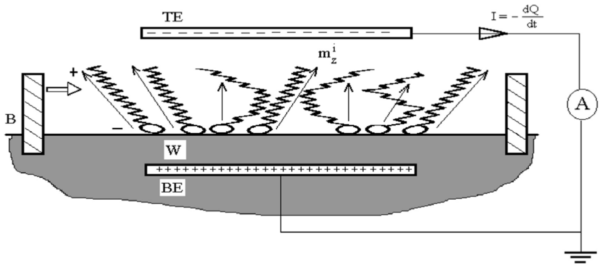

Fig. 2

As a surface-active substance, straight-chain hydrocarbon stearic acid (SA) was used, purchased from Lachema (Brno, Czech Republic). Stearic acid was dissolved in chloroform (1 mmol/l solution) and slowly added to the surface of bidistilled water to form a single monolayer at the air/water interface. The Langmuir trough was of a rectangular shape with the total working area of 600 cm^2. The compression rates varied between 20 and 120 cm^2/min, which corresponded to about 0.05 to 0.30 A/s per a molecule.

The displacement current in the circuit originates from three components [4]:

$$I = \frac{N}{d}\frac{dM}{dt} + \frac{M}{d}\frac{dN}{dt} + \frac{\epsilon_0 S}{d}\frac{d\Phi}{dt} \tag{1}$$

The first contribution arises from the change in the vertical component of the molecular dipole moment (M), the second contribution is connected with the change in number of molecules (N) between the electrodes. The third component was taken as zero because the surface potential of water Φ may be considered constant during the monolayer compression.

A typical recording of the Maxwell displacement current detected simultaneously with the surface pressure (π) – area per molecule (A) isotherm during the lateral compression of the monolayer is presented in Fig. 3. The current maximum indicates that the molecules become aligned perpendicularly to the interface. The area under $I - t$ dependence can be utilized for calculation of the change in the induced charge on electrode 1 and, hence, for the calculation of the molecular dipole moment. The value 2.5×10^{-30} Cm or 0.75 D was found for stearic acid molecule. The Maxwell displacement current measurement has been also applied to detect the vertical component of the dipole moment in a poly (3-alkylthiophene) derivative which is able to give a stable monolayer on the water surface. The value 5.5×10^{-30} Cm (or 1.65 D) are in good agreement with the value obtained from the molecular mechanics calculation [5].

The external compression of the monolayer on a water surface with an aid of a movable barrier can be used for studying non-equilibrium phenomena. For this purpose, the motion of the barrier was not continuous but regularly interrupted so as to allow the monolayer to reach an equilibrium state after stopping the barrier. The transient process was monitored by measuring the displacement current across the monolayer. Experiment showed that the dielectric relaxation time, i.e. the period needed for the monolayer to acquire a new equilibrium state, depends on the monolayer area A and hence on the molecular orientational order. At the beginning of the compression (low orientational order) the transient process is relatively slow ($\tau \sim 3$ s). On the other hand, in the state when the molecules stand upright at the air/water interface responds to external compression stimulation much faster ($\tau = 1$ s). This observation can be supported by the theoretical consideration based on the Debye theory for studying the rotational Brownian motion of molecules with permanent electric dipoles [6].

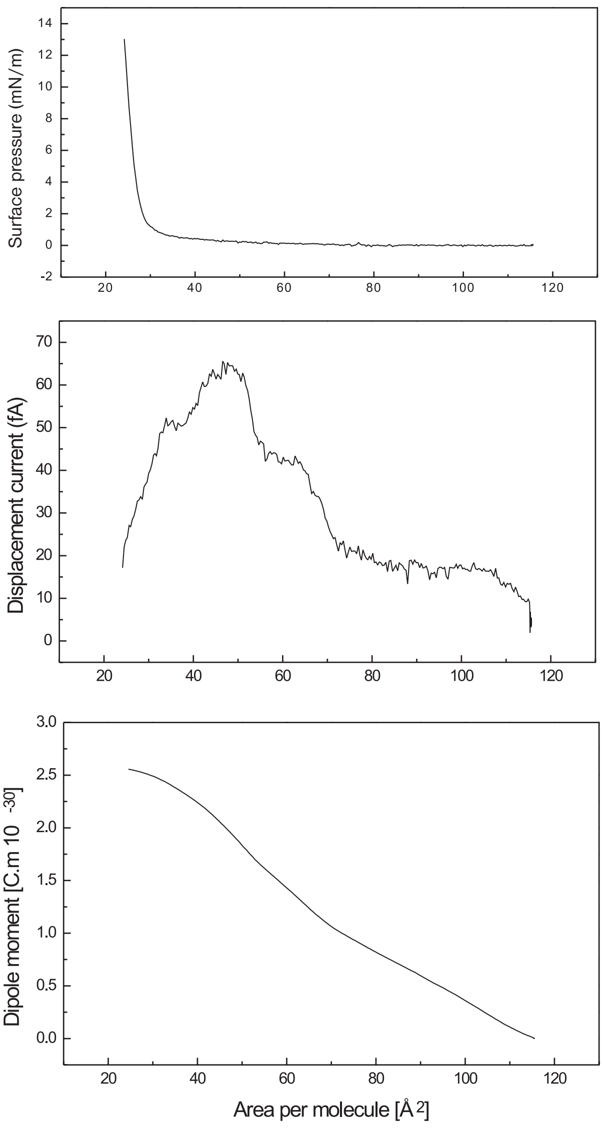

Fig. 2

3. Molecular layer as a surface modifier

The improvement of sensitivity and selectivity of the electrochemical detection system has been introduced by modification of the electrode surface, i.e. coating the surface with thin film for the purpose of immobilizing a specific redox reagent. The superior property of the LB coating method is the capability of depositing a defined number of monolayers (layer-by-layer) of the modifier at ambient temperature, i.e. even a monomolecular-layer coverage is feasible. Substituted polythiophenes were used in the role for the electrode coating, namely amphiphilic poly (3-alkylthiophenes), whose structure (see Fig. 4b) is adjusted to the requirements of the LB process.

The mechanism of charge transport in the layer of a modifier is crucial for kinetics of the charge transfer between the electrode surface and the solution probed. Electrochemical behaviour of both untreated and coated working electrodes was tested by means of double-step voltcoulometry (DSVCM). In this method, the time dependence of the charge transient in response to a potential step is studied at elevating potential applied to electrodes. The kinetic sensitive DSVCM has been presented recently [7]. All the electrochemical experiments were conducted in a two-electrode cell. The carbon fibre working electrode comprised two or three fibres (each 7 μm in diameter) protruding from a wax-filled capillary (see Fig. 4a). An Ag/AgCl/ electrode was used as a reference. Standard solutions of Cu were used in testing the working electrode.

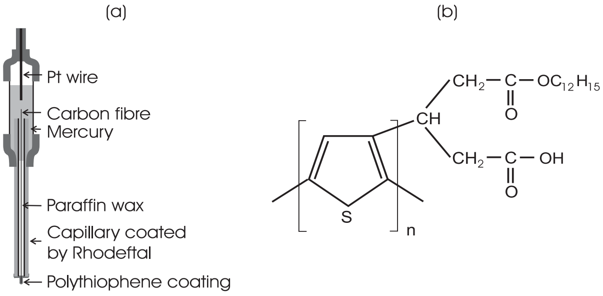

Fig. 4

The detection ability of the carbon electrode is documented in Fig. 5 where the signal maximum from Cu ions situated at ca. -0.3 V is dependent on the concentration of the species in the solution probed. On the other hand, the signal maximum was considerably raised by the formation of the electrode coating with polythiophene (Fig. 6). The presented potential region *U* is restricted to the interval, which is dominated by the presence of ions in the electrode redox reaction. Straight calibration lines were observed for a concentration range between 20 and 100 ng/ml (with a detection limit of 5 ng/ml) as shown in Fig.7. The slope of the calibration lines which refers to the sensitivity increases with the number of polymer monolayers and reaches its limit at 10 – 12 layers (thickness of the coating being ca. 18 nm). The detection process is reversible and the electrode coated by polymer does not "remember" the situation from the previous solution.

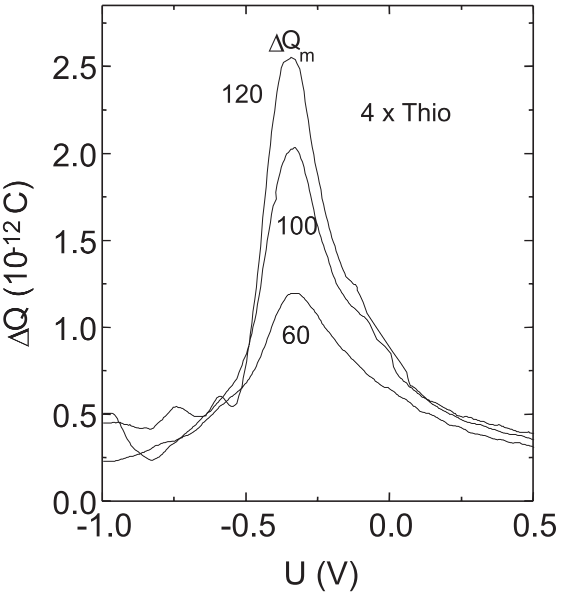

Fig. 5

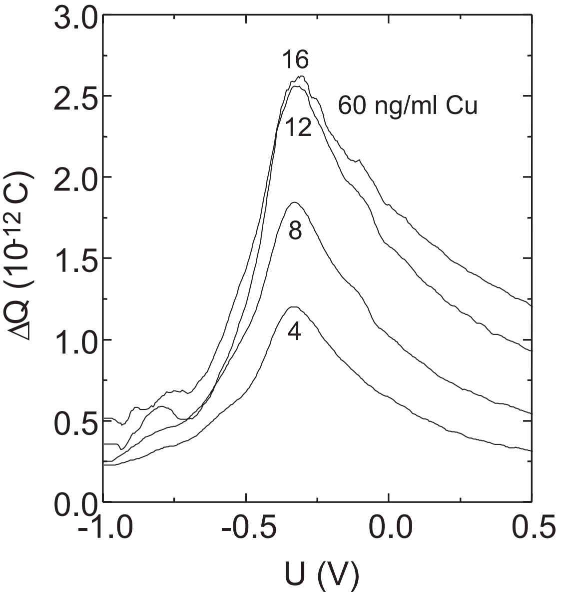

Fig. 6

4. Conclusions

When defining the role of LB layers in materials science in the new decade and beyond, not only should potential applications be considered but, first of all, the understanding of the molecular assembly in two dimensions at the molecular level is the basis in the technique of materials. Interest is given to the system composed of several types of molecules where the molecular interactions play a key role in determining the resultant system properties. But the interactions depend on the way how the molecules are spontaneously organized in the system – depend on self-orga-

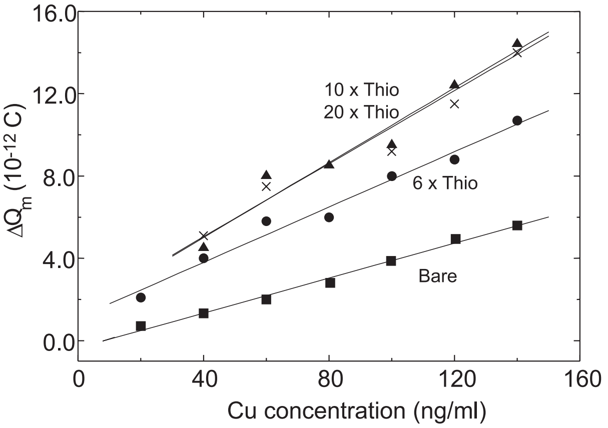

Fig. 7

nization. From this point of view LB films can be regarded as an ideal technological tool for modeling basic physical processes in the system with molecular organization and this impact of the research should be understood and put forward in any concept.

More direct practical goals of the research of organic molecular systems are emerging in these areas: development of electrochemical microsensors, nonlinear optical systems (the use of spontaneous orientation of molecules in the layers, molecular-level control on film thickness, generation of higher harmonics) and development of novel materials for the control of friction and wear (tribology).

References

[1] KUHN, H.: *Naturwissenschaften 54* (1967), 429.
[2] IWAMOTO, M., MAJIMA, Y.,: *J. Chem. Phys. 94* (1991), 5135.
[3] BARANČOK, D., CIRÁK, J., TOMČÍK, P., VAJDA, J.: *Phys. stat. sol.* (a) 169 (1998), 503.
[4] IWAMOTO, M.: *Thin Solid Films 244* (1994), 1031.
[5] CIRÁK, J., TOMČÍK, P., BARANČOK, D., BOLOGNESI, A., RAGAZZI, M.: *Thin Solid Films 402* (2002), 190.
[6] IWAMOTO, M.: Ch. X. Wu, *Phys. Rev. E54* (1996), 6603.
[7] THURZO, I., GMUCOVÁ, K., ORLICKÝ, J., PAVLÁSEK, J.: *Rev. Sci. Instrum. 70* (1999), 3723.

https://doi.org/10.26552/com.C.2003.2.22-25

Julius Štelina – Ctibor Musil *

THE STUDY OF KINETIC COLLOIDAL PARTICLES IN MAGNETIC FLUIDS USING DIFFRACTION EFFECT ON AN OPTICAL GRATING CREATED BY INTERSECTING LASER BEAMS

In this paper a short characteristic of magnetic fluids and some of their applications are presented a simple one-dimensional model of creation of thermal and absorption grating is explained. The method of generation of optical grating by using the interference two intersecting coherent laser beams is presented. In conclusion some possibilities of utilisation optical created grating are also indicated.

1. Introduction

Magnetic fluids are colloidal suspensions of single domain ferromagnetic particles Fe or Fe_3O_4, or other particles dispersed in a carrier liquid as, for example, water, mineral oil, etc. The particles, whose diameter is placed in the region (5 ÷ 20) *nm*, could not set down due to Brownian motion. These particles interacted via the long-range magnetic forces and short range Van der Waals forces. Mutual interaction of these particles causes formation of agglomerates and then their sedimentation, and the long time stabilisation of the colloidal solution is ensured by surfactant. The surfactant covers the particles and thus essentially suppresses interaction. As surfactant matter a detergent or alcohol and so on is usually used.

The first magnetic fluid was prepared in 1938 by Elmore [1], in order to see the magnetic domains in some ferromagnetic materials. The Papell [2] developed the magnetic fluids in 1965 in connection with the cosmic program of NASA. In this case, will the fluid being the part of the fuel made it possible to transport fuel into rocket engine in weightless state. The next authors developed the ultra – stabilised fluids with cobalt particles, with different carrier liquids and different surfactants. The magnetic saturation was higher than in the case of the Fe_3O_4 particles. It turned out that the magnetic fluids share the hydrodynamic and the magnetic properties. These are very interesting for fundamental physical research and some technical application too. Now, we remind that the magnetic fluid can be used as the seal of very speedy rotating shafts. In this case the magnetic fluid plays the role of the packing ring. The magnetic fluid can be used as a filling of space, in which the coil of the loudspeaker oscillates, this secures the axial alignment.

At present the magnetic fluids find their application in biomedicine when the medicaments are purposefully transported [3], in radio-diagnostic as of a contrast-medium [4], etc.

2. Creation of thermal grating – one-dimensional model

If the sample of fluid containing colloidal particles is illuminated by the light whose intensity is harmonically varied on the direction perpendicular to the direction of the propagation of the light beam the fluid will be heated harmonically due to light absorption.

It is possible to obtain the harmonic dependence of the intensity of the light, using two coherent intersecting laser beams (Fig. 1).

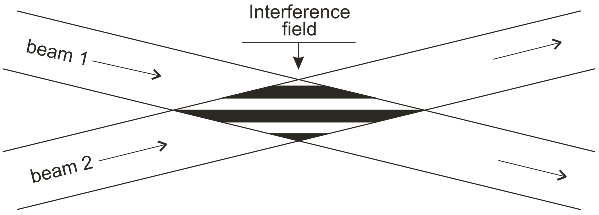

Fig. 1

When the sample of fluid is put into the interference field, the harmonic thermal field is created in the place where the beams are intersecting [5]. Harmonic variation of temperature will result in the thermal diffusion exchange of the colloidal particles between the places with different temperatures. This disturbs the equilibrium distribution of the particles (their concentration) and the diffusion due to concentration variations of particles starts between these places. After certain time the dynamic equilibrium takes place between these two processes and the periodical distribution of temperature and concentration of particles will be settled. Due to changes of the index of refraction the phase grating is created and due to the changes of concentration of particles the absorption grating is created too. The self-diffraction of light arises in this grating. When the interference field is switched off, the thermal

---

* **Julius Štelina, Ctibor Musil**
Department of Physics, University of Žilina, Veľký diel, 010 26 Žilina, Slovak Republic,

optical grating vanishes after the relatively short time (of the order of few milliseconds), while the absorption grating exist essential a longer time. The destruction of the absorption grating can be observed through the decrease of diffracted beam intensity. This fact allows us to study the dynamics of the colloidal particles in the fluid.

The diffusion flux of particles in the created grating, in one-dimensional case can be written

$$\frac{\partial n}{\partial t} = -D \cdot \frac{\partial^2 n}{\partial x^2} - S \cdot \frac{\partial^2 T}{\partial x^2} \tag{1}$$

In this equation n is the concentration of particles, t is time, D means the diffusion constant of magnetic particles, S is the thermal-diffusion coefficient (Soret constant), T is the temperature and x is the co-ordinate. In the case when the illumination is harmonic the equation (1) can be written as

$$\frac{\partial n}{\partial t} = -D \cdot \frac{\partial^2 n}{\partial x^2} - S \cdot D \cdot T_0 \cdot n_0 \cdot \Omega^2 \cdot \sin(\Omega \cdot x) \tag{2}$$

where T_0 is the amplitude of periodic modulation of the sample temperature, n_0 means density of the particles and $\Omega = \frac{2 \cdot \pi}{\Lambda}$ is the space frequency of the grating (Λ is the grating constant).

The solution of this equation is

$$n(x, t) = n_0 \cdot S \cdot T_0 \cdot (1 - \exp(-D \cdot \Omega^2 \cdot t) \cdot \sin(\Omega \cdot x) \tag{3}$$

From this term we can see that the amplitude of the particle density in equilibrium is

$$n_s = n_0 \cdot S \cdot T_0 \tag{4}$$

We can also see from Eq. (3), that after the heating is switched off the concentration grating decreases exponentially with time constant

$$\tau = \frac{1}{D \cdot \Omega^2} \tag{5}$$

Using grating constant Λ the diffusion constant D can be expressed as

$$D = \frac{\Lambda^2}{8 \cdot \pi^2 \cdot \tau} \tag{6}$$

From this we can see that τ is a quadratic function of the grating constant according to the expression

$$\tau = \frac{1}{8 \cdot \pi^2 \cdot D} \Lambda^2. \tag{7}$$

It is known that the diffusion coefficient is connected with mobility μ of the particles by Einstein's relation

$$D = \mu \cdot k \cdot T, \tag{8}$$

where $k = 1.38 \cdot 10^{-23}\, J \cdot K^{-1}$ is the Boltzmann constant

In the first approximation we will assume that the particles are of spherical shape. Then the viscosity of the based fluid can be expressed according to the equation

$$\eta = \frac{1}{6 \cdot \pi \cdot \mu \cdot r} = \frac{k \cdot T}{6 \cdot \pi \cdot D \cdot r}, \tag{9}$$

where r is the effective radius of the colloidal particles. We use the Poisson relation which determines the connection between the force acting on the spherical particles and their mobility.

3. Experiment and results

The principal scheme of the set-up created in our department of physics is demonstrated in Fig. 2.

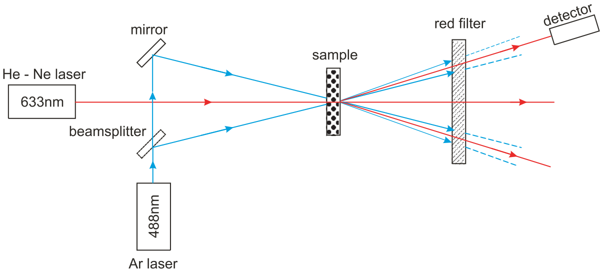

Fig. 2

The Ar laser beam (488 nm) is divided with a beam-splitter into two coherent beams with the small trajectory difference. The sample of magnetic fluid, with thickness in the region (60 ÷ 150) μm was placed in coherent intersecting laser beams, where the interference field is present (Fig. 1). The interference field creates the thermal grating in the fluid due to absorption of the light. We can observe either self-diffraction or the optical diffraction of the HeNe (if we decide to use it). The disappearing of the diffraction grating can be seen on auxiliary reading HeNe beam that is detected and registered on PC.

The typical time dependence of creation and disappearance of grating in our magnetic fluid is presented in Fig. 3. The time dependence of disappearance of grating may be seen in Fig. 4. This dependence has been evaluated and the time constant of the disappearance $\tau = 18{,}2$ s has been obtained. This time constant corresponds with the diffusion coefficient $D = 1.2 \cdot 10^{-11}\, m^2 \cdot s^{-1}$, which is in good agreement with another authors [9], [12].

The quadratic dependence of time constant of disappearance on the grating constant for the first beam (Eq. (9)), has been experimentally verified and is presented in Fig. 5.

4. Some applications

Some technical applications of magnetic fluids were mentioned in the introduction of this paper. The optical grating created by two intersecting coherent laser beams in magnetic fluids could be used as an optical-electronic element, which has some coincident properties as can be seen in Fig. 6a,b.

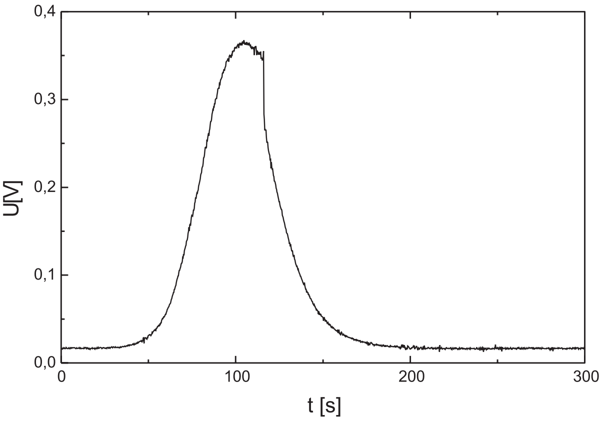

Fig. 3

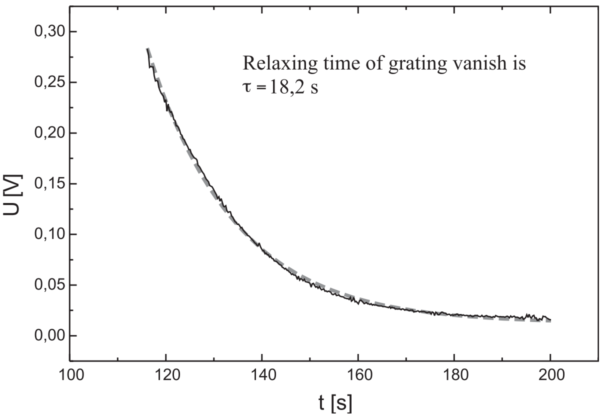

Fig. 4.

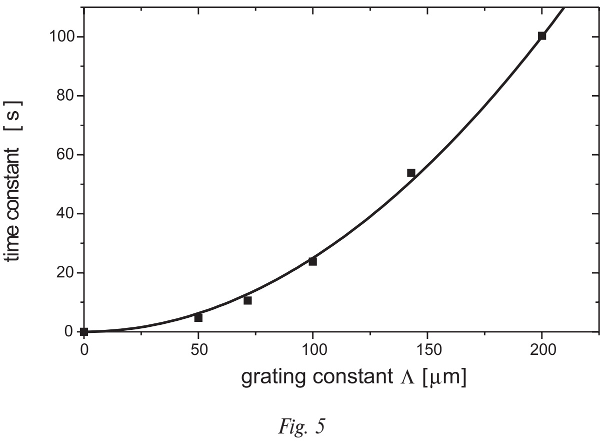

Fig. 5

The signals A, B come on optical grating, realised by magnetic fluid. The coherent signals A or B with wavelength λ are detected on output side separately (Fig. 6a). If both beams appear at the same time, after interference in their intersecting place, the signal C will be also detected on the output.

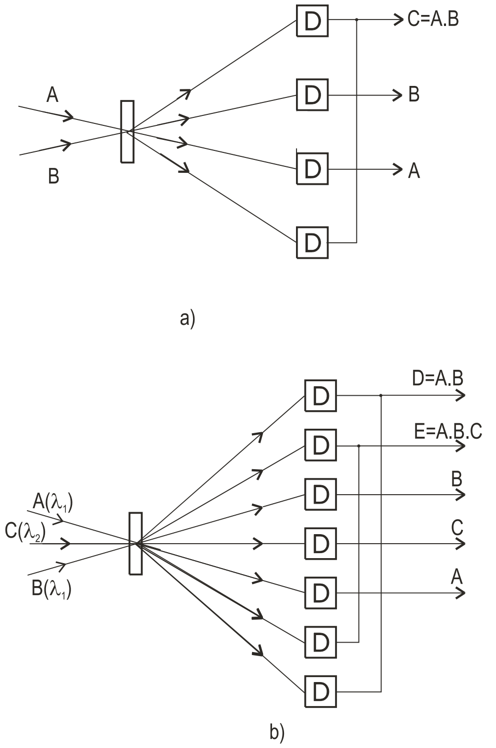

a)

b)

Fig. 6a, b

In Fig. 6b the case of three canal system is shown, in which coherent signals A and B work with wave-length λ_1. The laser beam C works on wave-length λ_2, for this the diffraction angle is different. The laser signals A, B or C can be detected on output side separately. The signal D can be detected if the interfering signals A and B, which the optical grating create, are present in the same time, while signal E is detected if the signals A, B and C are all presented at the same time.

The disadvantage of the presented optical-electronic elements is their slowly response, but in some cases this could turn into advantage, e.g. in cases where the time delay is useful.

5. Conclusion

From the preliminary results it can be seen that using the grating created by interference light field in the sample of the magnetic fluid and with the study of dynamic of its disintegration it is possible to obtain information about diffusion constant (Eq. (6)), the diameter of particles (Eq. (9)), if the viscosity of based fluid is known. Or vice versa the information about properties of the based medium, for example about its viscosity can be obtained, if the effective diameter is known (Eq. (9)). The possibility of other practical applications has been shown as well.

References

[1] ELMORE, W. C.: *Phys. Rev. 54* (1938), 309 and 1092

[2] PAPELL, S. S.: U.*S. Patent, 3 215 572* (1965)

[3] RUUGE, E. K., RUSETSKI, A. N.,: *J. Magn. Magn. Mater. 122* (1993), 335

[4] TSYB, A. F., AMOSOV, I. S., BERKOVSKY, B. M. a kol.: *J. Magn. Magn. Mater. 39* (1983)

[5] SENDERÁKOVÁ, D., CSÓKOVÁ, Z., ŠTRBA, A.: *A Contribution to Laser Induced Thermal Phase Gratings in Wave| and Quantum Aspects of Contemporary Optics,* Jerzy Nowak, Marek Zajac, Editors, Proceedings of SPIE Vol. 3320, (1998), 217

[6] TIMKO, M., KOVÁČ, J., ZENTKO, A., KONERACKÁ, M., KOPČANSKY, P.: *Magnetic fluids the properties and the possibilities of a technical using*, Institute of the exp. phys. SAV, Košice

[7] EICHLER, H. J., GUNTER, P. and POHL, D. W.: *Laser-Induced Dynamic Gratings,* Springer- Verag Berlin, Heidelberg, 1986.

[8] MUSIL, C., ŠTELINA, J., TUREK, I.: *The creating of diffraction grating in magnetic fluid using of Ar laser beam,* The 10. conference of Slovak physicists, l0.-l4.11.1997, Stará Lesná – Vysoké Tatry

[9] TUREK, I., ŠTELINA, J., MUSIL, C., TIMKO, M., KOPČANSKÝ, P., KONERACKÁ, M., TOMČO, L.: *The effect of selfdiffraction in magnetic fluids,* J. Magn. Magn. Mater. 201 (1999), 167

[10] KONPČANSKÝ, P., TOMČO, L., TIMKO, M., OCELÍK, V., KONERACKÁ, M., TUREK, I., ŠTELINA, J. AND MUSIL, C.: *The Dynamics of the Soret Effect in Thin Film of Magnetic Fluid*, Acta Physica Polonica A, No. 5, Vol. 97 (2000), p. 875 – 878

[11] TUREK, I., ŠTELINA, J., MUSIL, C., KOPČANSKÝ, P., TIMKO, M., KONERACKÁ, M., POTOČNÁ, J., JURÍKOVÁ, A., TOMČO, L.: *Self-diffraction of the light in magnetic fluids,* Czechoslovak Journal of Physics, Vol. 52 (2002), Suppl. A, 269

[12] MEZULIS, A., BLUMS, E., BOURDON, A., DEMOUCHY, G.: *Thermodiffusion – induced optical index grating in ferrocolloids: Determination of transport coefficients,* Fourth International PAMIR Conference on MHD at Dawn of Third Millenium, Presquile de Giens, France Sept. 18 – 22, 2000, p. 781

https://doi.org/10.26552/com.C.2003.2.26-28

Sofia Berezina – Oleg Kolosov – Juraj Slabeycius *

INVESTIGATION OF LOCAL MECHANICAL PROPERTIES OF Al-Cu-Li ALLOYS BY ACOUSTIC MICROSCOPE

The reflected scanning acoustic microscope was used for investigation of elastic properties of extruded Al-Cu-Li alloys. The local sound velocity and attenuation were measured by the V(z) curve method. The results show strong anisotropy of material due to extrusion of the sample.

1. Introduction

Modern technologies require materials working under extreme conditions with high reliability. One of the key parameters that have great impact on the life expectation of a material is its microstructure. The microstructure of green specimens can be changed. Extreme loading of material can lead to the various discontinuities, such as cracks, voids, dislocations and delaminations. Extrusion changes the shape of the grains resulting in the anisotropy of the isotropic green specimens. The development and investigation of new materials are not possible without effective method of measurement and testing their physical properties. Moreover, nondestructive testing of materials or device components is an obligatory part of every production process.

Acoustic microscopy represents very useful tool for investigation of materials. It provides a possibility for inspecting the internal structure of opaque specimens as well as quantitative evaluating the elastic properties of materials [1, 2].

We use scanning acoustic microscope (SAM) for investigation of elastic anisotropy of extruded Al-Cu-Li alloys.

2. V(z)-curve method

If the image formation requires the scanning of the object in the focal plane (2D x-y scanning), the quantitative measurement based on the *V*(*z*)-curve uses the scanning of the specimen towards the lens (z-direction) only. The valuable information about the specimen's elastic properties is extracted from the dependence of the output signal on the z-shift. The output signal oscillates periodically with z and the period Δz is characteristic for material [3].

There are two approaches for theoretical explanation of *V*(*z*) curves: wave description, based on the Fourier optics [4] and ray approximation [5]. Due to ray approximation the spherical wave created by the lens can be expanded into a set of particular plane waves incident to the object surface at various angles from 0 to ϑ_A. The ray with direction of the wave vector represents every particular wave (Fig. 1). If the angle of incidence is equal to ϑ_R, the incident wave generates surface Rayleigh wave. The critical angle can be determined from the formula $\vartheta_R = \arcsin(v_k/v_R)$ where v_k is the velocity of bulk wave in the liquid and v_R is the Rayleigh wave velocity.

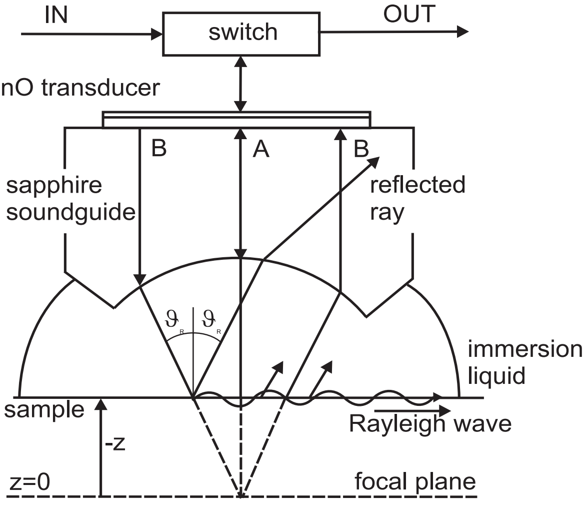

Fig. 1 The creation of output signal by two groups of waves

This surface wave is a leaky wave, it radiates the bulk wave into the immersion liquid at the angle of ϑ_R. The output signal is a result of the interference of the two groups of waves – the waves reflected from the object (ray A) and the waves radiated into immersion liquid by surface wave (ray B). These two rays give the main contribution to the output signal. The phase difference between rays A and B is

$$\Delta\varphi = \frac{2\,k\,z}{\cos\,\vartheta_R} + 2\,k_R\,z\,\mathrm{tg}\,\vartheta_R + \pi, \qquad (1)$$

---

* [1]Sofia Berezina, [2]Oleg Kolosov, [3]Juraj Slabeycius
[1]University of Žilina, Department of Physics, Veľký Diel, 010 26 Žilina, Slovakia
[2]University of Oxford, Department of Materials, Parks Road, OXFORD OX1 3PH, UK
[3]University of Trenčín, Faculty of Industrial Technologies, Department of Physical Engineering of Materials, ul. T. Vansovej 1054/45, 020 32 Púchov, Slovakia, slabeycius@fpt.tnuni.sk

where k_R is the wave number of surface wave and k is the wave number of the bulk wave in the immersion liquid. The phase shift π is connected with phase delay of Rayleigh wave related to the bulk wave. The interference maximum occurs for the phase difference of $2\pi n$ and therefore period of oscillation of $V(z)$ curve will be

$$\Delta z = \frac{\lambda/2}{1 - \cos\vartheta_R} = \frac{v_k/2f_0}{1 - \cos\vartheta_R}\,, \qquad (2)$$

where λ is the wavelength of the bulk wave in liquid and f_0 is the ultrasound frequency. Thus, we can determine the velocity of surface acoustic wave by measuring Δz.

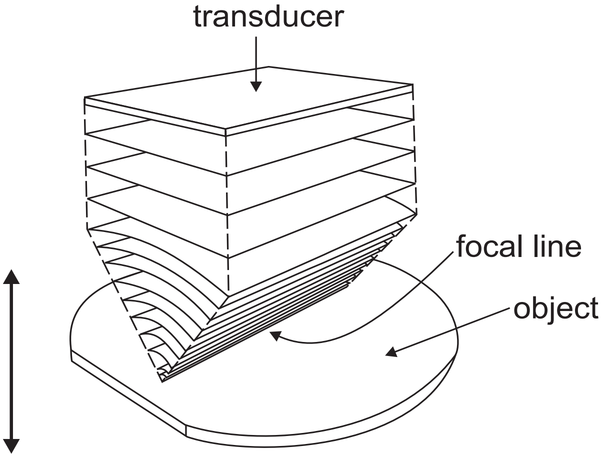

Fig. 2 Cylindrical acoustic lens

For anisotropic material where the SAW velocity depends on the direction of propagation, a cylindrical acoustic lens with line focus (Fig.2) is widely used [6 - 8]. The SAW generated by cylindrical lens has a direction perpendicular to the focal line. The periodicity of V(z) is for this case done by the same formula (2).

3. Samples

Aluminum alloys are materials of great importance in industry. Extrusions of Al-Cu-Li alloys with fiber texture often exhibit significant anisotropy and variation of mechanical properties through the profiles [9-10]. These variations depend on extrusion shape, extrusion procedure parameters and thermo-mechanical treatment parameters [11]. We investigated two alloy samples containing 2.59 Cu, 2.05 Li, 0.11 Zr, 0.04 Mg, 0.02 Si, 0.09 Fe wt. % with half of the dumb-bell profile (Fig. 3). The sample 1 was thermally treated at 530 °C and polished, the sample 2 with mat surface was not treated.

4. Experiment and results

Scanning acoustic microscope with large aperture cylindrical lens ($\vartheta_A = 2 \times 40°$) and operation frequency 250 MHz was used for obtaining the $V(z)$ curves for both samples. The measurements were carried out for the two direction: along the sample side-sill (direction A) and perpendicular to it (direction B).

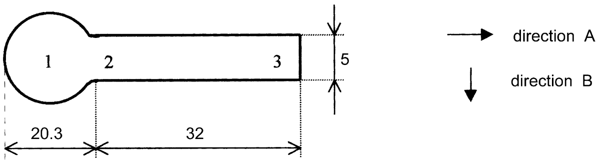

Fig.3 Positions of the measurement points in the cross-section of the AL-Cu-Li sample profile. Dimensions are given in mm.

Typical $V(z)$ curve is presented in Fig. 4, where the horizontal axis corresponds to the shift z and vertical one scales the relative values of the output signal.

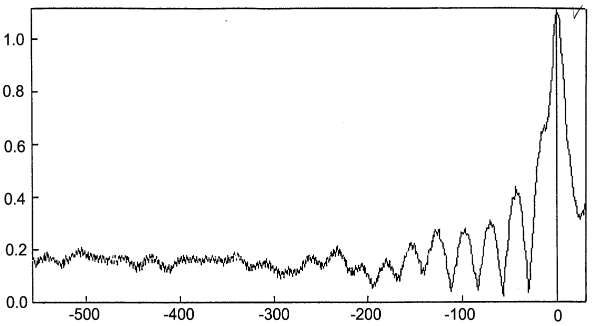

Fig. 4 V(z) - curve for sample 1, point 2, SAW direction B.

The data on SAW velocities measured in the points 1, 2, 3 are summarized in Table 1. As follows from the table, SAW velocity are higher in the sample 1 (with heat treatment and polished surface) for all points of the measurement and for both direction of SAW propagation. Taking into account that the enlargement of SAW velocity after polishing the fine ground surface is usually about 1% [12], one can deduce the reinforcing the alloy under the heating.

The presented results demonstrate also the significant variation and anisotropy of elastic properties across the cross-section of the treated sample. The SAW velocity values in point 3 are higher than the ones in point 1 for both directions of SAW propagation. At the same time the velocity of surface waves propagating perpendicular to the dumb-bell axis is lower than the velocity of SAW in the direction A (along the axis). It can be related with the changes of the material in the measured points. Fig. 5 shows the roll grain texture in the circular part of the sample 1 whereas the flattened grains befit to its rectangle part.

A large variation of SAW attenuation through the cross section was measured. The attenuation at the point 3 is noticeably higher (up to 20 dB) for SAW direction B for both samples. It can be related with the bigger scattering of the sound energy on the closest grain boundaries fallen on the length unit in direction B compared with direction A.

Table 1

Sample	Sample 1 (heating + polishing)				Sample 2			
	SAW-direction A		SAW-direction B		SAW-direction A		SAW-direction B	
Point	*V* M/s	*α* dB/mm	*V* m/s	*α* dB/mm	*V* m/s	*α* dB/mm	*V* m/s	*α* dB/mm
1	3153.7	116	3139.6	96	3074.2	97	3079.4	90
2	3127.4	69	3147.6	66	3093.7	88	3103.5	101
3	3213.7	70	3162.0	89	3094.3	87	3080.1	108

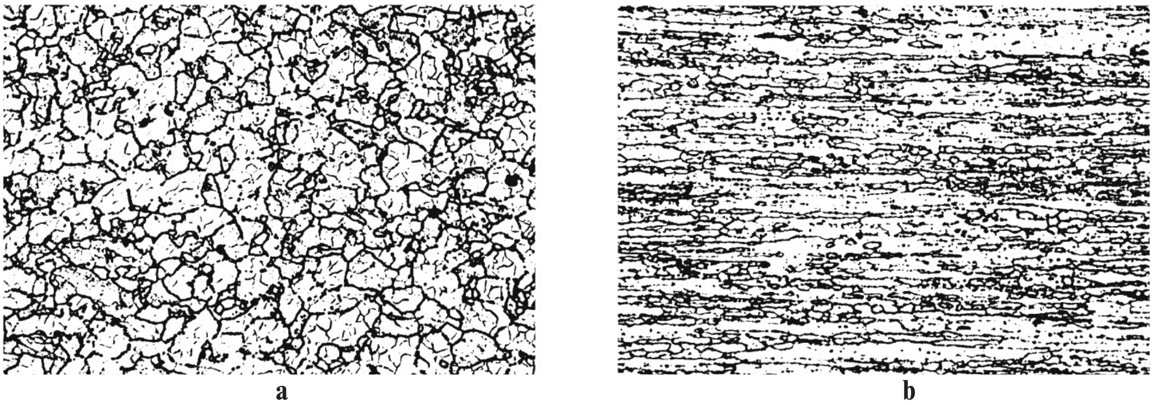

Fig.5 The grain texture in point 1 (a) and in point 3 (b) in the cross section of extruded Al-Cu-Li sample. Magnification 200.

5. Conclusion

The obtained results demonstrate the possibility of acoustic microscopy for reliable detection of the elastic anisotropy of extruded specimens. Both acoustic velocity and attenuation were found different for two main axes of the sample cross section. On the basis of the velocity comparison for samples 1 and 2 one can conclude that the heat treatment leads to the hardening of the alloy.

References

[1] ZININ, P. V.: *Quantitative Acoustic Microscopy of Solids.* Handbook of Elastic Properties of Solids, Liquids, and Gases. Volume I: Dynamic Methods for Measuring the Elastic Properties of Solids. M. Levy, H. Bass, R. Stern and V. Keppens. New York, Academic Press. (2001), pp. 187-226.

[2] KOŠTIAL, P., BEREZINA, S., SLABEYCIUS, J.: *Utilisation of Ultrasonic Waves in the Study of Surfaces and Interfaces*, Univ. of Zilina Edition, Žilina, 1998 (in Slovak)

[3] WEGLEIN R. D., WILSON R. G.: *Characteristics Material Signatures by Acoustic Microscopy*, Electr. Lett., 14, (1978), 352

[4] ATALAR A.: *A Physical Model for Acoustic Signatures,* J. Appl. Phys., 50, (1979), 8237

[5] PARMON W., BERTONI H. L.: *Ray Interpretation of the Material Signature in the Acoustic Microscope,* Electr. Lett., 15, (1979), 684

[6] BEREZINA S. I.: *Application of acoustic microscope for determining the orientation dependences of SAW velocity in crystals.* Proc. of XI Sov. Conf. on acoustoelectronics and quantum acoustics (Dushanbe, May 1981), part 1, p.84-85 (in russian)

[7] KUSHIBIKI, J., OHKUBO, A., CHUBACHI,. N.: A*nisotropy Detection in Sapphire by Acoustic Microscopy using Line-Focus-Beam,* Electton.Lett, 17, (1981), 534

[8] BRIGGS, A., KOLOSOV, O.: *Anisotropic elastic characterization of surfaces from 2 MHz to 20 MHz. Ultrasonics,* 36, (1998), p.317-321.

[9] STARÝ, V., MACEK, K.: *Composition US. Size Distribution of Intermetallic Phases in Al Alloys(Al-Cu-Li-Zr).* Journal of Computer Assisted Microscopy. 9, No. 1, (1998) p. 45.

[10] CIESLAR, M., VOSTRÝ, P., OČENÁŠEK, V., STULIKOVÁ, I.: *Inhomogeneity of Mechanical Properties and Deformation Instabilities in Al-Cu-Li-Mg Alloy*, Material Science and Eng. A234-236 (1997), 790-793.

[11] TARDY F., NORDY, M. H., PARADIS L., BABOUX, J. C.: *Material Surface Characterization by a Rayleigh Velocity Measurement,* Proc. of Ultrasonics World Congress 1995, Berlin 1995, 451.

[12] EYRAUD, V., NADAL, M. N., GONDARD, C.: *Texture measurement of shaped Materials by Impulse Acoustic Microscopy*, Ultrasonic World Congress 99, Book of Abstracts.

https://doi.org/10.26552/com.C.2003.2.29-32

D. Pudiš – J. Kováč jr. – J. Kováč – J. Jakabovič *

SEMICONDUCTOR LASERS BASED ON QUANTUM WELL STRUCTURES

We present electrical and optical properties of the quantum well laser structures based on InAs / $Al_xGa_{1-x}As$ material systems. The experimental results obtained from room- and low temperature electroluminescence measurements of InAs/$Al_{0.40}Ga_{0.60}As$ revealed the excellent emission spectra in the visible range 620-660 nm. The experimentally obtained transitions energies were compared with simple Kronig-Penney simulations. Going to low temperatures the stimulated emission from the cleaved edge was observed, which could be real perspective for laser applications.

1. Introduction to quantum structures

The development of III-V semiconductor growth techniques and their ability for growth of smooth ultra-thin layers on atomic scale have opened a new area in semiconductor research and technology. Quantum well (QW) heterostructures and superlattices with high-quality crystal perfection were fabricated by molecular-beam epitaxy (MBE), or metal-organic vapor phase epitaxy (MOVPE) [1]. These QW structures prepared from various III-V alloy semiconductors have received considerable interest because of their band-energy variability, which allows preparing of optoelectronic devices operated in wide spectral range.

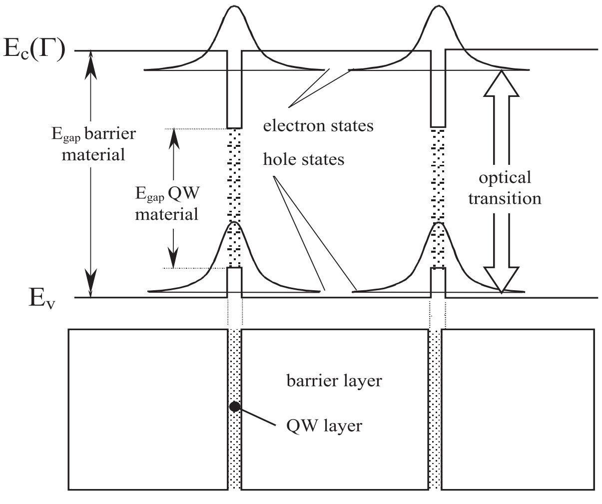

Fig. 1 Schematic of energy band diagram of QW structure – QW and barrier layer in active region. To form the potential quantum well the appropriate semiconductor material should be chosen (E_{gap} (QW) < E_{gap} (barrier)). Electron and hole in QW are then localized above conduction and valence band edge, respectively. The energy of optical transition lies at higher energies than in bulk QW material.

In these structures the energy of optical transition can be adjusted by an appropriate choice of III-V alloy semiconductors as well as by layer thickness in active region (fig. 1) [2, 3].

Considerable attention has been recently devoted to monolayer (ML) and submonolayer QW structures with layer thickness of some atomic layers in active region [4, 5, 6]. In ML QW structures the electron and hole states are energetically localized close to the band edge of barrier layer. To improve emission intensity from active region the multi quantum well (MQW) structures were designed. For our studies the InAs material for QW and $Al_xGa_{1-x}As$ ternary as barrier material has been chosen. The Al mole fraction $x = 0.40$ was used to achieve the emission at higher energy in comparison with the laser structure $x = 0.34$ published in [7].

Our experimental investigations focus on characterization of optical and electrical properties at room and low temperatures. Electrical properties of the structure are investigated by the measuring of conventional current-voltage characteristics. Optical properties are characterized by photoluminescence (*PL*) and electroluminescence (*EL*) measurements. To get information on the layer perfection high-resolution transmission electron microscopy (HRTEM) investigations have been performed.

2. Theoretical modeling of energy states

For design of devices and comparison of experimental results with theory it is important to know the location of the lowest energy state of electrons (*e*) in conduction band (*CB*), heavy holes (*hh*) and light holes (*lh*) in valence band (*VB*) (Fig. 2).

These states can be determined by solving Schrödinger's equation in each layer and by matching the solutions across the boundaries. As an idealized approximation for calculating the lowest *e*, *hh* and *lh* energy bands is the Kronig-Penney analysis [8]. These

---

* **[1]D. Pudiš, J. [2]Kováč jr., [3]J. Kováč, [3]J. Jakabovič**
[1]University of Žilina, Department of Physics, Veľký diel, SK 010 26 Žilina, Slovakia
[2]International Laser Center, Ilkovičova 3, SK 812 19 Bratislava, Slovakia
[3]Slovak Technical University, Department of Microelectronics, Ilkovičova 3, SK 812 19 Bratislava, Slovakia

calculations are simplified, but they provide a useful guide for choosing layer thickness corresponding to the desired *e*, *hh*, *lh* energies. The $n = 1$ energies are calculated as a function of well size for InAs and $Al_xGa_{1-x}As$ ternary barriers from the following expressions

$$\tan\left[\frac{a}{2\hbar}(2m_a E_{min})^{1/2}\right] - \left[\frac{m_a}{m_b}\left[\frac{V}{E_{min}} - 1\right]\right]^{1/2}$$

$$\tan h\left[\frac{b}{2\hbar}[2m_b(V - E_{min})]^{1/2}\right] = 0 \qquad (1)$$

$$\tan\left[\frac{a}{2\hbar}(2m_a E_{max})^{1/2}\right] - \left[\frac{m_a}{m_b}\left[\frac{V}{E_{max}} - 1\right]\right]^{1/2}$$

$$\cot h\left[\frac{b}{2\hbar}[2m_b(V - E_{max})]^{1/2}\right] = 0 \qquad (2)$$

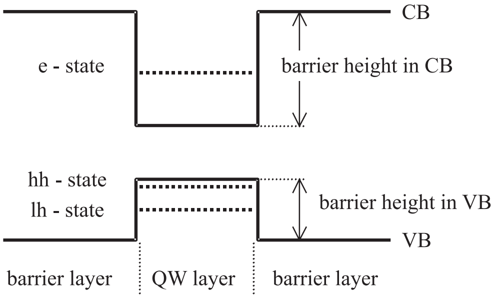

Fig. 2 Quantum confined e, hh and lh energy states. Square potential well for electrons and holes is formed by material parameters (E_g, VBO) and thickness of QW layer.

where *a* and *b* are well and barrier thickness and m_a and m_b the particle effective masses inside QW and barrier, respectively. The energy *E* of localized particle states (*e*, *hh*, *lh*) is calculated from the minima of conduction and valence band, respectively. The barrier height *V* of conduction and valence band is determined from the valence-band offset of well and barrier materials [9]. These expressions are generally valid as well for QW structures as for superlattices, where in superlattice structures with thin barrier layer the solution of particle energy splits into minibands represented by an energy range ($E_{max} - E_{min}$) [3]. The energy states of higher order ($n > 1$) in CB and VB can be determined similarly according to [8].

3. Laser preparation

The sample growth was carried out by low-pressure MOVPE in a commercial AIXTRON AIX-200 reactor equipped with a rotating substrate holder and standard precursors TMAl, TMGa, TMIn, DetZn, AsH_3 and Si_2H_6 with vapor pressure values $p(tot) = 50$ mbar and $f(tot) = 7$ slm on (001) oriented n-type GaAs substrates. The MOVPE experiments were carried out at growth temperatures 700 °C [1]. The layer arrangement (Fig. 3a) consists of a 450 nm GaAs buffer layer followed by a 1300 nm n-doped $Al_{0.55}Ga_{0.55}As$ confinement layer, the active region and 550 nm p-doped $Al_{0.55}Ga_{0.55}As$. The structures were covered by 10 nm GaAs layer. The active region contains 10 spatially well-separated InAs monolayers buried in thick (20 nm) $Al_{0.40}Ga_{0.60}As$ barriers. The contact metalization was performed by evaporating Au on top GaAs layer and AuGeNi on the bottom of n+ GaAs substrate.

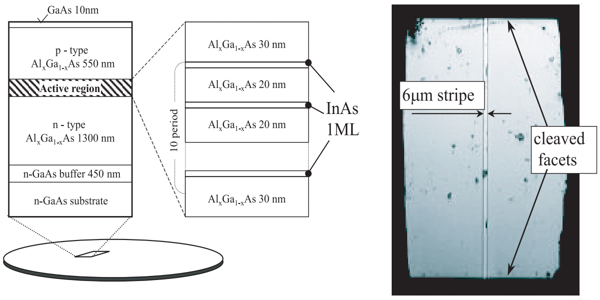

a) b)

Fig. 3 a) The layer arrangement of QW structure with detail of $InAs/Al_xGa_{1-x}As$ active region. b) CCD surface image of stripe laser device. The spontaneous emitting light arises in InAs QW and is amplified between cleaved planes along the Au stripe contact.

For the emission study the gain guided metal stripe lasers were fabricated. The stripes width of 6 μm in SiO_2 mask and AuBe/Ti/Au p-contact layer were prepared. The laser device fabrication was completed by thinning the wafer to 150 μm thickness and evaporation of bottom AuGe/Au n-contact. The samples were cleaved perpendicular to metal stripes (Fig. 3b). From the Kronig-Penney model the energy of optical transition was calculated to be 1.973 eV at $T = 0K$. As Kronig-Penney inputs the $InAs/Al_{0.40}Ga_{0.60}As$ material and layer thickness parameters according to the schematic in fig. 3a were used.

4. Experimental results

The electrical and optical properties of prepared laser device based on MQW structure were investigated. Electrical properties were examined by current-voltage measurements at forward bias. From room- and low-temperature electroluminescence (EL) measurements the optical properties were revealed. The low-temperature EL spectra were measured in He-close cycle cryostat. For recording the EL spectra monochromator of type SPM2 and Si-photodetector were employed. The EL intensity vs. driving current was measured by conventional pulse technique. Laser mode emission spectra were recorded using high-resolution double grating monochromator.

Electrical properties

The current-voltage measurement at forward bias shows the p-n junction opening in the range of 1 V in correspondence with diffusion potential. The weak edge emission from the active region was observed at current about 1 mA. The current flow increasing through the MQW region has influence on emission intensity.

The current flow is limited in the range of 1.5 V – 2.5 V due to low conductivity of confinement layers and intrinsic MQW active region as shown in current-voltage dependence (Fig. 4).

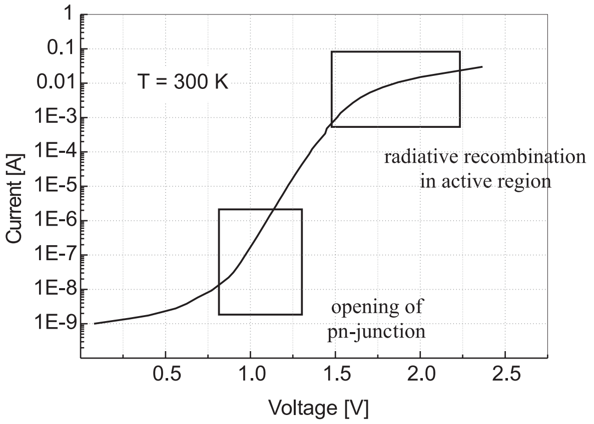

Fig. 4 Current-voltage dependence of laser device. Room temperature spontaneous emission starts at driving current app. 1 mA.

Optical properties

The optical properties on stripe laser structures were investigated by measuring the room- and low temperatures EL spectra from the cleaved edge of laser structure.

Room temperature EL spectrum revealed only the weak spontaneous emission from the cleaved edge of the laser structure with maximum intensity at 1.891 eV (655.7 nm) (fig. 5a). When going to low temperatures a considerable increase of the EL intensity (Fig. 5b) due to the strong localization of bound states in QW was observed and the energy of main maxima shows the blue shift in correspondence with $E_g(T)$ relation of $Al_xGa_{1-x}As$ barrier. At $T =$ $= 20$ K the maximum intensity lies at the energy 1.995 eV (621.6 nm).

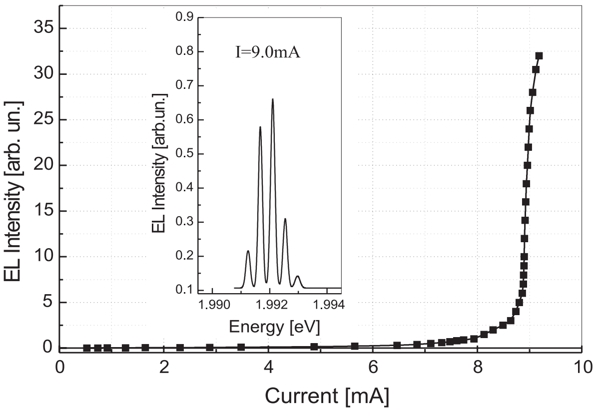

Fig. 6: The EL intensity vs. driving current and laser mode spectra (insert figure) of laser device based on InAs/$Al_{0.40}Ga_{0.60}As$ QW structure in active region.

From comparison of the experimental results and theoretical predictions (1.973 eV – $T = 0$ K) from point of view of the main peak energy position in EL spectra, the small discrepancy (app. 20 meV) was found. It could be caused probably by replacing the real structure by periodic square potential in Kronig-Penney model as well as exciton binding energy of localized e-hh pairs (excitons) in QW [7].

To achieve the higher emission energy the $Al_{0.40}Ga_{0.60}As$ was used in active region. Thus, the emission energy increased of

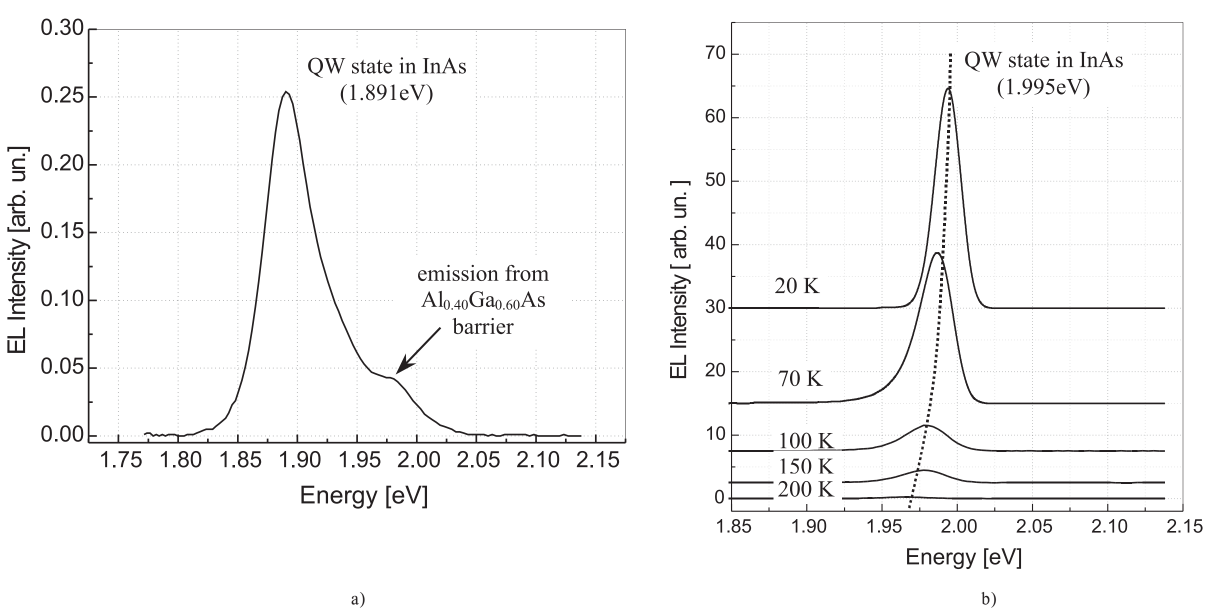

a) b)

Fig. 5 The EL spectra recorded from the cleaved edge of laser devices at a) room temperature and b) in temperature range of 20 - 200K. Dashed line shows the blue shift of maxima.

app. 80 meV in comparison with the structures employing the $Al_{0.33}Ga_{0.67}As$ material in active region [7, 9].

For the temperatures ranging from 20 K to 100 K the prepared stripe laser structure with InAs monolayers shows stimulated emission across their cleavage planes. The EL intensity vs. driving current characteristic of this structure shows the typical increase of emission intensity in the region of threshold current density (Fig. 6). Insert figure shows a laser mode spectrum measured at $T = 20$ K and driving current 9.0 mA. From the recorded dependence the extremely low threshold current and current density was estimated to be $I_{th} = 8.9$ mA.

5. Conclusion

To sum it up, we studied the optical and electrical properties of MQW structures based on $InAs/Al_xGa_{1-x}As$ materials grown by MOVPE as a real perspective structure for applications in laser devices. Optical properties were investigated by current and temperature dependencies of EL spectra taken from the cleavage plane of stripe laser arrangements.

Room temperature EL spectrum shows only weak edge emission at energy 1.891 eV. At low temperatures (20 K – 100 K) the InAs monolayer luminescence becomes very sharp and intense; its peak energy reflects nearly the $E_g(T)$-relation of the $Al_xGa_{1-x}As$ band gap [10].

In the low temperature range stimulated emission for investigated structures occurs at photon energies of about 1.995 eV (621.6 nm) for $T = 20$ K. At higher temperatures (above 100K) the stimulated emission disappears due to the thermal dissociation of InAs monolayer-bound excitons [2].

The material and layer parameters for growth processes could be calculated by simple Kronig-Penney model.

In our opinion the material system under investigation might be interesting for potential optoelectronic device applications. These excellent emission properties observed in MQW structures with the material basis of $InAs/Al_xGa_{1-x}As$ could be successfully employed in possible applications in the light emitting and laser devices operated in red and orange-red range of spectra.

Acknowledgement
This work has been supported by Slovak Grant Agency contract No.7600/20, International Laser Center Bratislava and bilateral WTZ project No. SVK01/001 (21/2001).

References

[1] GOTTSCHALCH, V., SCHWABE, R., WAGNER, G., KRIEGEL, S., FRANZHELD, R., PIETZONKA, I., PIETAG, F., KOVÁČ, J.: *Proc. of 7th EW MOVPE,* June 8-11, Berlin, 1997, E4

[2] TRAN, C. A., ARES, R., KARASYUK, V. A., WATKINS, S. P., LETOURNEAU, G., LEONELLI, R.: *Phys. Rev. B 57*, 1997, pp. 4633-4638

[3] MUKHERJI, D., NAG, R.B.: P*hys. Rev. B 12*, 1975, pp. 4338-4345

[4] IOTTI, R. C., ANDREANI, L. C., VENTRA, M. D.: *Phys. Rev. B 57*, 1998, pp. 15072-15075

[5] KOVÁČ, J., KUNA, L., GOTTSCHALCH, V., BENNDORF, G., GERHARDT, M., PUDIŠ, D., JAKABOVIČ, J., ŠKRINIAROVÁ, J.: *Proc. of 8th EW MOVPE*, June 8-11, Berlin, 1999, F1M4

[6] BITZ, A. J.: *Ph.D. thesis*, 1997

[7] PUDIŠ, D., KOVÁČ, J., KOVÁČ, J.,jr., JAKABOVIČ, J., GOTTSCHALCH, V., BENNDORF, G., RHEINLÄNDER, B., SCHWABE, R.: *Advances in Electrical and Electronic Engineering 1*, 2002, pp.33-37

[8] CHO, H. S., PRUCNAL, P. R.: *Phys. Rev. B 36*, 1987, pp. 3237-3242

[9] CATALANO, I. M., CINGOLANI, A., LEPORE, M., CINGOLANI, R., PLOOG, K.: *Phys. Rev. B 41*, 1990, pp. 12937-12940

[10] BLAKEMORE, J. S.: *J. Appl. Phys. 74*, 1993, pp. R123-R181

https://doi.org/10.26552/com.C.2003.2.33-36

Ivo Čáp – Klára Čápová – Dagmar Faktorová *

INTERACTION OF ELECTROMAGNETIC AND ACOUSTIC WAVES IN CONDUCTORS AND ITS UTILIZATION

The paper deals with the interaction of electromagnetic and acoustic processes in a conducting medium in presence of an external magnetic field. The electromagnetic excitation of acoustic wave similarly as acoustic excitation of electromagnetic wave is described. The practical utilization consisting in contactless acoustic wave generation and detection is demonstrated.

1. Introduction

The elastic and conducting medium consists of ionic lattice and gas of electrons. The external electromagnetic field acts on the particles and excites their motion. Under usual conditions the direct electromagnetic force affecting the ionic structure is screened by the electron collisions drag force, so that no mechanical excitation is observed. The penetrating electromagnetic wave is strongly damped in a thin surface skin layer. The screening effect can be disturbed by an external constant magnetic field. In such a case the mechanical excitation of the ionic lattice can propagate through the sample as an elastic wave, e.g. [1]. On the other hand the ionic movement generates the secondary electromagnetic wave which accompanies the elastic wave and represents the elastic mode of the electromagnetic wave, e.g. [2]. It propagates with the acoustic wave velocity and weak attenuation and can be detected at the opposite side of the conducting sample. There are many possibilities of the utilization of the effect. One of them consists in contactless ultrasonic defectoscopy of metal samples, another in the electromagnetic detection of mechanical vibrations in bodies, etc. The effect can be utilized in a wide range of frequencies and temperatures.

2. Theoretical description of the effect

Interaction of the mechanical motion of the structure and electromagnetic field in the medium can be described by means of wave equations of the electromagnetic wave and the elastic wave

$$\Delta \mathbf{E} - \epsilon\,\mu\,\frac{\partial^2 E}{\partial t^2} = \mu\,\frac{\partial J}{\partial t} \quad \text{and} \tag{1}$$

$$c_l\,\text{grad div}\,\xi - c_t\,\text{rot rot}\,\xi - \rho\,\frac{\partial^2 \xi}{\partial t^2} = \mathbf{f}, \tag{2}$$

where $\mathbf{E} \equiv \mathbf{E}(\mathbf{r}, t)$ is the electric intensity, $\xi \equiv \xi(\mathbf{r}, t)$ is the ionic displacement from the equilibrium state, ϵ and μ are permitivity and permeability of the medium, c_l and c_t are longitudinal and shear elastic constants, ρ is the density and $\mathbf{f}$ is the density of non-elastic forces acting on ions. $\mathbf{J} \equiv \mathbf{J}(\mathbf{r}, t)$ is the electric current density, which consists of both ionic and electronic parts

$$\mathbf{J}(\mathbf{r}, t) = \mathbf{J}_i(\mathbf{r}, t) + \mathbf{J}_e(\mathbf{r}, t)\,. \tag{3}$$

Ionic current is in connection with ionic displacement velocity

$$\mathbf{J}_i(\mathbf{r}, t) = n\,e\,\frac{\partial \xi}{\partial t}\,. \tag{4}$$

Electronic current density is given by

$$\mathbf{J}_e(\mathbf{r}, t) = \overset{\Rightarrow}{\sigma} \cdot \left(\mathbf{E} - \frac{n\,e}{\sigma_0}\,\frac{\partial \xi}{\partial t} + \frac{2\,E_F}{3\,e}\,\text{grad div}\,\xi\right), \tag{5}$$

where $\overset{\Rightarrow}{\sigma}$ is the tensor of the magneto-conductivity, σ_0 is the DC conductivity, n and e are the electron density and the elementary charge and E_F is the Fermi energy of the electron gas. The second term in the parentheses corresponds to the electron current caused by the motion of the ionic background and the third to the diffusion of the electrons.

The resulting force density acting on the ionic lattice can be expressed as

$$\mathbf{f}(\mathbf{r}, t) = f_{EM}(\mathbf{r}, t) + \mathbf{f}_e(\mathbf{r}, t), \tag{6}$$

where

$$f_{EM}(\mathbf{r}, t) = ne\left(\mathbf{E} + \frac{\partial \xi}{\partial t} \times \mathbf{B}\right) \tag{7}$$

is electromagnetic Lorentz force density from the resulting electromagnetic field in the medium and

$$\mathbf{f}_e(\mathbf{r}, t) = -\frac{nm}{\tau}\left(\frac{1}{n\,e}\,\mathbf{J}_e + \frac{\partial \xi}{\partial t}\right) \tag{8}$$

is the electron drag force resulting from the electron-ion collisions. In two last terms there is $\mathbf{B}$ the magnetic flux density, m is the mass of electron and τ is the collision mean free time.

The dynamic process can be significantly influenced by means of external constant magnetic field. In the case of linear processes

---

* [1]**prof. Ing. Ivo Čáp, CSc.**, [2]**prof. Ing. Klára Čápová, PhD.**, [2]**Ing. Dagmar Faktorová**
[1]University of Žilina, Faculty of Science, Hurbanova 15, SK-010 26 Žilina, Slovakia, E-mail: icap@fpv.utc.sk
[2]University of Žilina, Faculty of Electrical Engineering, Veľký diel, SK-010 26 Žilina, Slovakia, E-mail: capova@fel.utc.sk

the magnetic flux density $\boldsymbol{B}$ will be substituted by the constant value $\boldsymbol{B}_c$ and the time-dependent component will be neglected. In the presence of the external magnetic filed the conductivity tensor represents the electric anisotropy of the medium depending on the magnetic field orientation. For example, if the magnetic field vector $\boldsymbol{B}_c$ is parallel to the z direction, the magneto-conductivity tensor has the form

$$\overset{\Rightarrow}{\sigma} = \sigma_0 \begin{pmatrix} 1 & 0 & 0 \\ 0 & 1 & -\omega_c \tau \\ 0 & \omega_c \tau & 1 \end{pmatrix}, \tag{9}$$

where $\omega_c = e\, B_c\, /\, m$ is the cyclotron angular frequency.

The products of the conductivity tensor $\overset{\Rightarrow}{\sigma}$ and the terms obtaining ξ in (5) together with vector product in (7) represent the mathematical description of the mechanism of the interaction of electromagnetic and mechanic processes in the medium. In such way the time-dependent electromagnetic excitation generates acoustic process in the ionic structure and on the other hand the mechanical motion of the ionic structure leads to the accompanying electromagnetic field generation.

3. Waves in a conducting medium

Let us suppose the semi-infinite sample with the surface normal to the *z*-direction and all wave processes as plane waves propagating in *z*-direction. The set of equations (1) and (2) together with (3) to (8) can be solved under corresponding boundary conditions by means of Laplace transformation, e.g. [2], [3].

In many practical applications we utilise the mechanism of electromagnetic generation of the acoustic wave. In such case we suppose the plane electromagnetic wave polarized in *x*-direction and incident perpendicularly to the sample surface. In the case of $\boldsymbol{B}_c$ parallel to the *z*-direction the shear acoustic wave with *y*-polarization is excited. If the $\boldsymbol{B}_c$ has y-direction, the longitudinally polarized acoustic wave is excited. The time and space dependence can be expressed by

$$\xi(z,\, t) = i\, \frac{2\, H_0\, B_c}{\omega\, \rho\, s}\, e^{-i\, \frac{\omega}{s}\, z}\, e^{i\, \omega\, t},$$

where H_0 is the magnetic intensity of the incident electromagnetic wave at the surface, ω is the angular frequency and s is the velocity of the acoustic wave of the corresponding polarization. The shear component of the accompanying electromagnetic wave perpendicular to the propagation direction z can be expressed by

$$E(z,\, t) = i\, \omega\, B_c\, \xi(z,\, t) = i\, \omega\, B_c\, \xi_0\, e^{-i\, \frac{\omega}{s}\, z}\, e^{i\, \omega\, t},$$

where ξ_0 is the acoustic wave amplitude at the surface of the sample.

The electromagnetic wave accompanying the electromagnetically excited acoustic wave is given by

$$E(z,\, t) = \frac{2\, H_0\, B_c^2}{\rho\, s}\; e^{-i\, \frac{\omega}{s}\, z}\, e^{i\, \omega\, t}.$$

In the case of planparallel sample the electromagnetic wave is radiated from the sample and it can be detected by a proper detecting coil.

These results are exactly valid for non-magnetic materials. In the case of ferromagnetic materials these processes are influenced by magnetisation and magnetostriction.

4. Electromagnetic – acoustic transducer

The described effect is used in many practical applications. One of them consists in one-probe electromagnetic generation and detection of ultrasound. The arrangement of the probe called electromagnetic-acoustic transducer (EMAT), e.g. [4], is in Fig. 1.

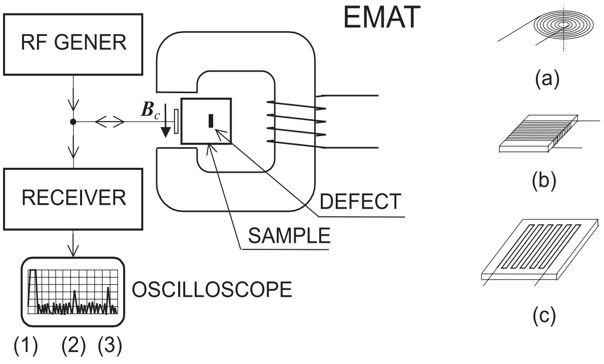

Fig. 1. Arrangement of EMAT and the shape of generating/detecting coils

The EMAT is mostly used for the ultrasonic defectoscopy. RF pulse generates the starting ultrasonic pulse (1). It propagates across the sample and reflects from the backside of the sample, see pulse (3) or from the defects of the sample (2). All pulses are detected, processed by a receiver and visualised by means of an oscilloscope. Position of the defect inside the sample is measured by means of time-delay of the reflected pulse. The conducting sample is placed in the magnetic field of a permanent magnet or an electromagnet. The sample can be placed into the magnetic field so that the magnetic flux density is normal or parallel to the generating-detecting surface of the sample. It determines the slower shear or the faster longitudinal acoustic wave generation.

Both acoustic and accompanying electromagnetic waves were generated by proper coils, Fig. 1 (a) to (c), supplied by the RF signal generator. The coil design determines the acoustic beam profile. The most complex beam structure but the best efficiency represents the flat spiral coil, Fig. 1 (a) and Fig. 2. In the case of a constant magnetic field parallel to the surface, Fig. 2 (a) the generated beam consists of two sub-beams with opposite longitudinal polarization. If $\boldsymbol{B}_c$ is normal to the surface, the generated beam has a shear radial polarization with zero value along the axis of the acoustic beam. This property can be utilised in special applications of EMAT.

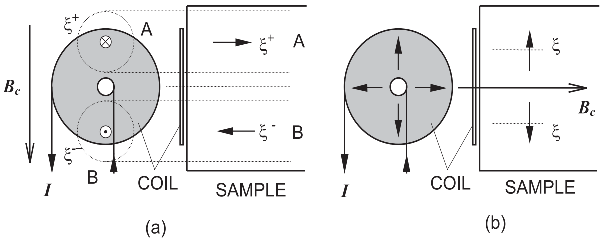

Fig. 2. Polarization of the acoustic wave generated by the flat spiral coil

Another typical shape of the coil is in Fig. 3. The generating/detecting coil is made from the thin wire wound in one layer around the flat dielectric strip. The RF magnetic fields of both layers of the winding with opposite directions of the current and with the phase shift $k\ d$ mutually interfere. The resulting RF magnetic field at the surface of the conducting sample is reduced by $k\ d = \omega\ d\ /\ c$ in comparison with the one-layer coil, e.g. the mentioned spiral coil. The advantage of the rectangular coil is the generation of very homogeneous acoustic beam similar to the plane wave with a better defined wave polarization in the whole sample. The sensitivity is lower than in the case of the spiral coil. Due to the reduction factor kd this generating/detecting coil can be used for higher frequencies applications. The system was tested in the frequency range from 10 to 25 MHz.

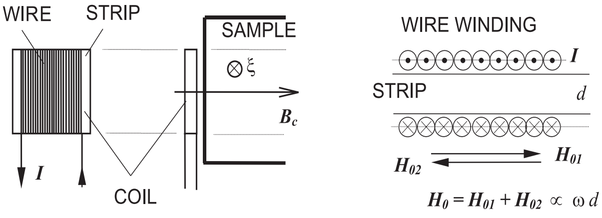

Fig. 3. Rectangular coil

The system of a flat wire coil allows to make generating/detecting coils for the special acoustic waves, as deflected waves, surface waves, focused waves, etc. Fig. 4. The coil in Fig. 4 (a) is able to generate or to detect the acoustic wave deflected from the direction normal to the surface by angle θ according to the ratio of the acoustic wave-length and the period x of the coil structure. The surface acoustic wave is generated under condition of $x = \lambda$. The structure in Fig. 4 (b) generates or detects the focused cylindrical wave. Such a system is very sensitive for the detection of material defects in the corresponding depth. The similar coil can be made as a circular one and then it serves as a planar acoustic lens used in the acoustic microscopy. Special coils can be made by means of planar technology in one-layer or as wire-coils. Because of the exact phase conditions the mentioned coils are designed for concrete frequency. We investigated the metal samples by means of surface acoustic waves at the frequency range 9.8 and 15 MHz. The focused cylindrical system with the tunable focus-length in the range from 5 to 8 mm was used for the one-dimensional scanning system at the mean frequency of 10 MHz. The reached resolution was about 0.5 mm.

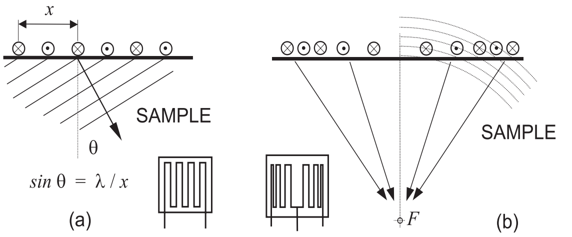

Fig. 4. Special generating/detecting coils

The experimental arrangement of the EMAT had the typical values of characteristic parameters: the RF frequency from 1 to 25 MHz, the generating pulse length of 2 to 5 μs, the repetition rate of 1 kHz, the electric current pulse amplitude of about 10 A. Because of the typical coil resistance of about 5 Ω it represents the pulse power of about 500 W. The received signal emitted from the sample was detected with the same coil and it was amplified by the wide band amplifier with the amplification of 60 dB.

The signal efficiency increases with decrease of the frequency mainly due to the decrease of the elastic wave attenuation, but the resolution increases with the increase of the frequency because of decrease of the acoustic wavelength.

5. Conclusions

The system of EMAT is suitable for investigation of electromagnetic and electrodynamic properties of different conducting structures. The obtained results were utilized in the construction of the EMAT, which enables to investigate defects of conducting samples. The defectoscopy using the EMAT makes possible to investigate the structure of the sample without any acoustic coupling, which is advantageous for the scanning method of the sample structure visualization. The coils made on the different substrates are useable in a wide temperature range as well. Contactless defectoscopy is proper for the investigation of different bodies in motion, e.g. rails or railway wheels. Other applications are connected with special shapes of acoustic beam generated by special generating coils.

References

[1] ARONOV, I. E., FALKO, V. L.: *Electromagnetic Generation of Sound in Metals in a Magnetic Field.* Physics Reports 221 (1992), No. 2-3, pp. 81 - 166.

[2] ČÁPOVÁ, K., ČÁP, I.: *Acoustically excited EM wave in metal,* in: Studies in Applied Electromagnetics and Mechanics, vol. 13, V. Kose and J. Sievert, eds. IOS Press, Amsterdam, 1998, pp. 811-814.

[3] ČÁPOVÁ, K., ČÁP, I.: *Material anisotropy investigation using anomalous EM generation of acoustic wave,* in: Studies in Applied Electromagnetics and Mechanics, vol. 14, R. Albanese at all, eds. IOS Press, Amsterdam, 1998, pp. 74-81.

[4] OGI, H.: *Field dependence of coupling efficiency between electromagnetic field and ultrasonic bulk waves.* J. Appl. Phys. 82, No 8 (1997), 3940-3949.

https://doi.org/10.26552/com.C.2003.2.37-40

KOMUNIKÁCIE
COMMUNICATIONS

P. Šutta – Q. Jackuliak *

X- RAY DIFFRACTION LINE PROFILE ANALYSIS OF STRONGLY TEXTURED THIN FILMS OF ZnO

ZnO thin films have been deposited on SiO_2-Si and Al-SiO_2-Si substrates by reactive sputtering. X-ray diffractometry was used to determine microstructural disorder parameters in ZnO thin films with strong preferred c-axis orientation. The influence of Al and Al_2O_3 buffer layer on preferred c-axis orientation and microstrain of crystallites was also studied. The microstrains and domain size showed only a small dependence on the preference of a buffer layer, but they depend on the thickness of ZnO thin film. The stress gradient along the c-axis was observed in all of studied samples.

1. Introduction

Thin films of metallic conductors, semiconductors and insulators are the basic materials for modern electronic devices. For optimal device performance, these films should possess specific mechanical, electrical, magnetic or optical properties which are strongly influenced by the microstructural qualities of the films such as crystalline or amorphous state, crystallographic orientation, crystallite size, strain and stresses. Therefore, microstructural characterization of thin films is very important for the design and improvement of electronic devices [1].

Due to their small dimensions perpendicular to the surface, the microstructure of thin films cannot be easily characterized by methods developed for the bulk materials. Therefore, various methods of surface physics are frequently applied to thin films. Among the analytical methods especially suitable for thin films, X-ray diffraction plays an important role since it is nondestructive, noncontact and highly quantitative.

However, due to the thinness of the film the diffracting volume is normally very small resulting in weak diffracted intensities. On the other hand, due to preferred orientation of crystallites in a certain direction, some diffraction lines can reach very strong intensities so that in such case there is no problem to apply line profile analysis to obtain the basic structural characteristics of thin films.

In line profile analysis mainly broadening and shape of diffraction line are investigated. Broadening of X-ray diffraction line profile is mainly caused by nonideal optics of the instrument, wavelength dispersion and structural imperfections of the specimen. The structural line broadening is often subdivided into size broadening and strain broadening. Size broadening is caused by the finite size of domains diffracting essentially incoherently with respect to one another. On the other hand, strain broadening is caused by varying displacements of the atoms with respect to their reference-lattice positions [2].

Line broadening is frequently characterized by means of one or two breadth measures (FWHM – full width at half maximum and $\beta = Area/I_0$ – integral breadth) and separation of size and strain contributions have been performed on this basis [3, 4]. More detailed analysis is possible by taking into account the complete shape of a line profile by expressing it in terms of Fourier coefficients. Both breadth and Fourier methods gain in reliability when more than one order of reflection is used for a given set of lattice planes [5].

2. Experimental procedure

In our work, ceramic and metallic thin films deposited on single-crystalline silicon wafers by means of diode sputtering were investigated. In special cases Al, SiO_2 and $A1_20_3$ buffer layers were also applied. A planar r.f. sputtering system Perkin Elmer 2400/8L was used. The sputtering chamber was always pumped down to $2 \cdot 10^{-5}$ Pa before admission of working gas (Ar or Ar/O_2 gas mixture 99,999 % in purity). Throughout the sputtering of Al, ZnO and Al_2O_3 targets (each 203 mm in diameter and 99.95 % in purity) a gas pressure of 1.3 Pa was kept constant [6, 7]. The temperature of substrate was mostly kept at room temperature. In special cases the temperature of substrate was kept at 300 °C or at 600 °C. The effects of different r.f. powers, different substrates and different film thicknesses were investigated. Furthermore, different ratios of Ar/O_2 gas mixture in case of ZnO films as well as the cyclic sputtering and ion etching of films were applied [8, 9]. The general characterisation of sputtered films is listed in Table I.

X-ray diffraction line profile analysis was used to determine microstructural properties of investigated films. First, preliminary diffraction patterns were recorded on the film. After that, the X-ray diffraction data were collected by using an automatic X-ray powder diffractometer URD-6 with a Bragg-Brentano goniometer. A copper X-ray tube (λ = 0,154178 nm) was used. Ceramic $A1_2O_3$ from NIST was used as an instrumental standard. The intensities of

---

* [1]P. Šutta, [2]Q. Jackuliak
[1]Department of Physics, Faculty of Logistics, Military Academy 031 11 Liptovský Mikulaš
[2]Department of Technical Physics, Faculty of Electrical Engineering, University of Žilina, 01026 Žilina

Characterisation of investigated thin films

Table 1

Sample (thin film)	Special condition	Substrate configuration	R. F. Power [W]	Thickness [nm]	Substrate temperature [°C]
ZnO 1	Ar+O_2 (25/75)	Al/SiO_2/Si	500	1000	room
ZnO 2	Ar+O_2 (25/75)	SiO_2/Si	500	1000	room
ZnO 3	Ar+O_2 (60/40)	Al/SiO_2/Si	500	1000	room
ZnO 4	Ar+O_2 (60/40)	SiO_2/Si	500	1000	room
ZnO 5	Ar+O_2 (25/75)	Al/SiO_2/Si	500	2500	300
ZnO 6	Ar+O_2 (25/75)	Al_2O_3/Al/SiO_2/Si	500	2500	300
ZnxOy 1	Multilayers	Al_2O_3/SiO_2/Si	500	250	room
ZnxOy 2	Multilayers	Al_2O_3/SiO_2/Si	500	250	300
ZnxOy 3	Multilayers	Al_2O_3/SiO_2/Si	500	250	600

diffraction lines were collected with a constant step of 0.02 deg of 2-theta and with a constant counting time of 20 seconds at each step. In order to appreciate degree of preferred orientation, the omega-scans of the most intensive diffraction lines for each material were also recorded.

From several available methods appropriate for the line profile analysis a single-line method based on a Voigt function [3] which is more versatile and powerful from the practical point of view was used to determine size-strain parameters (microstrains and crystallite sizes) of investigated thin films [4]. Because no monochromator was used, the $K_{\alpha 2}$ line had to be removed by a graphic method [10, 11].

3. Results and discussion

Because Zinc Oxide has a hexagonal close-packed wurtzite structure, polycrystalline thin films prepared by different techniques have usually preferential orientation of their grains in the [001] direction perpendicular to the substrate, strongly depending on the deposition conditions in the deposition unit.

Diffraction patterns preliminary recorded on the film indicated that all investigated films were polycrystalline. Almost in all cases, a very strong preferred orientation of crystallites perpendicular to the substrate, depending on the material and on the special conditions in the course of deposition, was observed. In case of zinc oxide films the preferred orientation is mainly in the [001] direction.

In case of continual sputtering there is a [001] preferred orientation of crystallites perpendicular to the substrate. (See X-ray diffraction patterns presented in fig. 1, 2 and 3).

The aluminium conductive layer resulted in a decrease of preferred orientation of ZnO crystallites (Fig. 1 and 2) as well as decrease of lattice imperfections, which can be observed in decreasing of microdeformations. Furthermore, in all cases of ZnO films whose thickness is 1 μm or less a considerable shift of (002) dif-

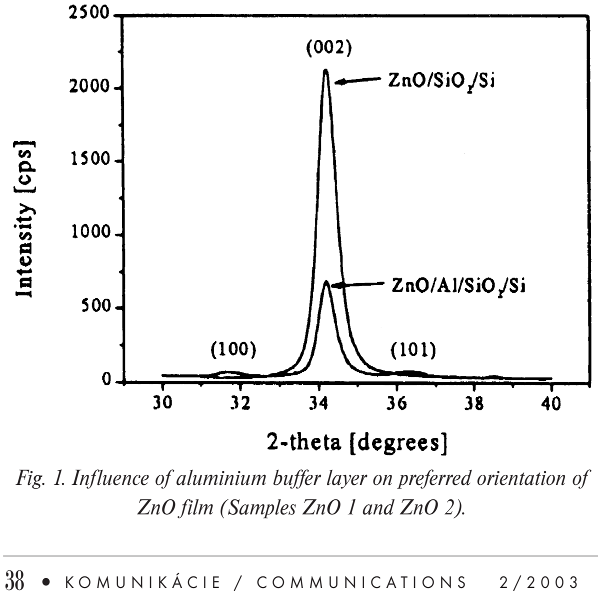

Fig. 1. Influence of aluminium buffer layer on preferred orientation of ZnO film (Samples ZnO 1 and ZnO 2).

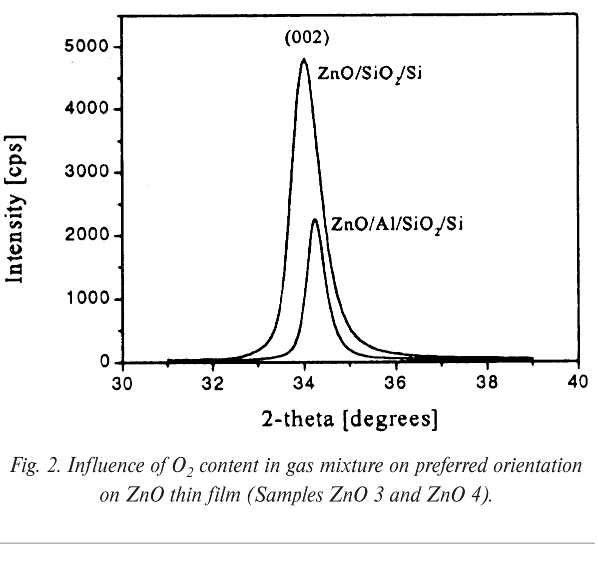

Fig. 2. Influence of O_2 content in gas mixture on preferred orientation on ZnO thin film (Samples ZnO 3 and ZnO 4).

fraction lines towards the lower diffraction angles was observed. When the thickness of ZnO film was 2,5 μm a considerable shift of (002) diffraction lines towards the higher diffraction angles was observed (See Table 2). Regular position of (002) ZnO line according to JCPDS standard is 34.44 deg. This line displacement is accompanied with the lattice strains which are present in the ZnO films due to lattice mismatch between the layer and substrate and due to the ion bombardment of films.

The increase of thickness from 1 μm to 2.5 μm resulted in considerable increase of crystallite size and decrease of the microstrains. Insertion of an Al_2O_3 layer between the Al and ZnO layers resulted in further increase of the crystallite size and decrease of the microstrains (Table 3).

It is apparent from Figure 3 that the use of 0.13 mm receiving slit on a diffractometer shows better asymmetry of the (002) line of ZnO thin films. The reason for this asymmetry is the stress gradient along the c-axis.

Influence of Al_2O_3 buffer layer on omega-scan is showed in Figure 4. The Al_2O_3 buffer layer resulted in an increase in width of the omega-scan trace.

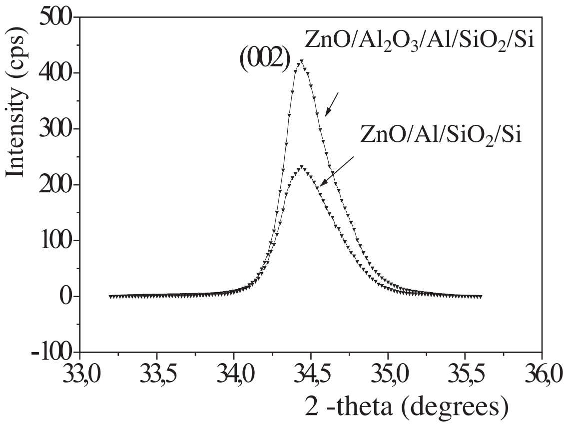

Fig. 3. Influence of Al_2O_3 buffer layer and thickness of ZnO thin film on preferred orientation of ZnO film (Samples ZnO 5 and ZnO 6).

The texture evolution depending on the substrate temperature during the deposition can be demonstrated on Zn_xO_y/Al_2O_3 multilayered structures prepared as sensitive layers for UV radiation. When substrate temperature during the deposition was kept below 300 °C, a part of amorphous phase was also observed. Much better

Data of investigated thin films obtained from X-ray diffraction

Table 2

Sample (thin film)	Investigated line	Line position	Intensity of $K_{\alpha 1}$ [cps]	FWHM [deg]	Integrated intensity [deg/s]
ZnO 1	002	34.184	436	0.4825	282.8
ZnO 2	002	34.205	1437	0.5568	1052
ZnO 3	002	34.216	1664	0.4591	1016
ZnO 4	002	34.027	2445	0.7335	2218
ZnO 5	002	34.480	1210	0.340	458.6
ZnO 6	002	34.480	2170	0.275	720.4
Zn_xO_y 1	002	34.265	5.9	0.4453	3,3
Zn_xO_y 2	002	34.379	32.47	0.5799	24.4
Zn_xO_y 3	002	34.372	724.4	0.4254	365.7

Size-strain data of investigated thin films

Table 3

Sample (thin film)	Investigated line	Integral breadth [deg] β	Shape factor $\Phi = FWHM/\beta$	Microstrains $\langle\epsilon\rangle \cdot 10^3$	Crystallite size D [nm]
ZnO 1	002	0.6493	0.7452	4.5	26
ZnO 2	002	0.7171	0.7764	5.9	28
ZnO 3	002	0.6104	0.7522	4.5	29
ZnO 4	002	0.9070	0.8087	8.6	27
ZnO 5	002	0.3791	0.8790	2.6	170
ZnO 6	002	0.3555	0.8208	1.6	400
ZnxOy 2	002	0.7462	0.7772	6.2	27
ZnxOy 3	002	0.5480	0.8427	5.3	97

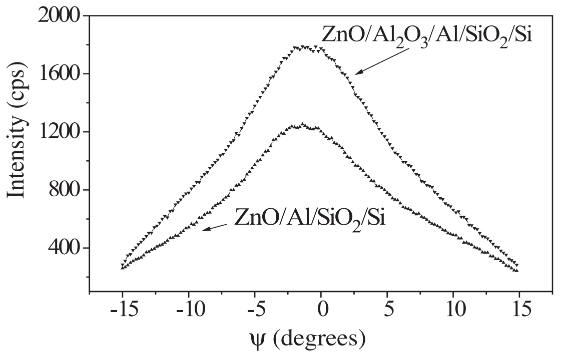

Fig. 4. Influence of Al_2O_3 buffer layer on the orientation distribution function of (002) planes ZnO thin film (Samples ZnO 5 and ZnO 6).

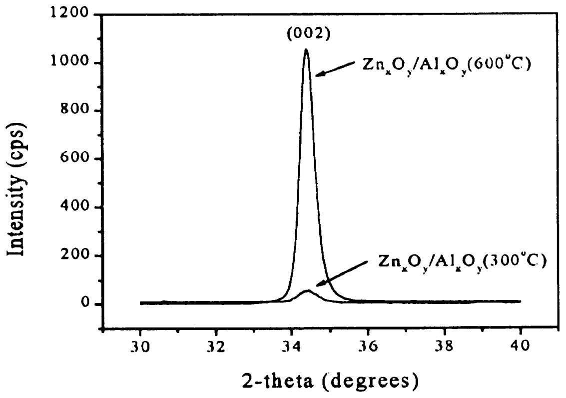

Fig. 5. Influence of substrate temperature on preferred orientation of Zn_xO_y/Al_2O_3 multilayered structure (Sample Zn_xO_y 2 and Zn_xO_y 3).

preferred orientation was observed when substrate temperature was kept on 600 °C (See Figure 5 and Table 2).

4 Conclusions

Our experiments indicated that the X-ray diffraction line profile analysis carried out on common X-ray diffractometer can be successfully used when investigating the microstructural properties of strongly textured thin films. The analysis is successful also in case when the film thickness is less than one micrometer. More attention has to be paid to the narrow lines because in case of their approximation by a non-appropriate profile the results can be over- or underestimated.

The obtained data about the influence of technology of preparation of thin films of ZnO as well as buffer layers on the structure of thin films of ZnO as well as other physical aspects were used to the improvement of preparation of the sensors of stress based on thin films of ZnO [7, 8].

Acknowledgement

The authors - would like to thank Prof. V. Tvarožek and Dr. 1. Novotny from Slovak University of Technology Bratislava for the preparing of samples and Prof. J.Fiala from ŠKODA Research Ltd. Plzeň, for the recording of preliminary diffraction patterns on the film and for valuable discussions during the preparation of the paper.

References

[1] SEGMULLER, A., NOYAN, I. C., SPERIOSU, V. S.: *X-ray Diffraction Studies of Thin Films and Multilayer Structures,* Prog. Crystal Growth and Charact. 18. (1989) pp. 21 - 66

[2] VAN BEI-KUM, J. G. M., VERMEULEN, A. C., DELHEZ, R., DE KEIJSER, TH. H., MITTEMEIJER, E. J.: *Applicabilities of the Warren-Averbach Analysis and an Alternative Analysis for Separation of Size and Strain Broadening,* J. Appl. Cryst.l-7, (1994) pp. 345 - 357

[3] LANGFORD, J. I. : *A Rapid Method for Analysing the Breadths of Diffraction and Spectral Lines using the Voigt Function,* J. Appl. Cryst. II, (1978) pp. 10 - 14

[4] DELHEZ, R., DE KEIJSER, TH. H., MITTEMEIJER, E. J.: *Determination of Crystallite Size and Lattice Distortions through X-ray Diffraction Line Profile Analysis*, Fresenius Z. Anal. Chem. 312, (1982) pp. 1 - 16

[5] BALZAR, D., LEDBETTER, H.: *Voigt-Function Modeling in Fourier Analysis of Size- and Strain-Broadened X-ray Diffraction Peaks,* J. Appl. Cryst. 26, (1993) pp. 97 - 103

[6] TVAROZEK, V. et al.: *Sensors and Actuators B*, 18-19,(1994) pp. 597 - 602

[7] TVAROZEK, V.: *Microsystem Technology in Biosensors. D.P. Nikolelis et al (eds.),* Biosensors for Direct Monitoring of Environmental Pollutants in Field, 351 - 371, Kluwer Academic Publishers. Printed in the Netherlands. (1998)

[8] NOVOTNY, L., SUTTA, P., MIKA, F., TVAROZEK, V.: *Piezoelectric ZnO Thin Films Prepared by Cyclic Sputtering and Etching Technology*, In: Proc. of the 20th International Conference on Microelectronics MIEL 95, Vol. I, held in Nis, Serbia, 12-14 September 1995 pp. 65 - 68

[9] SUTTA, P., et al.: *X-ray Diffraction Analysis and Optical Properties of ZnO Thin Films Prepared by Cyclic Sputtering and Etching Technique,* In: Proc. of the international conference ASDAM'96, held in October 22 - 26, 1996, Smolenice, Slovakia

[10] JACKULIAK, Q., SUTTA, P.: *Refinement of Method for Calculation of* $K_{\alpha 1}$ *and* $K_{\alpha 2}$ *Components of Diffraction Line*, In: Materials Structure in Chemistry, Biology, Physics and Technology. Vol. 3, (1996) No. 3, pp. 267 - 269

[11] BOROVSKIJ, I. B.: *Fizičeskije osnovy rentgenospektral'nych issledovanij,* lzdatel'stvo Moskovskogo universiteta, Moskva 1956

https://doi.org/10.26552/com.C.2003.2.41-43

P. Bury – Š. Barta – V. Magula – V. Slugen – T. Šmida *

ULTRASONIC INVESTIGATION OF PLASTICALLY DEFORMED STEEL-CONTRIBUTION TO ANALYSIS OF DEGRADATION INFLUENCE

Study of degradation influence on material properties of some steel components is very important because of their serviceable life. One of the most important side of the degradation process considering operation conditions is cumulated plastic deformation. The ultrasonic investigation of materials through the ultrasound attenuation and velocity measurements have been proved an effective tool of the study of structural changes caused also by plastic deformation due to the degradation process. In the contribution we present the results of both the frequency dependence of ultrasound attenuation and velocity measurements of steel samples (38ChN3MFA) with different relative plastic deformation (0, 1.5, 3 and 6 %). The results are compared also with the measurements obtained by some other techniques, including the measurement of electrical conductivity, and the rate of positron-electron annihilation and breakage toughness.

1. Introduction

Quantities characterising the propagation of high-frequency acoustic waves (ultrasound) in solid materials can be determined from the investigation of dependence of both acoustic waves velocity and attenuation on individual variables describing investigated properties of existing materials. The relation of velocity and attenuation of ultrasonic waves to various properties referred to intrinsic structure of solid material can then enable their study by means of ultrasonic velocity and attenuation measurement. Among these properties befit mainly elastic properties of materials, which reflect directly their intrinsic structure [1, 2].

Using the measurement of acoustic waves velocities and known values of density the elastic constants of solid materials, which are connected directly with inter-atomic forces, can be determined. The acoustic waves attenuation very sensitively reflects material intrinsic structure, not only the type of structure but also the changes due to defects occurrence (dislocations, grains etc.) Acoustic attenuation in metal materials depends on the way of preparation and further thermal treatment, that can influence a grain magnitude as well as the generation of dislocations or other defects. The attenuation also reflects permanent changes in material arising due to its strain [3].

In the case of material with a grain structure, dislocations or other defects the attenuation is caused by the dispersion, the frequency dependence of which depends on the rate of wavelength and mean defect size [1].

Presented contribution is orientated on analysis of degradation influence of material properties (steel 38ChN3MFA) with respect to serviceable life of produced components (for example girder M140) by investigation of cumulated plastic deformation. The structure changes of existing material were investigated for various degrees of plastic deformation using both attenuation frequency dependence and ultrasound velocity measurements. Obtained results were in detail compared with results obtained by other methods on the same samples.

2. Experiment

Investigated material was chosen from non-operated girder M140 and four sample series corresponding to four different material conditions were prepared; original (0 % of relative plastic deformation in strain); 1.5 %, 3 % and 6 % of tensile deformation Nevertheless, the 6 % relative plastic deformation corresponded to the strain just before the tensile strength level [4].

Samples for the acoustical investigation were prepared in the cylinder shape with diameter $d = 13$ mm and high $h = 8.65$ mm. The velocity and attenuation were measured for ultrasonic wave propagated in the direction of cylinder axis (x) and there by in deformation direction, but also in the direction perpendicular to cylinder axis(y) with faces separated by $l = 10.78$ mm.

Acoustic measurements of the both velocity and attenuation were made in frequency range of 10 – 100 MHz using pulse method and longitudinal acoustic waves generated by quartz transducers. All measurements were performed at room temperature.

---

* **[1]P. Bury, [2]Š. Barta, [3]V. Magula, [2]V. Slugen, [3]T. Šmida**
[1]Department of Physics, Faculty of Electrical Engineering, Žilina University, 010 26 Žilina
[2]Department of Physics, Faculty of Electroengineering and Informatics, Slovak Technical University, 812 19 Bratislava
[3]Welding Research Institute, Račianska 71, 832 59 Bratislava

3. Results and discussion

The results of velocity measurement for both propagating directions and corresponding elastic modules for the cylinder axis direction are summarised in Table 1. The velocity measurements were made at frequency of 12 MHz with accuracy better than 2.10^{-3}. The graph of frequency dependence of ultrasonic attenuation measured for individual samples is in Fig. 1.

Ultrasonic velocity measurements for all samples and two propagating directions (x and y) and elastic modules for propagating direction x. Table 1

plast. defor. (%)	$v_{L(X)}$ [m/s]	$v_{L(Y)}$ [m/s]	E_x [Pa]
0	5553	5580	24.14×10^{10}
1.5	5553	5580	24.14×10^{10}
3	5537	5595	24.00×10^{10}
6	5676	5603	25.22×10^{10}

The results obtained by the measurements of attenuation and velocity correlate considerably with results of other measurements obtained on the same samples, mainly the measurement of positron-electron annihilation rate, measurement of impact toughness by measuring of transient temperature and measurement of static breakage toughness. The most important results of mentioned measurements are summarized in Table 2.

Summarized results of measurement of plastic deformation influence on some physical characteristics. Here, *T50%* and *T60J* are the transient temperatures measured at impact work 60 J and temperature of 50 % plastic breakage, respectively, $K_{0,2}$ is the static breakage toughness for crack growth 0.2 mm, ρ is the electric resistivity and τ is the positron lifetime. Table 2

Measured characteristic	Plastic deformation [%]			
	0	1.5	3	6
T50 % [°C]	−82	−74	−72	−65
T60J [°C]	−63	−68	−53	−42
$K_{0,2}$ [MPa$\sqrt{\text{m}}$]	182	190	159	152
$10^8\ \rho$ [$\Omega\mu$]	29.4	29.5	29.1	28.7
τ [ps]	174.5	172.5	179.7	178.3

On the base of results of impact and static breakage toughness tests, it is necessary to state that a plastic deformation of girder material in the range of 0 – 6 % shows only lightly expressively on its resistance against a brittle damage. In spite of a relatively small differences in measured values and with consideration of results possible dispersion, the expected slow increase of transient temperature and slow decrease of breakage toughness values due to the plastic deformation up to 6 % was indeed confirmed, but from the respect to safety operation of girders it is not important.

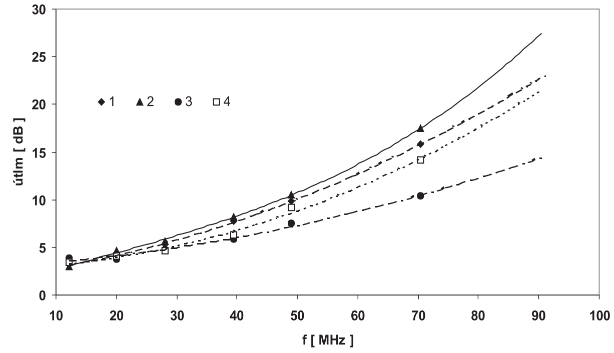

Fig. 1. Frequency dependence of ultrasonic attenuation for the samples with different value of relative plastic deformation: 0 % (4); 1.5 % (1); 3 % (2) and 6 % (3).

The test of static breakage toughness that presents at 20 °C more reproducible results simultaneously indicated that the marked properties degradation occurs between 1.5 and 3.0 % of plastic deformation. The differences between the values of static breakage toughness of original material and material after 1.5 % deformation, as well as between materials after 3 % and 6 % deformation, respectively, were intro-dispersion of measurements.

The relative small influence of plastic deformation in the range of 0 – 6 % is with respect to mechanical properties of the girder [4] understanding. It could he seen from the tensile pattern that there is not any deformation hardening in the range of 0 – 1.5 %. In addition the 1.5 % relative tensile deformation represents only small fraction of the material deformation efficiency (tensibility about 18 % and contraction almost 60%). Therefore there is no reason for its important influence on the toughness.

The decrease of the toughness after plastic deformation in the range of 1.5 – 3 % is with largest probability caused by the strength matrices development due to the relative important deformation hardening. It is evident that the deformation hardening is the most marked at deformations in the range of 1.5 – 3 %. From the volume constancy of plastic deformation but follows, that the contraction value at 3 % relative tensile deformation range only on the level below 5 % of total material plasticity. So small loss of plasticity due to the considering natural measurements dispersion could be hardly registered on the value of static breakage toughness and transient temperature, respectively.

On the other side, the rate of deformation hardening over ~ 3 % of relative tensile deformation again decreases, which indicates a relatively small increase of strength matrices behind the strength limit. With respect to small increase of strength matrices, the influence of cumulated plastic deformation would be registered more significantly only in the case of considerably higher values of plastic deformation.

The results obtained by measurements of both frequency dependence of ultrasonic signal and positron-electron annihilation exhibited already at preliminary measurements to be promising.

The values of both physical characteristics in the range of 0 – 1.5 % of relative tensile deformation were practically constant. Measured differences are in the frame of measurement error, which correlates with zero matrices hardening in the initial stages of plastic deformation.

In the range of 1.5 – 3 % of plastic deformation the marked increase of ultrasonic attenuation over 50 MHz was registered similarly as increase of mean positron lifetime, which indicates a change in the state of lattice defects. Taking into consideration the fact, that the total plastic deformation depends directly on the density of dislocation lines in matrices, that should be necessarily changed during initial deformation phases the behaviour of both parameters are with largest probability the mark of raising sensitivity of both methods on the cluster creation of intersected dislocations (dislocation forest) during initial stages of plastic deformation.

However, the attenuation values measured in the range of 3 – 6 % indicate comparing with the values of mean positron lifetime different sensitivity on defects number and configuration – the mean positron lifetime is practically constant while the attenuation significantly decreases. The small deformation hardening recognised in existing range indicates probably the beginning of creation of that areas with reduced density of dislocation lines and these areas alternate with areas with increasing dislocation density. It is possible that the method at ultrasonic attenuation measurement is more sensitive to the creation at dislocation substructure, however this assumption should be verified by additional measurements.

4. Conclusion

In conclusion we can state, that methods of ultrasonic attenuation and velocity measurement definitely recorded the region of 1.5 – 3 % plastic deformation, which is not indication of important reduction of material toughness, but it indicates the formation of degradation proces, that could manifest negatively at higher deformation values and the speed of which could be much higher at cumulated values of 3 – 6 % with respect to the small speed of deformation hardening. From the point of view of further operation of girder M 140 it was found that a plastic deformation does not cause important change of breakage properties and is not manifested on equipment safety. Regarding to possible utilisation of this method for monitoring of cumulated plastic deformation as well as also girders safety (residual lifetime), we can state that the measurement of ultrasonic attenuation over frequency 50 MHz after results verification using larger sample set could probably serve as check non-destructive method for monitoring of the rise of cumulated plastic deformation that does not influence indeed the girder residual lifetime but indicates at the values ~ 3 % the beginning of the stage when the value of cumulated plastic deformation can increase beyond control at small increase of nominal loading.

References:

[1] MASON, W. P.: *Physical Acoustics*, Vol. IV, Academic Press, 1966
[2] PAPADAKIS, E. P.: *Ultrasonic Instruments and Devices*, Academic Press, 2001
[3] TRUEL, R., ELBAUM, CH., CHICK, B. B.: *Ultrasonic Methods in Solid State Physics*, Academic Press, 1969
[4] HAMÁK, I., et. al.: *Residual lifetime of girders M 140 after long-time operation*, Order No. 222/2167 VÚZ Bratislava, September 2000

https://doi.org/10.26552/com.C.2003.2.44-47

Dalibor Blažek – Jozef Kúdelčík – Jozef Blažek *

A DESIGN OF AN INDUCTION METHOD DEVICE WITH RESPECT TO THE SIGNAL AND NOISE SENSITIVITY

An objective of this article is the relationship between the signal sensitivity, the noise sensitivity and the distribution of turns of winding on any chosen axis-symmetric core.

The analytical study originates from Faraday induction law and Nyquist theorem. Different windings were compared with respect to their physical properties.

1. Introduction

Induction method is often used for the measuring of low frequency magnetic field. The optimization of equipment in Fig. 1 consists of looking for the best combination of material of the core, its shape and winding. The relation between the material susceptibility, the core shape and the resultant sensitivity of the equipment was analyzed in [1]. An objective of this article is to find the relationship between the signal sensitivity, the noise sensitivity and the distribution of turns of winding on any chosen axis-symmetric core.

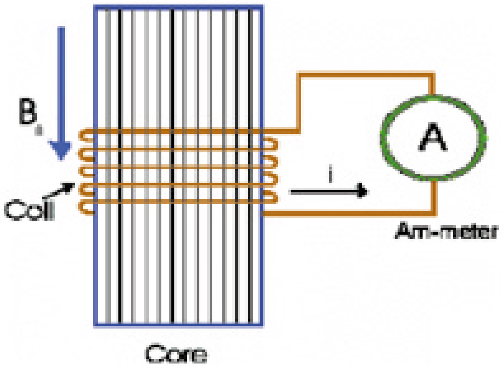

Fig. 1. The scheme of the studied equipment

First, the analytical study based on Faraday induction law is done. In this step the impact of the amount of turns and the distribution of turns on the core on the sensitivity are separated. Investigation of thermal noise originates from Nyquist theorem [2]. As a result of the theoretical part one has optimization criteria for searching the windings.

The relevant physical properties of each winding are self-inductance and mutual inductance of the turn and applied magnetic field. These properties are calculated by the finite element method. Next, a computer program for finding the best winding is used. Different windings were investigated on the cylindrical core having the length of 1 m, diameter of 0.084 m and susceptibility of 5000 inserted into a quasi stationary homogeneous magnetic field.

2. An induction method

Magnetic flux through the winding is proportional to a flux density of the applied magnetic field B and the value of electric current I in the circuit

$$\Theta = M B + L I, \tag{1}$$

where self-induction L and mutual inductance M are functions of the shape, material of the core and functions of distribution of turns on the core.

Periodical change of flux density with angular speed ω and amplitude B_o causes current with the amplitude

$$Io = \frac{\omega M}{\sqrt{R^2 + \omega^2 L^2}} B_o, \tag{2}$$

where R is the circuit resistance.

The normally used windings have so many turns n that it is possible to use integration through the density of turns

$$\rho(x) = \frac{1}{n}\frac{dn}{dx}. \tag{3}$$

The density of turns ρ is normalized function $\int_0^l \rho(x)dx = 1.$ Various windings differ by the number of turns and by the distribution of turns on the core.

The coefficients L, M in (1) can be determined only by a computer program calculating the distribution of magnetic field

---

* [1]**Dalibor Blažek,** [1]**Jozef Kúdelčík,** [2]**Jozef Blažek**
[1]Department of Natural Sciences, Faculty of Science of the University of Žilina, J. M. Hurbana 15, 010 26 Žilina, Slovakia, Tel. ++421-41-5625982 kl. 18, E-mail: blazek@fpv.utc.sk, kudelcik@fpv.utc.sk
[2]Air Force Academy Rampova 7, 041 21 Košice, Slovak Republic E-mail: blazek@dol.sk

in the space. Using (3), it is possible to separate the whole numbers of turns n from their distribution ρ. The result of modification is

$$M = \int_0^l n(x)\, M(x)\, dx = n \int_0^l \rho(x)\, M(x)\, dx = n\, M_1, \qquad \text{(4a)}$$

$$L = \int_0^l n(x)\, L(x, y)\, n(y) dx dy =$$

$$= n^2 \int_0^l \int_0^l \rho(x)\, L(x, y)\, \rho(y) dx dy = n^2\, L_1, \qquad \text{(4b)}$$

where the operator $M(x)$ (Fig 2a) and operator of self-induction $L(x, y)$ (Fig. 2b) are determined numerically for each core by the finite element method. The coefficients L_1, M_1 are self-induction and mutual induction of the winding standardized per one turn.

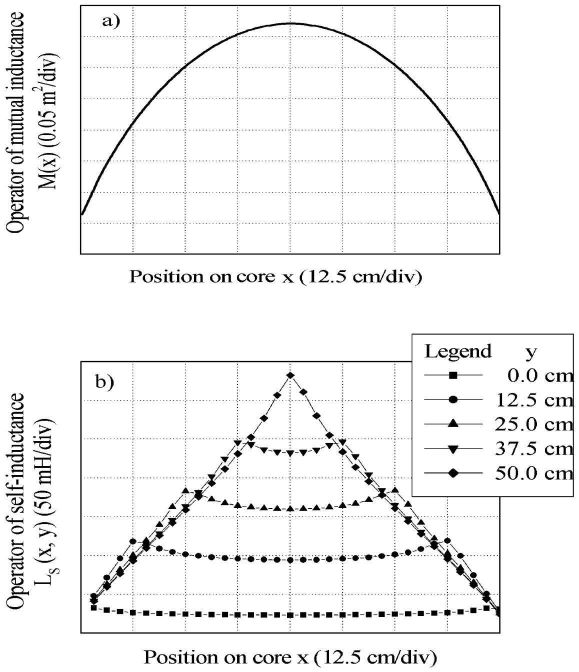

Fig. 2. a) Development of the operator of the mutual inductance M(x) of the winding and applied homogeneous magnetic field B_o. Variable x goes through the length of core. b) Development of the symmetrised operator of self - inductance $L_S(x, y) = L(x, y) + L(x, l - y)$. Developments were calculated by Finite element method.

The resulting circuit resistance consists of an internal resistance of the measuring apparatus R_A and winding resistance R_W. The winding resistance is proportional to the number of turns n, so one can define $R_W = n\, R_1$. The total circuit resistance is

$$R = R_A + n\, R_1, \qquad \text{(4c)}$$

Adding (4a, b, c) into (2), one gets the signal sensitivity of equipment

$$k_S = \frac{I_o}{B_o} = \frac{n\, M_1\, \omega}{\sqrt{(R_A + n\, R_1)^2 + \omega^2\, n^4\, L_1^2}}\ . \qquad \text{(5)}$$

3. Thermal noise

Each electric circuit exhibits fluctuations in thermal equilibrium. These fluctuations are superposed to the measured signal as noise. The important parts of noise in studied equipment are noise of magnetic core (i.e. Barkhausen`s jumps) and Nyquist thermal noise. The effective value of thermal noise current is

$$I_{ef}^2 = \frac{k_B\, T}{2\pi} \frac{R}{|Z|^2} \Delta\omega = \frac{k_B\, T}{2\pi} \frac{R}{R^2 + \omega^2\, L^2} \Delta\omega, \qquad \text{(6)}$$

where k_B is Boltzman constant, Z is impedance of circuit, R (4c) is total circuit resistance and $\Delta\omega$ is bandwidth of the signal. The noise sensitivity is

$$k_N = \frac{I_o}{I_{ef}} = \sqrt{\frac{2\pi}{k_B\, T}}\, \frac{\omega B_o}{\sqrt{\Delta\omega}}\, \frac{M}{\sqrt{R}}\ . \qquad \text{(7)}$$

Temperature T, amplitude of measured flux density B_o, frequency of measured signal ω and the bandwidth $\Delta\omega$ of amplifier have nothing in common with the winding, so they are suspect to be external quantities to the winding. Noise purity of the signal is the best if the winding with the maximal portion $M/\sqrt{R}$ is used. Adding (4a, c) one gets:

$$k_N \equiv \frac{M}{\sqrt{R}} = \frac{n\, M_1}{\sqrt{R_A + n\, R_1}}\ . \qquad \text{(8)}$$

Noise sensitivity (8) is a monotonic increasing function of number of turns n. In terms of the signal purity, the optimal number of turns does not exist.

So, one needs another approach. The winding resistance can be expressed as a function of the electrical conductivity of used material σ, the cross area of used conductor S and its length d. The optimal winding can be found under the condition that the volume of material used for wire $V = d\, S$, is a given constant parameter. Then, the winding resistance is

$$R_W = \frac{1}{\sigma} \frac{d}{S} = \frac{1}{\sigma} \frac{d^2}{V} = \frac{d_1^2}{\sigma V} n^2 = \alpha\, n^2, \qquad \text{(9)}$$

where d_1 is a length of one turn and α is appropriate substitution. The total circuit resistance is $R = R_A + \alpha\, n^2$ and

$$k_N \equiv \frac{n\, M_1}{\sqrt{R_A + \alpha\, n^2}}\ . \qquad \text{(10).}$$

The noise sensitivity (10) is a monotonic increasing function of n and converges the value $M_1/\sqrt{\alpha}$ to its limit. It is suitable to express the number of turns n as a function of new parameter ϵ, $\epsilon \in \langle 0, 1 \rangle$. The implicit form of this function is $k_N(n_\epsilon) \equiv \epsilon\, M_1/\sqrt{\alpha}$. Using (10) one gets the explicit form

$$n_\epsilon = \sqrt{\frac{\epsilon^2}{1 - \epsilon^2} \frac{R_A}{\alpha}}\ . \qquad \text{(11)}$$

Then, the winding resistance and circuit resistance are

$$R_W(n_\epsilon) = \frac{\epsilon^2}{1 - \epsilon^2} \text{ and } R(n_\epsilon) = \frac{1}{1 - \epsilon^2} R_A\, , \qquad \text{(12)}$$

respectively.

Substituting $p = \alpha(\omega L_1)^{-1}$ one gets a relation for noise sensitivity:

$$k_N = \sqrt{\frac{2\,\pi\,\omega}{k_B\,T\,\Delta\omega}\;\frac{M_1\,B_o}{\sqrt{L_1}}\;\underbrace{\frac{\epsilon}{\sqrt{p}}}_{x}}\,. \qquad (13)$$

and adding (14), (15) into (5) one gets :

$$k_S = \frac{1}{n_\epsilon}\,\frac{M_1}{\sqrt{L_1^2 + \left(\dfrac{\alpha}{\epsilon^2\,\omega}\right)^2}} = \frac{1}{R_A}\,\frac{M_1\sqrt{\omega}}{\sqrt{L_1}}\,\underbrace{\sqrt{\frac{p\,\epsilon^2\,(1-\epsilon^2)}{\epsilon^4 + p^2}}}_{y}\,. \qquad (14)$$

for final sensitivity.

The most important result of this article is the relation between the noise sensitivity and the signal sensitivity which can be expressed in the form

$$y = \sqrt{\frac{x^2 - p\,x^4}{1 + x^4}}\,. \qquad (15)$$

This relation (15) is demonstrated for different values of the parameter p in Fig. 3. It can be seen that the decrease of the parameter p (i.e. using more material with better conductance) leads to the increase of both the signal and the noise sensitivity. This effect is considerable until $p > 0.01$.

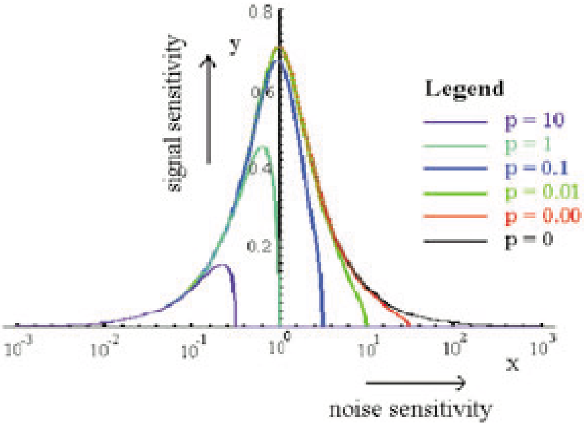

Fig. 3. Relation between noise sensitivity and signal sensitivity as a function of parameter p.

4. Optimal distribution of turns in winding

Another result comes from the comparison of the relations (13) and (14). The appropriateness of windings have to be measured by the ratio $M_1/\sqrt{L_1}$.

On the core there can be an infinite number of different windings. In real time one can search for only a finite amount of possibilities. So, the development of the density of turns $\rho(x)$ was tabulated in 17 incremental points on the whole length of core. Because of the mirror symmetry of the system the symmetrical windings $\rho(x) = \rho(l - x)$ were investigated only. In the process of searching, 23 million windings were compared.

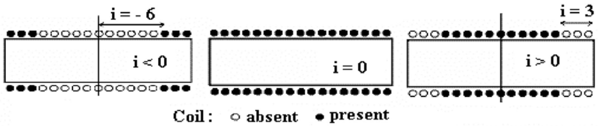

Fig. 4. Distribution of the turns ρ(x) on the core, for different values of index i.

Processes of optimization were done for many different situations. In spite of a huge set of possibilities, the results belong to a small set of windings. Therefore, it may be useful to know their physical properties, see Fig. 5. One can index these windings by one parameter, for example i, which describes the distribution of turns on the core, see Fig. 4. If $i = 0$ the turns are homogeneously distributed along the core. For $i < 0$ the windings are concentrated on the edges of core and for $i > 0$ the turns are close to the centre.

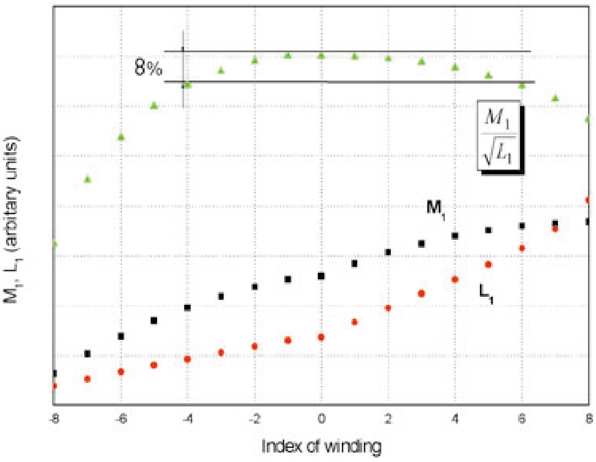

Fig. 5. Physical properties for special windings. Self-inductance L_1 and mutual M_1 inductance are standardized per 1 turn. Signal sensitivity k_S is proportional to $M_1/\sqrt{L_1}$.

In the case of cylindrical core there are many windings with almost the same appropriateness (Fig. 5). This fact enables a designer to satisfy other criteria in a process of construction. In any case the optimal number of turns should be.

Acknowledgement

Research was supported by the VEGA Grant 1/1714/20. The presented results are useful for implementation on ELF magnetic antenna produced by EDIS, the company for electronic digital systems in Košice and for a research team monitoring the Schumann resonances at the Astronomical and Geophysical observatory (Faculty of Mathematics, Physics and Informatics, Comenius University) at Modra-Piesok.

References:

[1] KÚDELČÍK, J., BLAŽEK, D., BLAŽEK, J.: *Physical application and optimization a shape of core for experience.* 11th Czech and Slovak Conference on Magnetism, August 20 - 23 2001, Košice

[2] PÉCSELI, H. L.: *Fluctuations in Physical Systems*, Cambridge University Press 2000

https://doi.org/10.26552/com.C.2003.2.48-53

KOMUNIKÁCIE
COMMUNICATIONS

Tadeusz Kasprowicz – Leopold Kruszka – Ryszard Rekucki *

DYNAMIC RESPONSE OF A TRUNK STRUCTURE BUILDING TO MULTIPLE TRANSIENT LOADINGS

The paper provides information concerning the dynamic response of building structures exposed to paraseismic loadings. Dynamic loadings can arise inside buildings or can be transmitted to buildings through subsoil, causing vibrations of structures. To carry out a dynamic diagnostics of existing buildings, it is necessary to take measurements of vibration parameters directly from the investigated structure. The paper presents some examples of such investigations, as well as a comparison of the obtained results and calculations with standard dynamic characteristics of existing buildings.

Key words: *structure, dynamics, paraseismic loading*

1. Introduction

Building structures, during many years of operation life, are subject to various dynamic influences, coming from sources located outside the building (for example – street traffic, construction machines' activities) as well as those inside the object (air conditioning and ventilation equipment, *personal* and cargo lifts, other machines and equipment, installed in the object under consideration). In accordance with the valid law (Art. 62 of the Building Law [1]) users are obliged to carry out, at least once every five years, basic periodical checks aimed at the evaluation of the technical state and usability of the building, related to the efficiency of the whole structure under conditions of the existing and planned influences. Such checking procedure should deliver an answer as regarding the possibility of the object's further use in a defined operation life and present guidelines concerning repairs, operation and maintenance limitations and recommendations for the future.

Technical diagnostics encompasses all influences, including dynamic ones, which are main factors [2] affecting the conclusions' correctness. An excessively high level of dynamic influences leads to a premature wear of individual elements of buildings' structure. Characteristics of dynamic loads as defined by their course in time are considered, mostly, at the point of their affecting the structure or at the point of where they are received by the structure's element are.

Investigations of dynamic influences affecting buildings and construction structures are often closely linked with practical difficulties resulting from stochasticity of the process observed. They occur not in defined and repeatable laboratory conditions but, in the natural environment, in a situation when vibrations sources are of a non-determined character. Such a situation makes it necessary to measure vibrations within the building being diagnosed, in order to statistically process the results and to interpret them professionally.

In each individual case, dynamic measurements have to be carried out in conditions representative of the effects considered (for example, one must not limit the number of dynamic loads' sources occurring in a normal operation and maintenance conditions). In further part of the paper results of investigations non-stationary multiple transient dynamic influences affecting the work of reinforced concrete and steel structure of an administration and office building will be presented.

2. Description of dynamic investigations

The measurements of dynamic loadings concerning an existing multi-storey building of two- shaft structure (towers "A" and "B") situated in Warsaw at a distance of about 150 m to the North – West from the intersection of Powązkowska Street and Zygmunt Krasiński Street. The aim of the measurements was to determine causes of falling off the walls' façade plates, made of architectural glass. Recently, in the building's vicinity, the roadway of Powązkowska Street has been widened and a multi-storey apartment block has been built. In the aftermath of these, the nearby traffic increased over that determined in the technical design. During the realisation of measurements, the following multiple transient loadings were affecting the structure:

- loads acting directly on the considered structure, the source of which was located inside the building (new lifts, air condition appliances, electric motors).
- loads being transferred upon the building's structure through subsoil and air (street traffic, wind).

The measurements and diagnostic analysis were carried out, based on recommendations contained in valid standards regulations and those found in literature concerning building structures diagnostics.

---

* **Tadeusz Kasprowicz, Leopold Kruszka, Ryszard Rekucki**
Wojskowa Akademia Techniczna, ul. Kaliskiego 2, skr. poczt. 50, PL-00-908 Warszawa 49, Poland, E-mail: tkasprowicz@wat.edu.pl

2.1. Description of diagnosed object

The building in 46/50 Powązkowska Street, undergoing a periodical technical evaluation constitutes an objects' system consisting of two buildings (towers "A" and "B"), nine and ten floors high, connected by a linking member, and the ground floor part of height up to 8.70 m. Both towers are a trunk construction. Demonstrative outlines of objects considered are shown in Fig. 1.

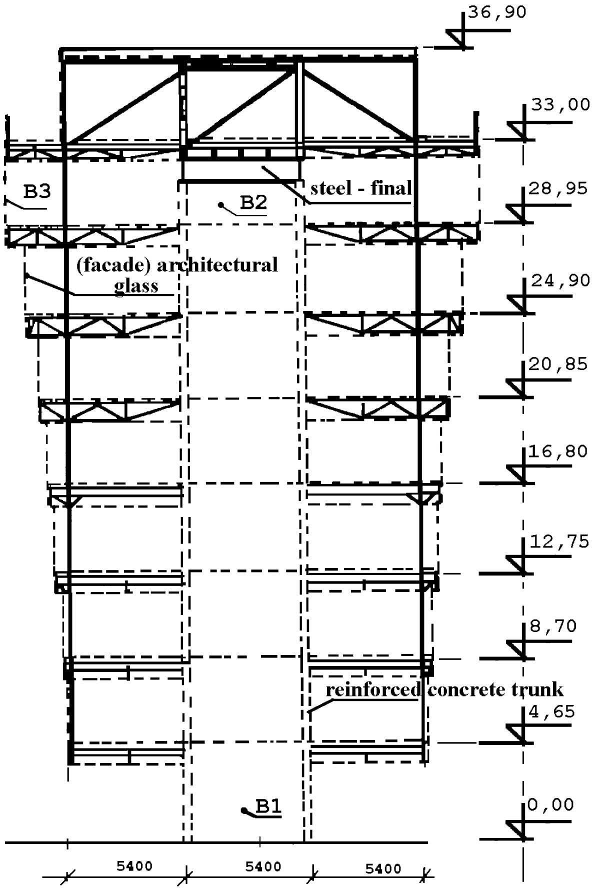

Fig. 1. Demonstrative outlines of diagnosed object - tower "B" with locations of measurements points: B_1, B_2 and B_3.

The main carrying elements of the buildings' structure are reinforced concrete trunks, of axial dimensions, in a horizontal projection of 5.40 m by 5.40 m and of the wall 30 cm thick. The height of tower "A" is 41.45 m and that of tower "B" - 38.10 m. Steel cantilever cornices were mounted on the upper edge of the reinforced concrete trunks. Steel vertical hangers supporting the steel structures of the beams of individual floors were attached to the supports' endings. The beams ends are supported directly on the reinforced concrete trunks through the intermediary of brackets welded to marks anchored in the trunks' concrete. Axial dimensions of floors in a projection are 16.2 m by 16.2 m, they widen upwardly up to the dimensions of 21.5 m by 21.5 m. Two lift shafts are situated within each of the two trunks. The engine rooms of the lifts found their place on the highest floors (on the eighth and ninth respectively). The inter-storey floors are supported on steel beams of 2 m spacing on which rolled steel sheets were spread out and a reinforced concrete plate, minimum 5 cm thick was placed. The height of an individual floor is 4.05 m, and that of floor structure is 1.05 m.

The structure of façade walls was mounted on individual floors' edges. Window elements, 150 cm wide, are separated by 30 cm wide full elements of the façade walls. The inner parts of those walls are made of "Baletice" - type plates. The outside of the structure is covered with 3 mm thick architectural glass and the inside by asbestos-cement plates. Schematic pictures of façade walls are shown in Fig. 2.

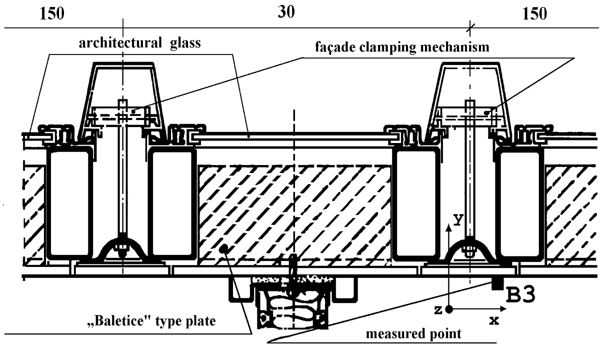

Fig. 2. Façade wall cross-section and location of measurement point B3.

The linking member structure is situated between two towers, which are expansion - joined with them in both planes. The structure is of the same height as tower "B". The design structure of the linking member is based on a system of steel columns (pillars) anchored in the foundations. As working action of the linking member itself has no direct effect on the behavior of the structural elements of façade walls, no dynamic investigations on the linking member pillars were conducted.

The structures of one-floor high extension buildings are separate objects and were omitted in the diagnostics of the towers' structures.

2.2. Object's foundation in subsoil

The soil in the immediate foundation area of individual buildings of the structure's aggregate in 46/50 Powązkowska Street belongs to weak subsoils. For this reason, the separate foundation plates of the towers "A" and "B", and the linking member were founded on reinforced concrete pillars. Directly on the foundation plate, the reinforced concrete trunks of the towers were founded. The structure of the tower's foundation is shown in Fig. 3. Such a type of foundation results in a very low turning of the plate as well as in the structure's resistance to dynamic loads transferred through the subsoil.

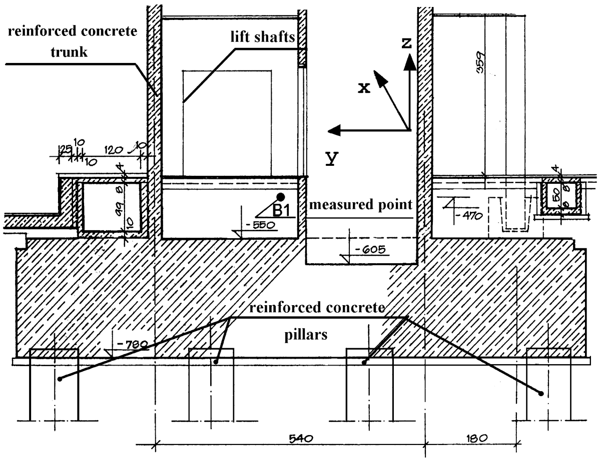

Fig. 3. Structure of tower's foundation and location of measurement point B1.

2.3. Characteristics of equipment and of measurement procedure

For the evaluation of dynamic effects, it is necessary to objectively determine their level through a direct measurement, realised at the construction site. In the system under consideration, vibrations have a multiple, transient character, close to random ones. The diagnostic procedure in this case consists in measuring real-time vibrations and then, statistically processing the obtained results. According to the PN-85/B – 02170 standard [5], a measurement line has to comprise measuring gauges (transformers), signal formation system, and a recording or displaying device.

Based on standards-related requirements and those concerning the structure being diagnosed, changes in the time of vibration acceleration values in selected points, characteristic for the building's design structure, have been adopted as measurement parameters. To this end, the accelerometers (PCB Piezotronics) have the following measurement characteristics:

1. Model 393B12 – sensitivity about 982 mV/ms^{-2}, measurements range from $8 \cdot 10^{-5}$ ms-2 to 4.9 ms^{-2}, measured frequency range 0.1 – 1000 Hz.
2. Model 393A03 – sensitivity about 100 mV/ms^{-2}, measurements range from $8 \cdot 10^{-5}$ ms^{-2} to 49 ms^{-2}, measured frequency range 0.1 – 1000 Hz, were used.

These parameters fulfil the requirements defined in the relevant standard and the accelerometers also posses a currently valid certificate for the agreement with the ISO 10012 – 1 and military standards of MIL-STD 45662A. The indication accuracy of the whole measuring system used in the testing does not exceed 2 %. The diagram of the measuring system is shown in Fig. 4.

Signal from measuring transformers, fixed to the standardised measurements cube, along mutually perpendicular axes *x*, *y*, *z*, was transmitted to an 8-channel M482A18 amplifier (PCB Piezotronics), with amplification capabilities of 1, 10, 100 – simultaneously from two measurement points. The measurements cube, with its sensors, during vibration observations, was permanently fixed to the building's structure with the help of a magnetic connector and a specially designed steel plate fixed to structure's material in the site selected for observations of dynamic responses.

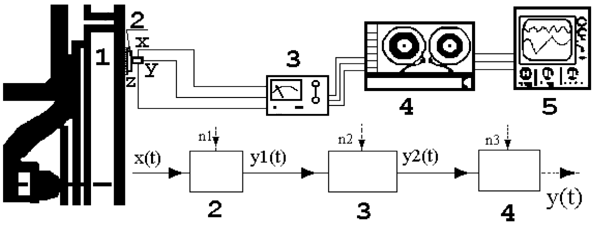

Fig. 4. Diagram of the measurement set for recording vibrations of building's structural elements: 1 – panel wall – investigated element, 2 – piezoelectric accelerometers, 3 – multi-channel amplificatory of the loading and signal formation, 4 – multi-channel magnetic recorder, 5 – multi-channel digital control oscilloscope.

Following its appropriate amplification, an analogue signal was recorded on the BASF E-240 magnetic tape of the professional 24-channel V-STORE recorder (RACAL). The recording was conducted randomly (in conditions of the building's use) at two points, with transformers fixed along *x*, *y*, *z*-axes. In each case, the measurement of three 5-minutes time slots was made. For current observation of the vibration level and for proper determination of amplifications necessary on individual constitutive members of the measurements' lines a 4-channel digital oscilloscope of the 0 – 8 GSa/s measurements band was used. The oscilloscope's software makes it also possible to speedily decompose the signal observed in the domain of time into the signal imaged in the domain of frequencies, which enables a correction of the measurement parameters.

2.4. Distribution of measuring gauges during experiments

Following the analysis of the static system of the relevant structure, and the attempt of paraseismic diagnosis (determining the causes of falling-off of the façade glass plates during building's maintenance) while taking into account technical conditions for installing accelerometers on the object's load-bearing structure it was decided that the recording of acceleration values in the function of time would be conducted on the tower's trunks, in the technical rooms on the lower ground floor level, that of the seventh floor and on the façade wall structure of the Powązkowska Street side, at a point distanced 5.50 m (tower "A") and 6.50 m (tower "B") from the building's corner.

During the first experiment, measuring gauges were positioned in the following places: point A1 – on the trunk of tower "A" on a lower ground-floor level, at a point 80 cm above the floor level (measurement relative to *x*, *y* and *z* axes) and adequately point B1 (Figs 1 and 3) – on the trunk of tower "B" on a lower ground-floor level, at a point 80 cm above the floor level (measurement relative to x, y and z axes). In the second experiment, measuring gauges were located at the following points: A2 – on the trunk of tower "A", on the seventh floor level, at a the point 80 cm above the floor level (measurement relative to x, y and z axes), A3 – on the façade wall structure, on the same floor in a corner room from the Powązkowska Street side, at the point 120 cm above the floor level (measurement relative to x, y and z axes).

During the third experiment measuring gauges were positioned in the following points: B2 (Fig. 1) on the trunk of tower "B" on the seventh floor level at a point 80 cm above the floor level (measurement relative to x, y and z axes), B3 on the façade wall structure (Figs. 1 and 2), on the same floor, in a corner room from the Powązkowska Street side, at a point 120 cm above the floor level (measurement relative to x, y and z axes).

3. Analysis of measurement results.

3.1. Apparatus and software used in the analysis of measurement signals

According to the PN-85/B-02170 Polish Standard, a non-direct method of measurements had to be adopted, consisting in analogue recording of the vibrations' acceleration signal on a magnetic tape and a following spectral analysis of the signal recorded in laboratory conditions.

Quality analyses were conducted with the help of the "Vibrations" software package in the STYST environment, and the statistical evaluations, i. e. correlation and regression coefficients, with the help of SYSTAT software – Fig. 5.

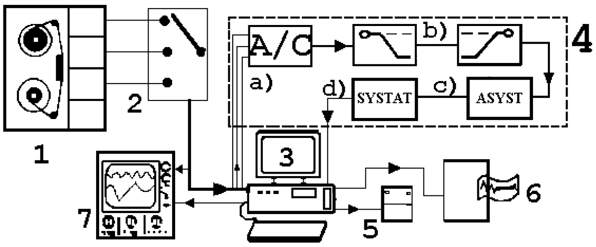

Fig. 5. Diagram of measurement set for measurement data analysis and sensing the vibrations of the building's structural elements: 1 – multi-channel magnetic recorder, 2 – channel selector, 3 – computer, 4 – computer module for digitising and an analysis of measurement signals, (a – analogue-to-digital converter , b – digital low-and-high pass filter, c – ASYST software for analysis and gathering, d – SYSTAT software for statistical analysis , 5 – floppy or compact disk, 6 – printer or plotter, 7 – oscilloscope.

The quantification and sampling of the analogue signal into the digital one, used in the analyses, was conducted on a digital four-channel oscilloscope with the frequencies of 250 samples per second and 1000 samples per second, with generated at the level of 0.8 of the maximal observed value being measured.

Discrete vibration runs were recorded, in the function of time, being of a 1024 points' length, which constitutes 4096 ms for 250 samples per second, and 1024 ms at the 1000 samples per second of sampling.

Data series from individual measurement points, registered separately from x, y and z axes were subjected to initial processing by conducting a scale change, depending on the given accelerometer's sensitivity, from signals expressed in volts to those expressed in ms^{-2}.

3.2. Analysis method of measurement signals

The investigated building's structure is affected by vibrations, which are generated by street traffic and by the permanently used building's equipment. The vibrations from the street traffic are transferred to the building's structure by subsoil. The vibrations from the building's equipment are passed directly onto the building's structure. The characteristics of the amplitude and frequency of vibrations undergo continuous changes in time depending on street traffic intensity, the number of personal and cargo lifts in operation, ventilation motors in use, wind strength, air temperature, etc. Generally, they are long-term, recurrent and transient random signals. A theoretical analysis of such a complex loading system and its influence on the building's structure is very complicated and laborious. Fortunately, in order to assess the influence of vibrations on the building structure it is not necessary to describe the course of vibrations in detail. It is sufficient to recognize the course, in a representative period of using the building, as a complex superposition of vibrations caused simultaneously by all sources. In such conditions, vibrations were measured and recorded as analogue signals. The analogue signals were converted into digital ones and then analysed. A series of measurements was carried out on a digital 4-channel oscilloscope at the sampling frequency of 1000 samples per sec generated at 0.8 of the maximal observed measured value. Data sets from particular measurements points, recorded separately for the axes of x, y, z were subjected to initial processing by trans-scaling, depending on given accelerometers sensitivity, from a voltage signal [V] into an acceleration one [m/s^2]. Then, each signal was zeroed and averaged.

Typical vibration courses of structural elements of trunk "B" of the examined building occurring relative to the global axis y, established during investigations, in the function of time are presented in Fig. 6, the structure of the glass panel wall is shown in Fig. 7.

An increased level of vibrations was observed during passages of personal lifts. On the 7-th floor, vibrations of the trunk structure intensified with a lift cabin approaching the highest floor and during braking. At the same time, a distinct increase of vibration intensity with a tendency hitting the shaft walls was observed in the panel wall structure – see Fig. 7.

In the reinforced concrete trunk's structure, at the B2 measurement point maximal vibrations amplitudes of $-$ 0.01049 m/s^2

and + 0.01389 m/s^2 were observed. On the other hand, accordingly, at the B3 measurement point, in the glass structure of the panel wall, vibration amplitudes were − 0.0245 m/s^2 and + 0.02666 m/s^2.

4. Vibration damage assessment

All the methods known nowadays concerning the assessment of vibration induced damage can be divided, according to the adopted parameter, depending on velocity, acceleration, and energy. An approximate assessment was carried out with the use of the condition for the acceleration amplitude value of horizontal subsoil movement at the structure's foundation site as:

$$a_p < 0.005g < 0.049 \text{ ms}^{-2} \qquad (1)$$

where:
a_p – horizontal movement acceleration amplitude,
g – earth gravitation acceleration.

For such assessment reliable are vibration acceleration values measured in the measurement points A1 and B1, which were located on the reinforced structure of the tower trunks, i. e. at the basic carrying structure element of the diagnosed buildings, and at the surrounding ground level, according to the PN-85/B-02170 standard. Maximal values of the acceleration amplitude in the considered points are about 50 % of the admissible value as defined by relationship (1). Moreover, the building in question is situated at the distance of over 15 m from the traffic-loaded road axis and, according to the PN-85/B-02170 Standard, the effects of vibrations transmitted by the subsoil can be neglected in the dynamic calculations.

Velocity values as determined in a narrow-band analysis for the measurement points: A2, B2, A3 and B3, were used in the assessment of the maintenance-related vibrations' effect on the façade walls. The current Polish standards do not provide any criterion for the diagnostic procedure for such cases. Based on the analysis found in literature and on the author's own research concerning affecting the design structure of façade walls, especially that of façade plate made of 3 cm – thick architectural glass of the dimensions: 150 cm × 405 cm and 100 cm × 405 cm a criterion of velocity was adopted.

The design structure of façade walls is supported on individual storeys' floor edges. Additionally, the architectural glass plates

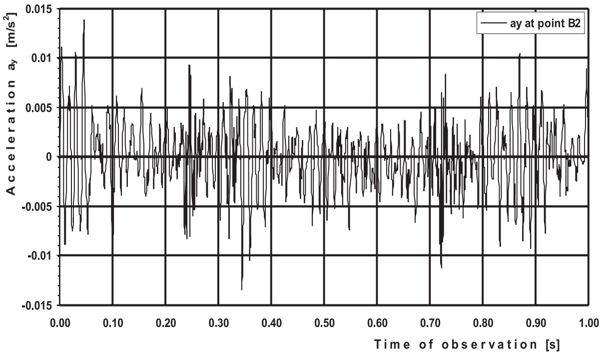

Fig. 6. Vibrations course relative the axis y at the B2 measurement point – reinforced trunk at the 7th floor.

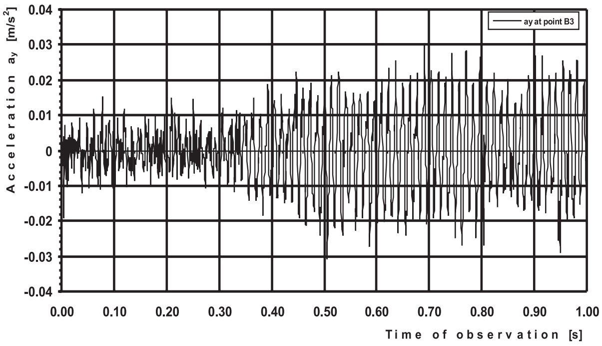

Fig. 8. Vibrations course relative axis y at the B3 measurements point – panel wall.

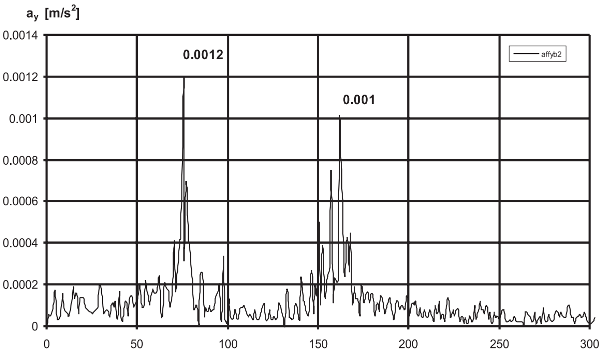

Fig. 7. Amplitudes acceleration spectrum relative the y-axis at the B2 measurement point – 7th floor reinforced concrete trunk.

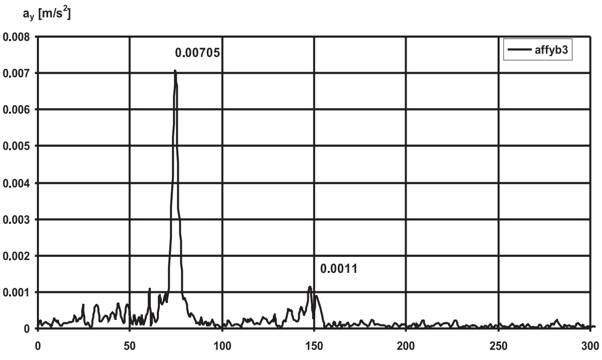

Fig. 9. Amplitude acceleration spectrum relative the y-axis at the B3 measurement point on panel wall.

are fixed in place with aluminium clamps and a clamping mechanism – see Fig. 2. Storey floors, on the other hand, are connected with the given tower's reinforced concrete trunks with the help of grid beams. Such a design solution suggests that the velocity parameters determined in the points: A2, A3, B1 and B3 can be used to determine the level of usage-related vibrations affecting the component elements of the façade walls. According to the adopted criterion and taking into consideration the data from the PN-85/B-02170 standard for devices especially sensitive to dynamic effects, i. e. first class of sensitivity, the admissible effective value of one-directional velocity is 0.1 mms^{-1}.

Maximum effective velocity values were observed at the measurement points fixed on the façade walls structures:

- A3 *x*-axis: 0.02953 mms^{-1} at the frequency of 78.12 Hz,
- A3 *y*-axis: 0.02372 mms^{-1} at the frequency of 23.44 Hz,
- B3 *x*-axis: 0.0322 mms^{-1} at the frequency of 75.19 Hz,
- B3 *y*-axis: 0.01492 mms^{-1} at the frequency of 74.21 Hz,
- B3 *z*-axis: 0.01642 mms^{-1} at the frequency of 75.19 Hz.

Moreover, at the frequencies lower than 10 Hz in the points:

- A3 *x*-axis: 0.01307 mms^{-1} at the frequency of 9.76 Hz,
- A3 *y*-axis: 0.01238 mms^{-1} at the frequency of 9.76 Hz,
- B3 *x*-axis: 0.01038 mms^{-1} at the frequency of 8.78 Hz,
- B3 *z*-axis: 0.04754 mms^{-1} at the frequency of 8.78 Hz.

5. Conclusions

The analysis of spectral characteristics of amplitude accelerations in the points of A2, A3, B2 and B3 – see Fig. 4, has shown the existence of vibrations caused by the passage of personal lifts situated within the towers' trunks through floors and beams onto the structural elements of the façade walls. This phenomenon is especially evident at the frequency ranges of 70 – 79 Hz and 140 – 160 Hz on the distribution diagrams of the acceleration spectrum for above points. Because of the design of the floors (reinforced concrete plate on zinc covered sheet) and mutual connection of the floors with the façade walls at the measurement points situated on these walls, 6 – 8 times increase of vibration level was observed in comparison to the points fixed on the trunks, at the seventh floor level. The velocity peak values within the whole range of the analysed frequencies, i. e. 0 – 500 Hz do not exceed the limit value for machines and equipment of very high vibration sensitivity. In the conditions of the measurements realization, peak values of 2.1 – 9.6 times lower than the admissible were observed. The level of maintenance-related vibrations in the building has no immediate harmful effect on the component elements of the reinforced concrete and steel structures and the façade walls. The computed frequency of resonance vibrations for architectural glass plate is about 24 Hz and the experimentally determined vibration parameters are the most intensive within the frequency ranges of 70 – 80 Hz and 140 – 160 Hz, which excludes the development of façade walls resonance and, as a consequence, their falling-off from the main structure.

One should conclude that the maintenance related wear, and the fact that the clamping system on the façade walls structure more than 20 years old, contributed to the falling off of architectural glass plates. The wear of the mounted elements with a simultaneous action of high intensity winds and considerable temperature changes can lead to further cases of the glass plates falling off of the building's façade.

References

[1] Polish building law: *Construction Law* – Act from 1994 July 7 (in Polish - Dz. U. z 1996 roku nr 89, poz. 414).
[2] CIESIELSKI, R.: *Dynamical diagnosis in building engineering* (in Polish), Construction Review (in Polish) 1/1993, pp. 4 - 13.
[3] CIESIELSKI, R., MACIĄG, E.,STYPUŁA, K.: *Using of vibrations' spectrum to dynamical diagnosis of buildings* (in Polish), Proceedings of the XXXVIII Conference of Civil Engineering Committee, Polish Academy of Sciences, vol. 1, Krynica, 1992.
[4] BEAUCHAMP, K. G.: *Signal processing. Using Analog and Digital Techniques,* George Allan & Unwin Ltd., 1973.
[5] POWERS, D. L.: *Boundary value problems,* Academic Press, 1979.
[6] ASYST, *Module 2 Analysis,* Asyst software Technologies, 1990.
[7] Polish Standard PN-91/N-01352 "Vibrations. Principles of making measurements at work stations (in Polish)".
[8] Polish Standard PN-88/B-02171 "Assessment of vibrations' influence on people at buildings (in Polish)".
[9] Polish Standard PN-85/B-02170 "Assessment of harmfulness of vibrations transmitted through subsoil to buildings (in Polish)".
[10] Polish Standard PN-80/B-03040 "Machines foundations and bearing structures. Calculations and designing (in Polish)".
[11] German Standard DIN-4150-2-3, 1986, "Erschűtterungen im Bauwesen".
[12] Czechoslovakian Standard ČSN-730036, 1996, "Seismické zatížení staveb".
[13] ISO-IS 10137-1992, "Serviceability of buildings against vibration".

https://doi.org/10.26552/com.C.2003.2.54-58

komunikácie
COMMUNICATIONS

Andrzej Surowiecki – Edward Hutnik *

INTERNAL FORCES TESTS IN RETAINING WALLS OF ROAD EMBANKMENTS

The subjects of this paper are resistance structures constituted by reinforced soil applied in highway engineering. Test results carried out on laboratory models are presented, leading to the estimation of the size and shape of the wedge of the reinforced soil embankment block, in the boundary state of active pressure. The task was conducted in the following two stages: on the basis of measured horizontal strains of the embankment (unitary lateral pressures) and reinforcing dowels - with the application of sensors of electro-resistant tensometry. The slip curve, determining the searched block wedge, is formed by the points of maximal normal stress occurring in the reinforcement dowels located in the horizontal layers. The slip curve divides the embankment area into two zones: active (block wedge) and passive, in which dowel anchorage takes place.

1. Introduction

The classical reinforcement soil, being the subject of analysis, has found the broadest application in the field of resistance structures (retaining walls of road embankments, bridge heads, etc.). The necessary length of reinforcement dowels is calculated as a sum of lengths in the active and passive zone when designing the retaining structures made of reinforced soil. The curve of maximal tensile forces divides the soil embankment into two zones mentioned before. Therefore, the mode of accepting the shape of the curve influences the structure designing economy. The article presents a testing method, enabling determination of the value of block wedge reduction in the vertical wall embankment of non-cohesive soil reinforced with horizontal dowels, in reference to an identical structure with no reinforcement. The size and shape of the wedge of soil embankment block with reinforcement was estimated in the boundary state of active pressure. The task was performed as a test (in two stages), on the basis of measured strains of reinforcement dowels, with the application of sensors of electro-resistant tensometry.

2. Measurement rule of block wedge

The subject of the tests are measurements of: horizontal strains of loaded soil embankment (medium-grained dry river sand), carried out in the plane of the retaining wall of model [6] as well as strain measurements of reinforcement dowels by means of electro-resistant tensometry.

In the first stage, the block wedge in the boundary state of the active pressure of the soil embankment was determined on the basis of the estimation of the value of the zone of influence of the external load of the soil surcharge (measured perpendicularly to the plane of the retaining wall of the embankment) on the value of the embankment horizontal pressure, read out at the wall plane. The test method consists of the analysis of processes of changes of the value of soil pressure on the retaining wall, as the distance of the test load of the surcharge (sectional, executed by means of the so-called stemple) from the measurement retaining wall increases. The range of the block wedge in the pressure boundary state was determined as parameter ly,boundary in particular measurement levels, on the basis of the analysis of the course of pressure dwindling phenomenon, as the loading stemple moves further apart from the wall. Then (stage II), parameter ly,boundary was compared with the location of maximal normal stresses in dowels located in horizontal layers. The details of the test method, the stand and the model design are provided in the elaboration works [6, 7, 8, 9] (Fig. 1).

The adopted test method enables to preserve relative specificity of the testing conditions and the planned change of one of the parameters with other parameters unchanged.

3. Profile and location of reinforcement dowels

One of the test goals was to determine forces in reinforcement in the form of strain measurements. The application of limp dowels could guarantee the initiation of strains, possible to be measured with the use of soil surcharge load in the tests (the load was called "special" or "testing").

Dowels in the form of limp steel belts, with the symbol of 50HSA, length of $l_a < 1.80$ m (length of cubicoidal container with model – soil embankment amounts to $L = 2.00$ m) and intersection of $b_a \times g_a = 0.024$ m $\times$ 0.001 m (b – dowel width, g – dowel thickness) were used as reinforcement. The soil centre was reinforced with belts of smooth surface and with notches (in the form

---

* **[1]Andrzej Surowiecki, [2]Edward Hutnik**
[1]Technical University of Wrocław, Institute of Civil Engineering; Agricultural Academy of Wrocław, Institute of Civil Engineering and Landscape Architecture
[2]Agricultural Academy of Wrocław, Institute of Civil Engineering and Landscape Architecture

of angles), fastened with electric welding on both sides. The notches, shaping the belts surface spatially, cause the increase of dowels resistance to pulling out from the soil centre.

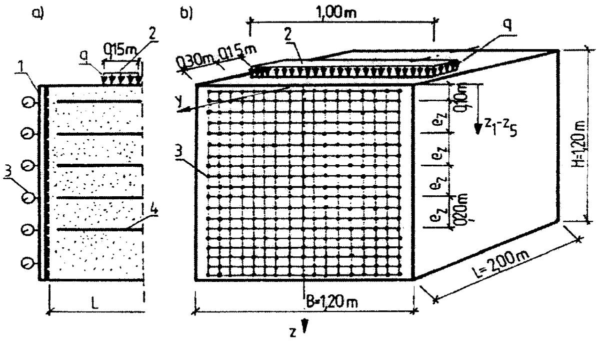

Fig. 1. Design and basic parameters of test stand: a - block of longitudinal vertical intersection; b - general view; 1 - measurement wall (frontal one); 2 - load-carrying plate; 3 - horizontal rooms sensors; 4 - reinforcement belts

In the model designed for laboratory tests, the reinforcement was distributed in horizontal layers with identical vertical spacing $e_z = 0.195$ m. In each layer, the dowels were located paralelly to the longitudinal axis of the container, with the preservation of identical axial horizontal spacing, accepted in turn: $e_x = 0.11$; 0.17 and 0.23 m. The determined three sizes of dowel length l_a in the model form a sequence of terms: 1.0 l_a (A, B, C, D system); 0.72 l_a (E); 0.55 l_a (F). The maximal dowel length $l_a = 1.80$ m (A, B, C, D systems) includes not only the area of the block wedge in the soil embankment (dry coarse-grained river sand was used) but also the anchoring section.

4. Estimation of body of block on basis of horizontal pressure measurements at plane of retaining wall (stage I)

The charts illustrating the change of the determined (approximated) value of the block wedge in the reinforced and non-reinforced soil embankment are presented in figures 2 and 3. The surface areas included between respective curves (Fig. 3) express the reduction of the block body as a result of placing notches on the dowel surface. The test curves were approximated with mathematical functions, for example curves from figure 2 (C_c is a correlation co-efficient):

I for non-reinforced sand:
$v = a\, e^{bu}$, $a = 3.788\ 10^{-2}$, $b = 3.587$, $C_c = 0.918$;
II for non-reinforced sand:
$v = a\, e^{bu}$, $a = 6.159\ 10^{-3}$, $b = 4.464$, $C_c = 0.906$;

I for reinforced sand:
$v = a\, e^{bu}$, $a = 1.053\ 10^{-2}$, $b = 6.119$, $C_c = 0.920$;
II for reinforced sand:
$v = a\, e^{bu}$, $a = 1.085\ 10^{-3}$, $b = 11.221$, $C_c = 0.908$;

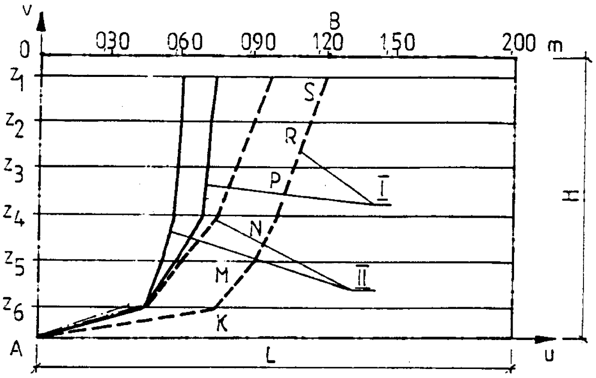

Fig. 2. Range of block wedge estimated in test $l_{y\,gr}$ and course of slip curve: - - - non-reinforced embankment; - - - reinforced with belts with no notches (A system); I - loosely poured; II - pre-consolidated; z1-z6 - measurement levels

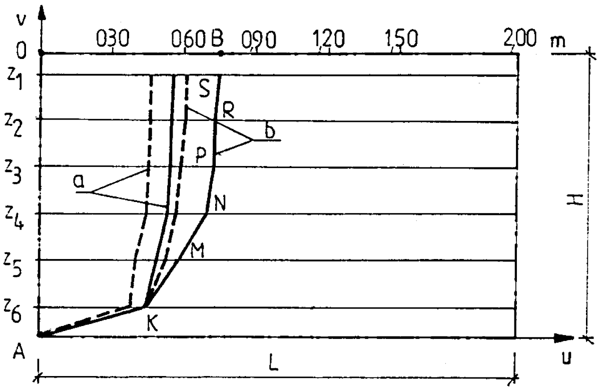

Fig. 3. Value of block wedge and course of slip curve from tests, depending on type of reinforcement (A system): - - - loosely poured embankment; - - - pre-consolidated; a - belts with notches; b - without notches

5. Estimation of block body on basis of distribution of maximal normal stresses in reinforcement (stage II)

Description of reinforcement strain measurements

The special load of the surcharge introduced in the tests results only from the test method and is mainly a factor forcing the formation of the block wedge. The static band load was executed through vertical thrust of a stiff steel stemple, located perpendicularly in relation to the horizontal projection of the container. The details of the course of tests regarding the conditions of the height of the test load are available in the monograph [5]. Also, it is worth noticing that identical load does not cause, to the same extent, the anticipated phenomena of the formation and movement of the block wedge in the soil centre differing with regard to the degree of consolidation and amount of reinforcement. Therefore, the load accepted for test purposes should be treated as approximated, but in admissible limits.

The measurements of unitary reinforcement strains ϵ carried out with the method of electro-resistant tensometry were used in tests with reinforcement systems: A (9 dowels in layer), B (6 dowels in layer) and C (4 belts in layer) – in all cases the dowels included notches on the surface. Yet, the extensometers were stuck only on two belts in each layer so as to reduce the number of connection cables maximally. These ducts, running, out of necessity, near reinforcement through the soil centre are the reason for disturbances during the recording of dowel strains, and artificially (which is undesirable) support the dowels resistance to being taken out from the centre. 10 extensometers were stuck on each belt, 5 pieces on each side. The location of extensometers along the belt length was anticipated in a way enabling to include mainly the active zone (i.e. block wedge range) and partially the anchoring zone. The extensometers were coated with resin, protecting them against mechanical damage and dampness. The measurements and recording of extensometers read-outs were carried out with a multi-point automatic kit designed for strain tests, consisting of an automatic extensometric bridge, an apparatus controlling the measurement and extensometers connecting, extensometric boxes and a microcomputer with a printer. The strains measurement in the reinforcement belts was conducted in turn for two states of surcharge loading: $q = 37.02$ kPa i 61.69 kPa $= q_{max}$. The values of normal stresses in the reinforcement obtained from the micro-computer are expressed with a classic Hook's dependence: $\sigma = E\,\epsilon$.

Normal stresses in reinforcement

Figure 4 shows the stress diagrams along the dowel located at the level of $z_2 = 0.29$ m, depending on the surcharge load with a stemple in the distance of $l_y = 0.30$ m from the measurement wall. These diagrams can represent the strained axis of the reinforcement with the length of l_a.

Figure 5 illustrates the stress distribution along belts located at the levels of $z_2 = 0.29$ m and $z_3 = 0.485$ m, depending on the level of sand backfill density. The stresses in the reinforcement in the sand embankment are lower than in a loosely poured embankment.

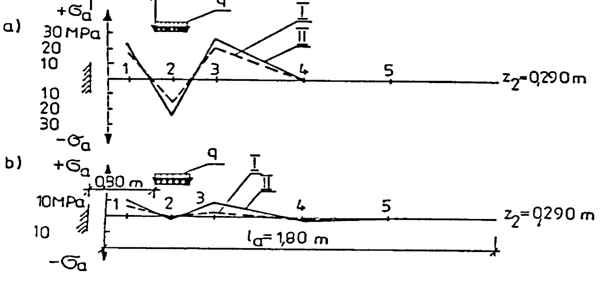

Fig. 4. Diagrams of normal stress distribution in upper surface of reinforcement dowel, depending on load: a - loosely poured sand; b - pre-consolidated; I - load q = 37.02 kPa; II - q = 61.69 kPa; 1-5 - extensometers numeration on upper surface of dowel (A reinforcement system)

Figure 6 presents the stress distribution in the reinforcement dowels on five measurement levels for the embankment consisting of loosely poured sand, reinforced in A system. The surcharge load $q = 61.69$ kPa is located in the distance of $l_y = 0.30$ (curve a) or $l_y = 0.60$ m (curve b) from the retaining wall. The stemple location from the wall amounting to $l_y = 0.60$ m is a minimal distance, at which the soil pressure on the retaining wall (i.e. in this location of the stemple, block wedge in the embankment is fully formed) was not observed.

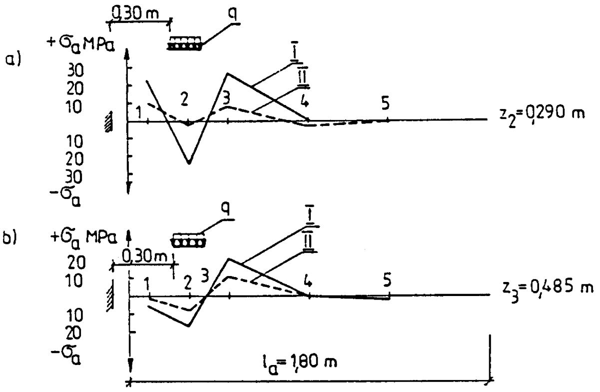

Fig. 5. Diagrams of normal stress distribution in upper surface of reinforcement dowel at level of z_2 (a) i z_3 (b). Load q = 61.69 kPa in distance of l_y = 0.30 m; I - loosely poured sand; II - pre-consolidated sand

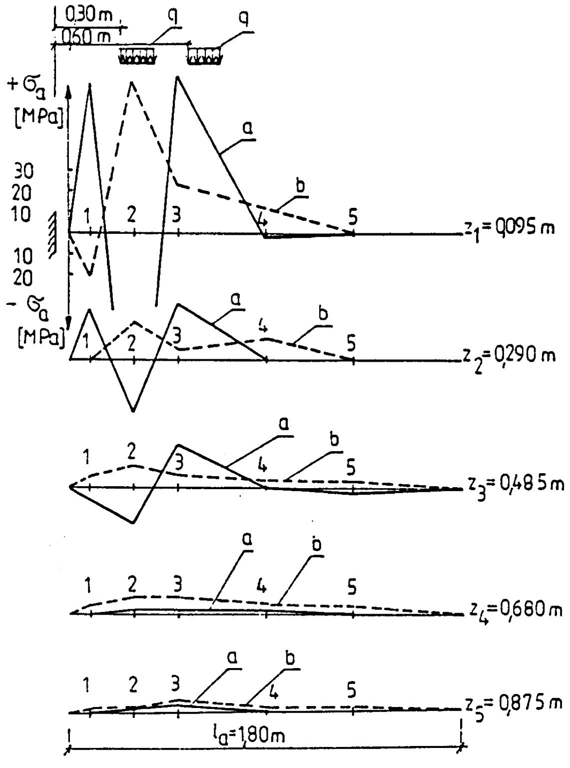

Fig. 6. Diagrams of normal stress distribution on upper surface of reinforcement dowels in loosely poured embankment: a - stemple in distance of l_y = 0.30 m; b - ly = 0.60 m = $l_{y,boundary}$, z_1 - z_5 - reinforcement location levels; 1 - 5 - extensometer numeration; reinforcement system A

Fig. 7 also shows the diagrams of stress distribution in the reinforcement dowels on five measurement levels, depending on the load-carrying stemple relocations, as in fig. 6, but for the pre-consolidated embankment.

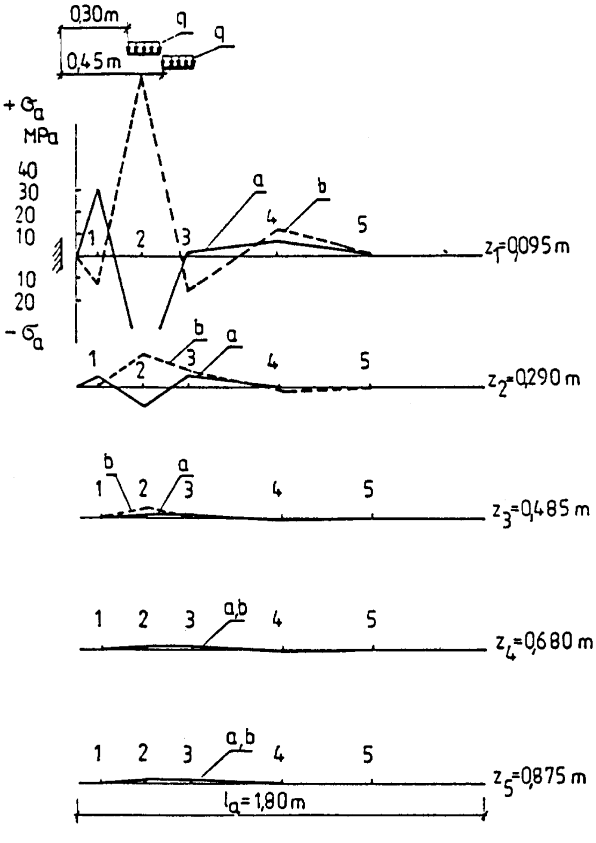

Fig. 7. Diagrams of normal stress distribution in upper surface of reinforcement dowels in pre-consolidated embankment: a - stemple in distance of $l_y = 0.30$ *m; b -* $l_y = 0.45\ m = l_{y,boundary}$, z_1 *-* z_5 *- location levels of reinforcement layers; 1 - 5 - extensometer numeration; reinforcement system A*

Estimation of slip surface location

As results from tests concerning normal stresses in the reinforcement, the profile of the strain of reinforcement belts changes as the distance of the load-carrying stemple from the measurement wall increases. If the distance of the stemple from the wall reaches the boundary value $l_y \cong l_{y,boundary}$ (stemple locations $l_y \geq l_{y,boundary}$ are not accompanied by any increases of soil pressure on the wall), only the tensile stresses will occur on the upper surface of the belts. This phenomenon may confirm the fact of the block wedge formation on the complete embankment height. The belts at the highest level are an exception, where the extensometer No 1 shows compressive stress $(-\sigma_a)$ in their upper surface. This phenomenon repeated in all tests (for a different number of dowels in the model) and is a result of direct, disturbing band influence of the load, which the belts at this level are subject to. The diagrams show that in belts located at lower levels (e.g. z_4 and z_5), the stresses of one character (tensile) occur as early as at shorter distances of the stemple from the retaining wall. Therefore, one may suppose that the embankment damage is of a progressive character, thus the block wedge is formed gradually, gaining first a final shape in the lower zone.

It is known from literature regarding reinforced soil tests [Long, Schlosser 1974, 78] that a potential slip curve in the state of stress boundary equilibrium can be obtained graphically: it is a geometric place of maximal tensile forces in particular reinforcement layers. Proceeding analogically in relation to the points of maximal ordinates occurrence, concerning curve (b) from figures 6 and 7, the course of the slip curve was determined in a test in the reinforced sand embankment (Fig. 8). The accuracy of estimation is connected, among others, with the number of extensometer location points and their distribution on the reinforcement belts.

As results from relevant literature [1], slip along surface can be accepted only for the non-coherence soil. Since the reinforced soil has features of anisotropic coherence [2, 3, 4, 5], the slip curve should be adopted and identified with the line of soil damage with cohesion.

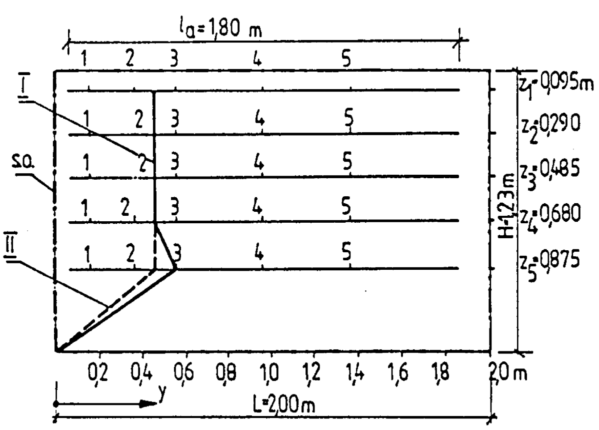

Fig. 8. Curve connecting points of maximal tensile stresses in reinforcement (approximated estimation): 1 - 5 - extensometers numbers stuck to upper surface of dowels; z_1 *-* z_5 *- numbers of measurement levels of retaining wall; I - embankment of loosely poured sand; II - pre-consolidated embankment*

6. Summary

The sizes and shape of the wedge of reinforced soil embankment block were estimated, in the boundary state of active pressure. The task was performed as a test (in two stages), on the basis of measured strains of reinforcement dowels, by means of electro-resistant tensometric sensors. The points of maximal normal stresses occurring in reinforcement dowels located in horizontal layers form a slip curve, separating the searched block wedge from the retaining wall plane. The basis for analysis were the measurements of: horizontal strains of loaded soil embankment, carried out at the plane of a model with considerable dimensions, and the measurements of reinforcement dowel strains by means of electro-resistant tensometry method.

In stage I, the wedge of the block in the boundary state of active pressure of the soil embankment was determined on the basis of the estimation of the value of the zone of influence of the external load of soil surcharge (measured perpendicularly to the plane of the retaining wall of the embankment) on the value of the horizontal pressure of the embankment, read out at the wall plane. The testing method consists of the analysis of the process of changes of the value of soil pressure on the retaining wall, as the distance of the test loading of surcharge (sectional, realised by means of the so-called stemple) from the measurement retaining wall increases. On the basis of the analysis of the course of the phenomenon of pressure dwindling, as the load-carrying stemple moves further apart from the wall, the range of the block of the wedge was determined, in the boundary state of active pressure as parameter $l_{y,boundary}$ in particular measurement levels. Then (stage II), parameter $l_{y,boundary}$ was compared with the location of maximal normal stresses in dowels, at the level of the embankment.

Summing up, the usability of tensometric tests for examining the operation of loaded engineering structures was proved. The measurement of normal stresses in the reinforcement enabled quite a precise specification of the shape of the slip surface in the reinforced soil embankment.

References

[1] GLAZER, Z.: *Mechanika gruntów [Soil mechanics]*, Wyd. Geologiczne [Geological Publishing House], Warszawa 1987.

[2] LONG, N. T.: *Badania gruntów zbrojonych* – Wybrane zagadnienia geotechniki [Reinforced soil tests – Selected problems of geotechnics], PAN-IBW, Wrocław, Ossolineum, 1978, p. 185 – 210.

[3] LONG, N. T., SCHLOSSER, F.: *Wymiarowanie murów z gruntów zbrojonych – Wybrane zagadnienia geotechniki [Dimensioning of reinforced soil masonry – Selected problems of geotechnics]* – , PAN-IBW, Wrocław, Ossolineum, 1978, p. 211 – 237.

[4] LONG, N. T., SCHLOSSER, F.: *Zasada działania i zachowanie się gruntu zbrojonego – Wybrane zagadnienia geotechniki [Principle of operation and profile of reinforced soil – Selected problems of geotechnics]*, PAN-IBW, Wrocław, Ossolineum, 1978, p. 157 – 184.

[5] SCHLOSSER, F.: *Grunt zbrojony w budownictwie lądowym [Reinforced soil in civil engineering]*, Archiwum Hydrotechniki [Hydraulic engineering archive], vol. XXI, 1974, sheet 2, p. 299 – 336.

[6] SUROWIECKI, A.: *Analiza doświadczalna poziomego parcia gruntu zbrojonego oporowych konstrukcji podtorza [Test analysis of horizontal pressure of reinforced soil of retaining structures of track substructure]*, Pr. Nauk. Instytutu Inż. Lądowej [Work of Scientific Institute of Civil Engineering] P. Wr., No 41, Seria: Monografie [Series: Monographs] No 15, Wrocław 1993.

[7] SUROWIECKI, A.: *Laboruntersuchungen von mechanischen Eigenschaften bewehrter lockerer Bodenschichten*, Bautechnik, Jg. 71, H. 11, 1994, p. 707 – 711.

[8] SUROWIECKI, A.: *Badania doświadczalne klina blocku ściany oporowej z gruntu zbrojonego [Tests of the wedge of a block of a retaining wall of reinforced soil]*. Inżynieria Morska i Geotechnika [Naval Engineering and Geotechnics], No 2, Gdańsk, 1995, p. 68 – 72.

[9] SUROWIECKI, A.: *Interaction between reinforced soil components*, Studia Geotechnica et Mechanica, Vol. XX, No. 1/2, Wrocław 1998, p. 43 – 61.

Názov doktorandskej dizertačnej práce: **Controlling logistického procesu**
Autor: **Ing. Juraj Dubovec**
Vedný odbor: **62-03-9 Odvetvové a prierezové ekonomiky**
Školiace pracovisko: **Fakulta prevádzky a ekonomiky dopravy a spojov Žilinskej univerzity**
Školiteľ: **Doc. Ing. Jozaf Strišš, CSc.**

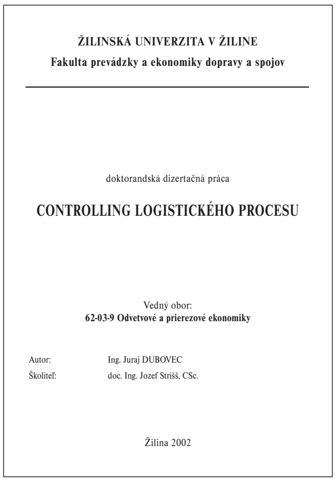

ŽILINSKÁ UNIVERZITA V ŽILINE
Fakulta prevádzky a ekonomiky dopravy a spojov

doktorandská dizertačná práca

CONTROLLING LOGISTICKÉHO PROCESU

Vedný obor:
62-03-9 Odvetvové a prierezové ekonomiky

Autor: Ing. Juraj DUBOVEC
Školiteľ: doc. Ing. Jozef Strišš, CSc.

Žilina 2002

Resumé:

Doktorandská dizertačná práca sa zaoberá controllingom logistického procesu, ktorý je nástrojom pre podporu manažérskeho rozhodovania v dynamickom podnikateľskom prostredí. Výstavbou komplexnej sústavy kalkulácie nákladov a výkonov, systému vhodných logistických ukazovateľov a ich premietnutím do informačného systému je možné docieliť dobré fungovanie a súlad logistických procesov s prijatou stratégiou.

Vplyv dynamiky informačných technológií umožnil postupnú konvergenciu hodnotovej a informačnej stránky podnikového systému a vytvoril tak priestor pre nové postupy a metódy v oblasti controllingu.

Globalizácia, silný medzinárodný konkurenčný tlak, pracovná mobilita, spájanie podnikov a nové informačné technológie charakterizujú prostredie, v ktorom sa musia osvedčiť controllingové postupy.

V teoretickej rovine dizertačná práca popisuje možnosti využitia konvergencie rôznych techník a technológií pre stanovenie controllingových ukazovateľov logistického procesu pre podporu rozhodovania na rôznych riadiacich úrovniach.

Uvedené postupy sú súčasťou projektu tvorby „Balanced Scorecard“, ktoré umožňujú sledovanie výkonnosti pomocou predložených postupov. Hierarchia ukazovateľov je jednoduchá a prehľadná, vrátane vzťahov používaných na výpočet jednotlivých ukazovateľov a umožňuje vytvárať rôzne scenáre podľa modelu „čo sa stane keď“. Postup stratégie sa sleduje pomocou finančných a nefinančných ukazovateľov.

Praktické riešenia ukazujú, že pre podporu rozhodovania postačuje maximálne 20 ukazovateľov so vzájomnými väzbami.

Ukazovatele sú dvoch druhov:

- *Ukazovatele úsilia (zvyčajne sú špecifické pre danú firmu)*
- *Ukazovatele výsledkov*

Voľba ukazovateľov (najmä ukazovatele úsilia) a väzieb medzi ukazovateľmi vyjadruje spoločnú víziu úspešnosti firemnej stratégie, nakoľko dáva jasnú predstavu o procese.

Pre efektívny controlling logistického procesu potrebuje podnik systém logistických ukazovateľov, ktoré by spoľahlivo identifikovali „úzke“ miesta procesu. Tieto signály nám umožňujú zasahovať do logistických procesov tak, aby sa dosiahla rýchlosť, pružnosť a hospodárnosť celého logistického systému.

POKYNY PRE AUTOROV PRÍSPEVKOV DO ČASOPISU KOMUNIKÁCIE – vedecké listy Žilinskej univerzity

1. Redakcia prijíma iba príspevky doteraz nepublikované alebo inde nezaslané na uverejnenie.
2. Rukopis musí byť v jazyku anglickom. Príspevok by nemal prekročiť 7 strán (formát A4, písmo Times Roman 12 bodové). K článku dodá autor **resumé** v rozsahu maximálne 10 riadkov (v anglickom jazyku).
3. Príspevok prosíme poslať: **e-mailom**, ako prílohu spracovanú vo Word-e, na adresu: *holesa@nic.utc.sk* alebo *polednak@fsi.utc.sk* príp. *vrablova@nic.utc.sk* (alebo doručiť na diskete 3,5″) **a jeden výtlačok** článku na adresu Žilinská univerzita, OVaV, Moyzesova 20, 010 26 Žilina.
4. Skratky, ktoré nie sú bežné, je nutné pri ich prvom použití rozpísať v plnom znení.
5. Obrázky, grafy a schémy, pokiaľ nie sú spracované v Microsoft WORD, je potrebné doručiť buď v digitálnej forme (ako GIF, JPG, TIFF, BMP súbory), prípadne nakresliť kontrastne na bielom papieri a predložiť v jednom exemplári. Pri požiadavke na uverejnenie fotografie priložiť ako podklad kontrastnú fotografiu alebo diapozitív.
6. Odvolania na literatúru sa označujú v texte alebo v poznámkach pod čiarou príslušným poradovým číslom v hranatej zátvorke. **Zoznam použitej literatúry** je uvedený za príspevkom. Citovanie literatúry musí byť **podľa záväznej STN 01 0197 (ISO 690)** „Bibliografické odkazy".
7. K rukopisu treba pripojiť **plné meno a priezvisko autora a adresu inštitúcie v ktorej pracuje, e-mail adresu** a číslo telefónu alebo faxu.
8. Príspevok posúdi redakčná rada na svojom najbližšom zasadnutí a v prípade jeho zaradenia do niektorého z budúcich čísiel podrobí rukopis recenziám a jazykovej korektúre. Pred tlačou bude poslaný autorovi na definitívnu kontrolu.
9. Termíny na dodanie príspevkov do čísiel v roku sú: 30. september, 31. december, 31. marec a 30. jún.

COMMUNICATIONS – Scientific Letters of the University of Žilina Writer's Guidelines

1. Submissions for publication must be unpublished and not be a multiple submission.
2. Manuscripts written in English language must include abstract also written in English. The submission should not exceed 7 pages (format A4, Times Roman size 12). The abstract should not exceed 10 lines.
3. Submissions should be sent: **by e-mail** (as attachment in system Microsoft WORD) to one of the following addresses: *holesa@nic.utc.sk* or *vrablova@nic.utc.sk* or *polednak@fsi.utc.sk* **with a hard copy** (to be assessed by the editorial board) **or on a 3.5″ diskette** with a hard copy to the following address: Zilinska univerzita, OVaV, Moyzesova 20, SK-10 26 Zilina, Slovakia.
4. Abbreviations, which are not common, must be used in full when mentioned for the first time.
5. Figures, graphs and diagrams, if not processed by Microsoft WORD, must be sent in electronic form (as GIF, JPG, TIFF, BMP files) or drawn in contrast on white paper, one copy enclosed. Photographs for publication must be either contrastive or on a slide.
6. References are to be marked either in the text or as footnotes numbered respectively. Numbers must be in square brackets. The list of references should follow the paper (according to **ISO 690**).
7. The author's exact mailing address, **full names, e-mail address, telephone or fax number, and the address of the organisation where the author works** and contact information must be enclosed.
8. The editorial board will assess the submission in its following session. In the case that the article is accepted for future volumes, the board submits the manuscript to the editors for review and language correction. After reviewing and incorporating the editor's remarks, the final draft (before printing) will be sent to authors for final review and adjustment.
9. The deadlines for submissions are as follows: September 30, December 31, March 31 and Juny 30.

KOMUNIKÁCIE
COMMUNICATIONS

VEDECKÉ LISTY ŽILINSKEJ UNIVERZITY
SCIENTIFIC LETTERS OF THE UNIVERSITY OF ŽILINA

Adresa redakcie:
Address of the editorial office:
Žilinská univerzita
Oddelenie pre vedu a výskum
Office for Science and Research
Moyzesova 20, Slovakia
SK 010 26 Žilina
Tel.: +421/41/5620 392
Fax: +421/41/7247 702
E-mail: polednak@fsi.utc.sk, holesa@nic.utc.sk

Každý článok bol oponovaný dvoma oponentmi.
Each paper was reviewed by two reviewers.

Časopis je excerpovaný v Compendexe
Journal is excerpted in Compendex

Vydáva Žilinská univerzita
v EDIS - vydavateľstve ŽU
J. M. Hurbana 15, 010 26 Žilina
pod registračným číslom 1989/98
ISSN 1335-4205

It is published by the University of Žilina in
EDIS - Publishing Institution of Žilina University
Registered No: 1989/98
ISSN 1335-4205

Objednávky na predplatné prijíma redakcia
Vychádza štvrťročne
Ročné predplatné na rok 2002 je 500,- Sk

Order forms should be returned to the editorial office
Published quarterly
The subscription rate for year 2002 is 500 SKK.

Jednotlivé čísla časopisu sú uverejnené tiež na:
Single issues of the journal can be found on:
http://www.utc.sk/komunikacie